WASHINGTON UNIVERSITY

Department of Physics

Dissertation Examination Committee:
James Buckley, Chair
Henric Krawczynski
Martin Israel
Ramanath Cowsik
Lee Sobotka
Demetrios Sarantites

VERY HIGH ENERGY GAMMA RAYS FROM THE GALACTIC CENTER

by

Karl Peter Kosack

A dissertation presented to the
Graduate School of Arts and Sciences
of Washington University in
partial fulfillment of the
requirements for the degree
of Doctor of Philosophy

May 2005

Saint Louis, Missouri

Acknowledgements

I would first like to thank my adviser Jim Buckley for all the support and encouragement throughout my graduate school experience. The work presented in this dissertation could not have been done without his constant stream of ideas and feedback. Likewise, I would like to acknowledge all of my committee members for their useful comments and suggestions.

I also acknowledge the graduate students, professors and staff of the Laboratory for Experimental Astrophysics at Washington University with whom I collaborated over the years: Paul Dowkontt, Richard Bose, Garry Simburger, Henric Krawczynski, Marty Israel, and Marty Olevitch, from whom I have gained a deeper understanding of electronics, hardware development, and astrophysics in general. I owe much of my positive graduate experience to my friends and fellow graduate students: Lauren Scott, Paul Rebillot, Jeremy Perkins, Scott Hughes, Christopher Aubin, Randy Wolfmeyer, Mead Jordan, Trey Garson, Kuen "Vicky" Lee, Brian Rauch and Kristopher Gutierrez (many of whom provided hours of on-line computer tank fights, and probably some important science discussion too). I can't imagine a better group of people to work with.

I would also like to thank Trevor Weekes and the VERITAS[1] collaboration (in particular all Whipple telescope observers) who were influential in providing data and feedback, and for accepting my observing proposals. Thanks also to the McDonnell Center for Space Sciences for funding much of my research and travel and for granting me a fellowship for my first three years.

Additional thanks go out to all of my non-physicist friends: the entire roving pack of Funhounds[2], Ellen Wurm, etc. for feigning genuine interest in astrophysics during my graduate career, and of course to my family for putting up with me going to school for twenty-two years. Finally, I must acknowledge the *Grind* coffee shop in St. Louis's Central West End, where I typed about ninety percent of this thesis and spent countless hours in front of my laptop drinking iced mochas and writing analysis code. I know I will always harbor fond memories of my Graduate School years at Washington University and hope to keep in contact both professionally and socially with all of the co-workers and friends I have made here.

[1]The VERITAS Collaboration is supported by the U.S. Dept. of Energy, N.S.F., the Smithsonian Institution, P.P.A.R.C. (U.K.), N.S.E.R.C. (Canada), and Science Foundation Ireland.

[2]Supported predominantly by the Jägermeister company and the Guinness brewery

Contents

List of Figures

List of Tables

Abstract

I report an analysis of TeV gamma-ray emission from the Galactic Center region using the Whipple 10m gamma-ray telescope. New analysis techniques for analyzing Whipple data are discussed, including gamma-ray selection criteria which scale automatically with zenith-angle, energy, and seasonal changes to the instrument. Additionally, two-dimensional imaging techniques are presented for analyzing sources which are offset from the center of the camera. The results of 31 hours of on-source observations of the Galactic Center over an extended period from 1995 through 2004 are presented. Empirically, our results show a very high energy measurement with a flat spectrum extending above 3 TeV, and no evidence for variability over the entire observation period. The measured excess corresponds to an integral flux of $(5.3 \pm 1.9) \cdot 10^{-9}\,\mathrm{m}^{-2}\mathrm{s}^{-1}\mathrm{TeV}^{-1}$ above an energy of 2.8 TeV, roughly 22% of the flux from the Crab Nebula at this energy. The 95% confidence region has an angular extent of about 15 arcmin and includes the position of Sgr A*. While the details of the emission mechanism are still unknown, we discuss several possible astrophysical and cosmological interpretations, including accretion-powered emission from an AGN-like source, and emission from WIMP dark-matter annihilation.

Chapter 1

Intro

The heart of the Milky Way is a fascinating region from an astrophysical standpoint—not only does it contain one of the brightest sources of radio, X-ray, and GeV gamma-ray emission in the sky, but the details of the emission from this region are largely unknown and may include such exotic processes as super-massive black-hole accretion and exotic dark matter particle annihilation. Presented in this dissertation is one of the first detections of very-high-energy (VHE) gamma-ray emission from the Galactic Center (Kosack et al., 2004). This result is consistent with a subsequent higher-sensitivity detection by the HESS experiment (Aharonian et al., 2004).

1.1 The Center of our Galaxy

The Galactic Center (GC), which is located approximately 8.5 kpc (R_{GC}) from Earth in the constellation of Sagittarius, is a complicated region containing a wide variety of sources within a small region of the sky. Within a two-degree field-of-view

(which is typical for a ground-based gamma-ray telescope), a search on the Simbad astronomical database, for example, returns over 10,000 known objects.[1] Though optical observations of this region are limited due to absorption by dust, a number of bright sources, including stars, supernova remnants, and background galaxies, can be seen in other wavebands. In the field of TeV Gamma-Ray Astronomy, where there are only a handful of known sources in the sky, source confusion is rarely a consideration and the emission is usually attributed to the nearest source of high-energy particles. For this reason, it is tempting to associate high-energy emission with the massive black-hole candidate Sagittarius A*. However, due to the large number of high-energy sources (e.g. compact stellar remnants, supernovae shells, or hot gas clouds) near the Galactic Center, several of which are known emitters of X-Ray and GeV radiation, source confusion is still a major concern. Here I present a brief overview of the potential high-energy sources in the GC region. Since I eventually argue that the TeV observations by our group and by HESS are most probably pointing to emission very close to the central arcminute (~ 3 pc) region in the immediate vicinity of Sgr A*, I focus this discussion on the multi-wavelength data from this region.

1.1.1 Sagittarius A*

The brightest object in the central few parsecs of the Galactic Center region is an unidentified compact source known as Sagittarius A* (Sgr A*), which is located at

[1] http://simbad.u-strasbg.fr/Simbad

the center-of-mass of the galaxy [2] . This object, which has a bolometric luminosity of $L_B \simeq 10^{37}\,\mathrm{erg\,s^{-1}}$(Narayan et al., 1998), is brightly visible in the Radio through X-Ray wavebands (excluding optical), and is widely believed to be a super-massive black hole surrounded by an accretion disc.

Super-massive Black Hole

The most compelling evidence that Sgr A* is a black hole comes from infrared measurements of the orbits of seven stars about the central of the galaxy. These measurements constrain the mass of the central object to $M_\star = (3.7\pm0.2)\times10^6(R_{GC}/8\mathrm{kpc})^3 M_\odot$, within a radius less than 10 AU.(Ghez et al., 2005). The closest approach of a measured stellar orbit (S0-16) was 45 AU, at a velocity of 12,000 km/s. Radio measurements of the peculiar motion[3] of the object itself with respect to extra-galactic sources put a conservative lower-limit on the mass of Sgr A* of $0.4\times10^6\,M_\odot$ within an emission radius of 0.5 AU, implying a matter density on the order of $\sim 10^{22}\,M_\odot\,\mathrm{pc}^{-3}$, a strong indication that the matter is in the form of a black-hole (Reid and Brunthaler, 2004). The "size" of the black hole, defined by its Schwarzschild radius, $R_s \equiv 2GM/c^2$, is approximately 10^{10} m or $\sim 1/20$ AU.

[2] Galactic coordinates: $(l = 0^\circ, b = 0^\circ)$; Equatorial coordinates: (Right Ascension) $\alpha = 17^h45^m40.0383^s \pm 0.0006^s$, (Declination) $\delta = -29^\circ00'28.069'' \pm 0.014''$, J2000 epoch (Falcke, 2003, p 317)

[3] The *peculiar* motion of an object its true motion relative to a local standard for rest, removing all effects of the Earth's orbit around the Sun and the Solar System's orbit about the galaxy.

Radio Emission

The existence of a compact radio source in the Galactic center was first theorized by Lynden-Bell and Rees (1971), citing evidence that the center of our galaxy has similar properties as other active galaxies, which are known to contain super-massive black holes. The first positive detection of a bright source of radio emission from the Galactic Center was made by Balick and Brown (1974), who reported an unresolved object, which was later named Sagittarius A* to differentiate it from Sagittarius A, which encompasses a larger region(Falcke, 2003). Subsequent observations with higher-resolution radio telescopes resolve Sgr A* as an extremely bright point-source, with luminosity $L_{radio} \sim 10^{36}\,\mathrm{erg\,s^{-1}}$ and an average power-law $S_\nu \propto \nu^{1/3}$ spectrum in the GHz range, with an upturn in the sub-mm regime and a cutoff around $10^{12}\,\mathrm{Hz}$ (e.g. Krichbaum et al., 1998; Melia and Falcke, 2001). This spectral index is a bit of a mystery, since it is not what one expects for self-absorption ($\nu^{5/3}$) or for emission from a power-law distribution of electrons—rather, it is consistent with mono-energetic emission. The radio emission is also variable on time-scales from 100 days (Zhao et al., 2001) to as little as 1 hour, with a 20% change in signal amplitude ($\Delta S/S$). This fixes the size of the radio emission region $R < (\Delta S/S) \cdot c\Delta t \sim 20R_s$, at 100 GHz.

IR Emission and Flaring

Quiescent near-infrared emission from within a few milliarcseconds (mas) of Sgr A* ($\sim 10^2\ R_s$) has been observed from an unresolved source coincident with Sgr

A* (within 10-20 mas), which may be attributed to synchrotron emission from high-energy electrons, or thermal emission from hot gas in the accretion disc (Genzel et al., 2003). Time-variable flaring activity is also present, with a total flare time-scale of 30-50 minutes, a ~ 5 min rise/fall time, and quasi-periodic structure on ~ 17 minute time-scales(Genzel et al., 2003). The flaring time-scale implies that the IR emission is occurring in a region smaller than about 30 Schwartzchild radii of the black hole: ($R_{IR} \leq c\Delta t \simeq 30 R_s$).

X-Ray Emission and Flaring

High-resolution Chandra Observatory data show a bright X-ray point-like source (CXOGC J174540.0-290027) associated with Sgr A* (within about 0.2 arc-seconds), and possible extended emission out to a distance of 1.4 arcsec from Sgr A*. The quiescent emission luminosity in the $2-10\,\mathrm{keV}$ energy range is $L_X = 2.4 \times 10^{33}\,\mathrm{erg\,s^{-1}}$, with an integral power-law spectral index of $\gamma = 2.7^{+1.3}_{-0.9}$ (Baganoff et al., 2003). In addition to this steady emission component, Chandra (Markoff et al., 2001) and XMM (Porquet et al., 2003) have also detected dramatic X-ray flaring activity from Sgr A*. The flares, which occur approximately daily, have a flux up to two orders of magnitude above the quiescent emission and last $\lesssim 200\,\mathrm{s}$, with doubling times on the order of $\Delta t \sim 10$ min (Markoff et al., 2001). The flare-state spectrum is much harder than the quiescent state, with $\gamma \sim 0.3$ (Liu and Melia, 2002). The variability implies an emitting region $R \leq 20\,R_s$, similar to the infrared measurements. Recent multi-wavelength monitoring of Sgr A* has shown a correlated X-ray and NIR flare

(Eckart et al., 2004), implying the two have a related emission mechanism.

GeV Gamma-Ray Emission?

In 1998, the EGRET instrument on board the Compton Gamma-Ray Observatory satellite detected an extremely bright peak in the excess of GeV gamma-ray emission toward the Galactic Center (a source labeled 3EG J1746-2851)(Mayer-Hasselwander et al., 1998). The emission has a peak energy of 500 MeV, and in this initial detection was found to be marginally consistent with a point-source located within 0.2° of Sagittarius A*. The measured flux above 100 MeV is $(217 \pm 15) \times 10^{-8}\,\mathrm{ph\,cm^{-2}\,s^{-1}}$, with a broken power-law spectrum of:

$$F(E) = \begin{cases} (2.2 \pm 0.01) \times 10^{-10} (E/1900\,\mathrm{MeV})^{-1.30 \pm 0.03} & (E < 1900\,\mathrm{MeV}) \\ (2.2 \pm 0.01) \times 10^{-10} (E/1900\,\mathrm{MeV})^{-3.1 \pm 0.2} & (E > 1900\,\mathrm{MeV}) \end{cases} \tag{1.1}$$

Recent re-analyses of the EGRET data, more heavily weighting the higher-energy emission (with higher angular resolution) by Hooper and Dingus (2002) and Pohl (2004) indicate the excess is offset from the position of Sgr A*, and is in fact a separate, but possibly nearby, object. These analyses exclude the position of Sgr A* at a $> 95\%$ confidence level.

1.1.2 Other Objects Near the Galactic Center

Sgr A East

Surrounding Sgr A* lies an extended radio object known as *Sgr A East* (schematically shown in Figure 1.1), which is characterized by a shell-like structure with an

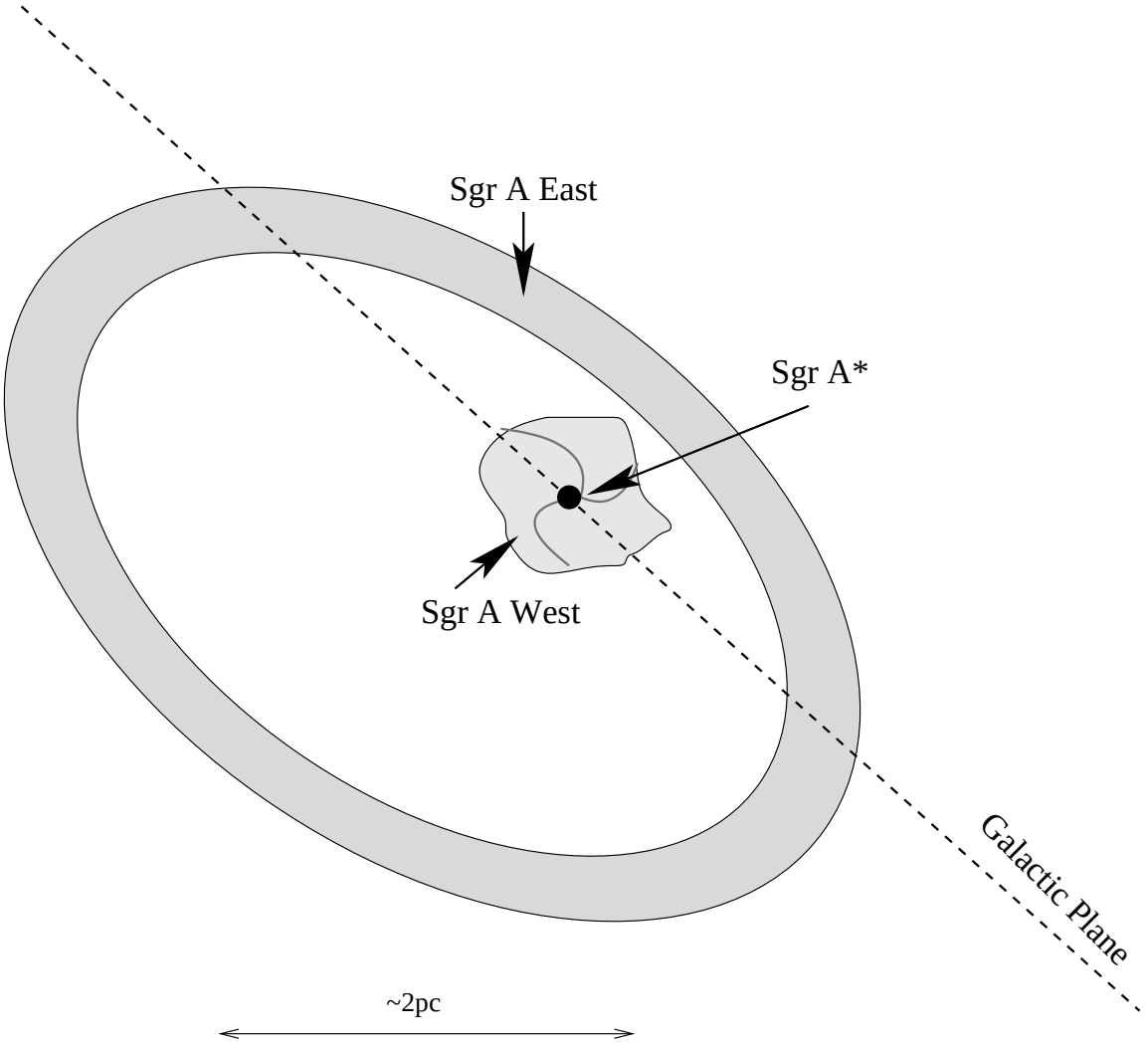

FIGURE 1.1: Schematic Diagram of Sgr A*, Sgr A East, and Sgr A West. The total angular size of the depicted region is about 1/30 of a degree, or 1/60 of the field-of-view of the Whipple telescope.

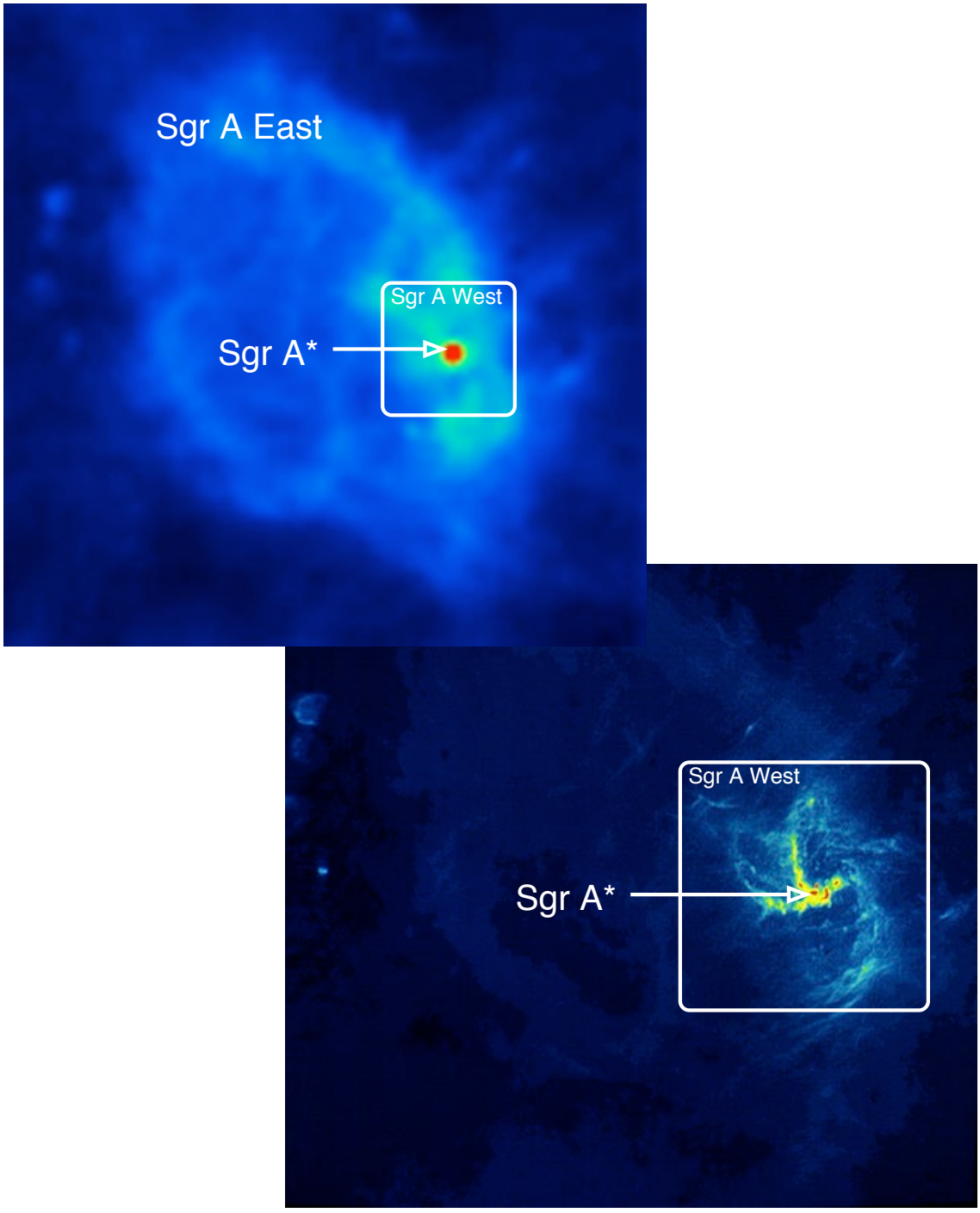

FIGURE 1.2: Radio images of the Galactic Center (Plante et al.). The top image (a 20 cm wavelength VLA image) shows the ring-shape of Sgr A East, while the spiral shaped Sgr A West dust cloud is visible in the bottom (a 6 cm wavelength VLA image). The bright point-like object at the center of Sgr A West is Sgr A*, which is visible in both images.

angular size of about 3.5 by 2.5 arc-minutes (Ekers et al., 1975). Sgr A East is likely either a supernova remnant (Ekers et al., 1983), the remains of several nearby supernovae, or a star which was tidally disrupted by the Sgr A* black hole (Khokhlov and Melia, 1996). The emission from Sgr A East is non-thermal, indicating the presence of high-energy particles—most likely radio-synchrotron emission from relativistic electrons (Maeda et al., 2002). If the observed EGRET GeV emission is associated with Sgr A East, it would be two orders of magnitude brighter than other known supernova remnants (Fatuzzo and Melia, 2003).

Sgr A West

Within the Sgr A East shell, and just surrounding Sgr A*, is *Sgr A West*, a spiral-shaped region of thermally-emitting hot gas. The spiral nature is a possible indication that the gas is falling inward toward Sgr A*. Sgr A West may also be physically located near Sgr A East, which would allow interaction between the two objects. Recent low-frequency radio observations (Roy and Pramesh Rao, 2004) suggest Sgr A* lies physically in front of Sgr A West.

1.2 VHE Gamma-Ray Emission Mechanisms

One might expect to see TeV emission from the Galactic Center from two classes of emission: astrophysical and cosmological. Astrophysical emission includes processes that are present in other known TeV sources such as active galactic nuclei or supernova

remnants, while cosmological emission may be generated by more exotic mechanisms such as the annihilation of massive dark matter particles. Both of these possibilities are significant motivation for looking at the Galactic Center with a telescope sensitive to VHE gamma rays.

1.2.1 AGN-Like Emission

Active Galaxies, which include Seyfert galaxies, Quasars, and BL Lac objects, contain an extremely bright, compact source of radiation at their center. This *Active Galactic Nucleus*, or AGN, out-shines the other luminous matter in the galaxy, making them appear as a single, distant, point-like object. Originally discovered in the radio regime, AGNs emit a broad spectrum of radiation from radio to TeV gamma-rays and are thought to be powered by super-massive black holes ($M \approx 10^8 M_\odot$), around which matter is accreting at an appreciable rate (Frank et al., 1992). AGN are observed to expel relativistic jets of matter in which much of the very high energy emission likely originates and are typically highly variable. They switch between periods of strong flaring activity with time-scales on the order of minutes to days, to relatively quiescent states.

Though the details of AGN are not well known, accretion (the gravitational in-fall of matter onto a massive compact object) appears to be the dominant power source: a fraction of the gravitational potential energy associated with accreting matter can be converted to radiation; this fraction can be as much as $0.3Mc^2$ for accretion on to a black-hole, a very high efficiency compared with $0.007mc^2$ for the nuclear fusion of

hydrogen. From a purely Newtonian standpoint, the gravitational potential energy of a mass m which travels from infinity to a radius R from a larger object with mass M is GMm/R. The maximum accretion rate, $\dot{M}_{edd}$, is related to the Eddington luminosity (L_{edd}, which is found by balancing radiation pressure and gravitational potential energy) by:

$$L_{edd} = \dot{M}_{edd} c^2 \cdot \eta \tag{1.2}$$

where η is the fraction of the rest mass energy released as radiation. When the accreting matter has angular momentum, it forms an *accretion disk*, where in-falling streams of matter intersect themselves forming shocks that thermodynamically mix the matter, eventually resulting in a circular disc-like structure. In order for a super-massive black hole (or any other massive object) to emit the luminosities observed in a typical AGN, there must be a large supply of accreting gas.

TeV gamma-rays may be generated via several mechanisms in AGNs: inverse-Compton up-scattering of low-energy photons by high-energy electrons accelerated outside the emission region, inverse-Compton scattering of synchrotron photons by the same synchrotron-emitting electrons (synchrotron-self-Compton), hadronic cascades from high-energy protons (e.g., $p + p \rightarrow \pi^0 \rightarrow 2\gamma$), photo-meson interactions (e.g. $p + photon \rightarrow \pi^0 + p \rightarrow 2\gamma$), or if magnetic fields are large enough, direct proton-synchrotron emission (Aharonian and Neronov, 2005). Little is known about the mechanism for accelerating particles up to TeV energies, but typically (lacking better information), first-order Fermi acceleration in a shock is assumed.

Recent evidence indicates that our galaxy may have a lot in common with active

galaxies. Quiescent and flaring X-ray and NIR emission from Sgr A* are consistent with a Keplarian accretion flow, indicating that the central black hole may power a low-accretion-rate AGN (Mezger et al., 1996). However, the Eddington luminosity of Sgr A* is $L_{Edd} \sim 5 \times 10^{44}\,\mathrm{erg\,s^{-1}}$, which is about nine orders of magnitude brighter than the observed luminosity, implying that the accretion process must be *radiatively-inefficient* in contrast to AGNs.

The radiative efficiency for an accretion flow is defined as:

$$\eta_r \equiv \frac{L}{\dot{m}c^2} \tag{1.3}$$

where L is the observed luminosity and $\dot{m}$ is the accretion rate. A popular accretion model which can explain both quiescent and flaring activity with very low η_r is the *advection-dominated accretion-flow* (ADAF) (e.g. Ichimaru, 1977; Esin et al., 1997; Narayan et al., 1995; Manmoto et al., 1997), which has been widely applied to Sgr A*. In this model, the flow of matter in the disc is in the form of an optically thin gas of ions, which cools inefficiently—i.e., the rate of viscous heating is much greater than the cooling rate. Most of the accretion energy is stored thermally and is advected into the black hole, leading to overall luminosities orders of magnitude lower than the Eddington limit. Since ADAF models include the effects of angular momentum, they more accurately describes galactic processes than simple spherically-symmetric (or Bondi) accretion.

As in an AGN, a number of mechanisms may be responsible for generating TeV gamma-rays in the Galactic Center, including π^0-decay from high-energy protons ac-

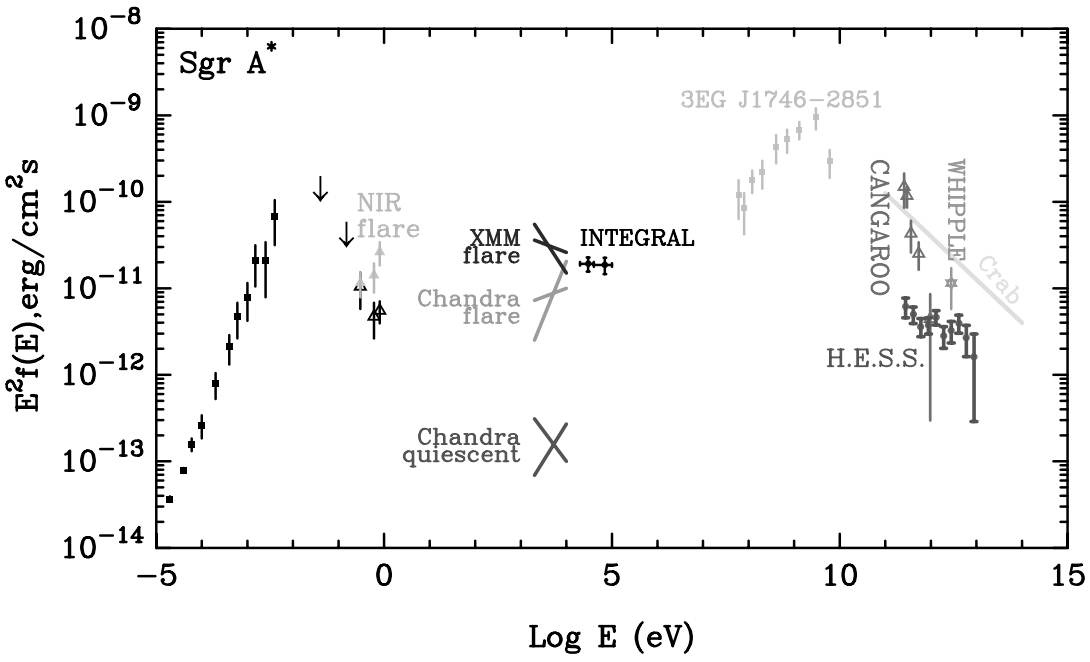

FIGURE 1.3: The various spectral emission components for observations of Sgr A* (figure from Aharonian and Neronov (2005)). This includes measurements in the radio (Zylka et al., 1992), IR (Genzel et al., 2003), X-ray (Baganoff et al., 2003), GeV gamma-ray (Mayer-Hasselwander et al., 1998), and TeV gamma-ray (Kosack et al., 2004; Tsuchiya et al., 2004; Aharonian et al., 2004). The Whipple flux plotted here was from an earlier analysis which resulted in a flux ~ 3 times higher than the actual result (see §1.14 for a full description).

celerated in shocks in the accretion disc (Fatuzzo and Melia, 2003), inverse-Compton up-scattering of lower-energy photons by relativistic electrons accelerated in the disc or a misaligned jet, or inverse-Compton emission from electrons in a plerionic wind termination shock (Atoyan and Dermer, 2004).

Jet-ADAF Model

Various models have been proposed to explain the wide spectrum of emission observed from the Galactic Center (see Figure 1.3), one of which is the coupled

Jet-ADAF model (Yuan et al., 2002), which can explain the radio through X-Ray emission components self-consistently. Though a jet or optically thin accretion disc alone cannot sufficiently explain the observed emission, it is argued that a combination of the two can. In this model, an ADAF around the central black hole is powered by the accretion of surrounding hot plasma. Shocks in the disc accelerate particles very near the black hole ($R \gtrsim 2\ R_s$), a fraction ($\sim 0.5\%$) of which are ejected and transfered to the jet, forming a shock (due to supersonic radial velocities) near the jet's nozzle. Though the exact mechanism for forming a jet is not understood, jets are often seen in other astrophysical objects when there is an accretion disc (e.g. M81). Though there may be vague evidence of an elongated radio structure (Lo et al., 1998), no such jet has been definitively observed in our galaxy, and its existence is postulated solely to explain the complicated multicomponent spectrum of the Galactic Center. In the Jet-ADAF model, the lower-energy radio emission comes from the outer jet region (and, to a lesser degree from the ADAF), while the sub-mm radio fluxes are generated thermally by electrons near the base of the jet. Quiescent and rapid X-ray variability are produced predominantly by synchrotron self-Compton scattering or thermal bremsstrahlung in the nozzle of the jet. If one interprets the X-ray emission as high energy synchrotron emission, one can also account for TeV emission.

Proton Models

Following the assumption that lower-energy emission comes from high-energy electrons accelerated in the accretion disc around Sgr A*, X-ray and TeV emission in the

Galactic Center may also be explained by high-energy protons. Like their leptonic counterparts, protons can be accelerated to very high energies via shock acceleration in an accretion flow very close to the black hole ($R < 10R_s$), producing high-energy photons through several channels: proton-proton interactions, proton-synchrotron emission, and proton-photon interactions.

Proton-proton interactions produce pions ($p + p \rightarrow \pi^{\pm,0} + X$), which decay producing TeV gamma rays (predominantly from direct π^0 decay). The gamma rays produced may then pair-produce leptons ($\gamma \rightarrow e^+ + e^-$), which emit more gamma-rays through bremsstrahlung ($e^- \rightarrow e^- + \gamma$), initiating a cascade. This top-down process will produce a continuum of high-energy emission.

VHE radiation can also come directly from synchrotron emission or bremsstrahlung from high-energy protons ($p + \vec{B} \rightarrow \gamma$) . For synchrotron emission, energies up to a cutoff of $E_{max} \simeq (9/4)\alpha_{fs} m_p c^2 \sim 0.3$ TeV may be produced where α_{fs} is the fine structure constant (Aharonian and Neronov, 2005). Bremsstrahlung can do better, producing energies up to $0.2(B/10^4\,\mathrm{G})^{3/4}\,\mathrm{TeV}$. In both cases, no emission is predicted over a TeV unless the magnetic field strength is on the order of 10^6 G, about four orders of magnitude larger than currently accepted values near the black hole, or if the protons traveling toward us have Lorentz-factors $\gamma > 10$ (Aharonian and Neronov, 2005).

High energy X-ray and gamma-ray emission may also be generated by photo-

meson interactions:

$$\begin{aligned} p + \gamma &\rightarrow p + \pi^0 \rightarrow p + 2\gamma \\ p + \gamma &\rightarrow n + \pi^+ \rightarrow p + e^- + \bar{\nu_e} + e^+ + \nu_e + \nu_\mu + \bar{\nu_\mu} \\ p + \gamma &\rightarrow p + \pi^+ + \pi^- \rightarrow p + e^+ + \nu_e + 2\bar{\nu_\mu} + e^- + \bar{\nu_e} + 2\nu_\mu \end{aligned} \tag{1.4}$$

In this scenario, high-energy protons interact with lower-energy IR photons, again generating neutral pions which decay into gamma-rays. Secondary electrons initiate cascades which may produce TeV photons via the synchrotron Inverse-Compton mechanism.

Black-Hole Plerion Model

Following the discovery of TeV emission by Whipple (Kosack et al., 2004) and HESS (Aharonian et al., 2004), A compelling self-consistent model for the observed radio through TeV gamma-ray emission has been proposed by Atoyan and Dermer (2004). In this model, the radio and sub-millimeter emission is produced close to the black hole in a turbulent magnetized corona. In the accretion disc, advection-dominated accretion flows give rise to the observed X-ray flares and quiescent radio emission. The ADAF's magnetized corona drives a wind of sub-relativistic particles outward in a solid angle of about 1 steradian, which terminates in a shock where electrons become accelerated by the Fermi mechanism to high energies. This concept is very similar to that thought to be at work in pulsar-powered synchrotron nebulae like that of the Crab Nebula, where particles are also accelerated in a wind termination shock. Sources with synchrotron nebulae like the Crab are referred to as *plerions*,

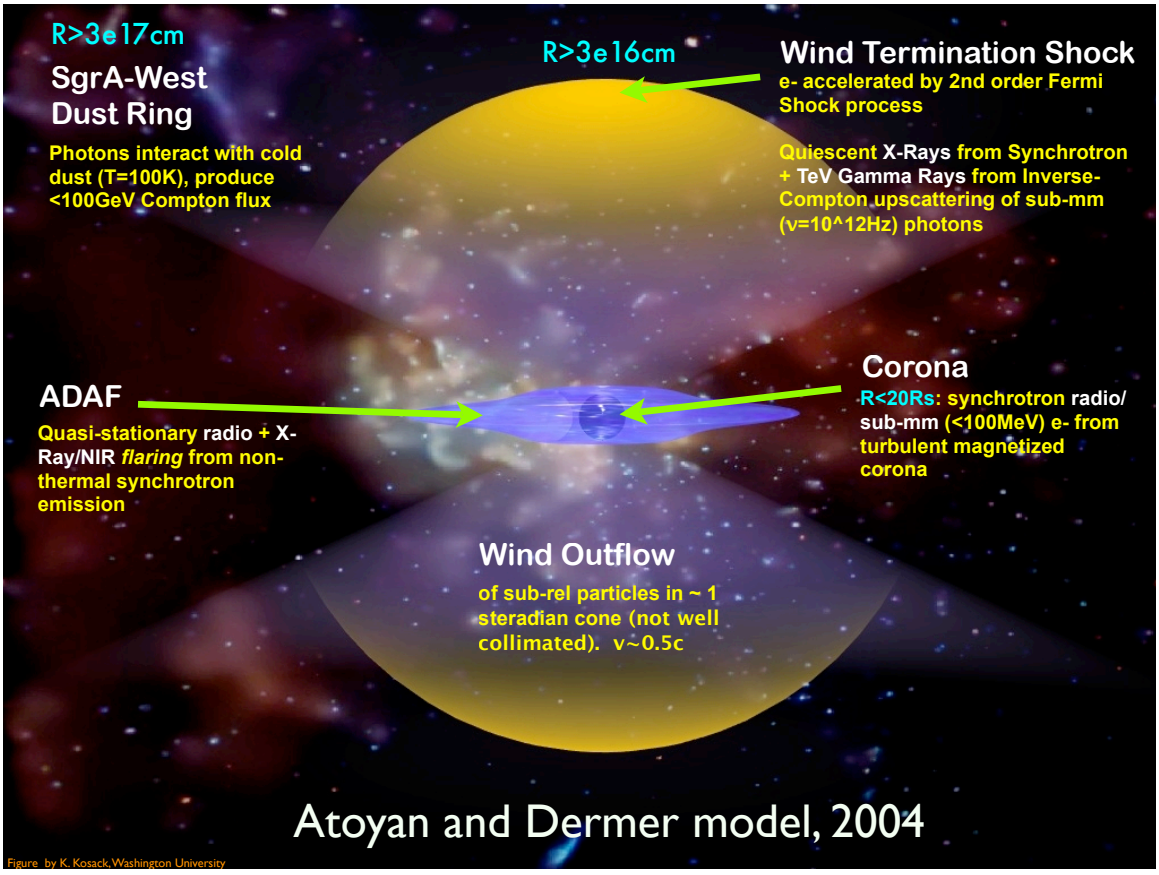

FIGURE 1.4: Black-Hole Plerion model for Galactic Center emission (not to scale), as proposed by Atoyan and Dermer (2004).

which is why this model is referred to as the *black-hole plerion model*. These high-energy particles produce the quiescent X-ray and TeV Gamma-ray emission by Inverse Compton up-scattering of the sub-mm photons, and it is possible the arc-second extent of the quiescent Chandra emission might then be a marginally resolved image of the plerion nebula. Note that if the wind were very collimated, as in a jet, the termination shock would not occur and therefore not produce TeV gamma rays. Some of the high-energy photons then interact with the Sgr A West dust, producing the GeV flux observed by EGRET. This model predicts steady TeV gamma-ray emission, since the gamma rays are produced in an extended region some distance from Sgr A*, but not exceeding the extent of the extended x-ray component (see figure 1.4.)

1.2.2 Light from Dark Matter?

Dark matter provides an interesting possibility for high-energy emission from the Galactic Center region. It is well known that most of the matter in the universe is non-luminous. This can be inferred from galactic rotation curves, which show that the velocities of molecular clouds far from the center of galaxies exceed the expectations for the Keplarian velocity produced by luminous matter. More recently, measurements of the Cosmic Microwave Background point to non-baryonic dark matter that accounts for 30% of the closure density, ten times that of ordinary baryonic matter. Furthermore, the indication that much of the dark matter in the universe may be made up of non-baryonic matter comes from Big-Bang nucleosynthesis and recent measurements of the Cosmic Microwave Background with the WMAP satel-

Parameter	Symbol	Value
Hubble parameter	h	0.73 ± 0.03
Total matter density	$\Omega_{\rm m}$	$\Omega_{\rm m}h^2 = 0.134 \pm 0.0006$
Baryon Density	$\Omega_{\rm b}$	$\Omega_{\rm b}h^2 = 0.023 \pm 0.001$
Non-baryon Density	$\Omega_{\rm nb}$	$\Omega_{\rm nb}h^2 = 0.111 \pm 0.006$

TABLE 1.1: Recent values for various cosmological parameters (Eidelman et al., 2004).

lite, which constrain the baryon density in the universe to be $\Omega_{\rm b}h^2 = 0.023 \pm 0.001$ (Eidelman et al., 2004). Moreover, structure-formation models require that the dark matter is *cold*, or non-relativistic, when galaxies started forming. Collectively, these observations point to a non-baryonic dark halo in all galaxies.

If not baryonic, what could the remaining dark matter be? The current leading theory is that dark matter is made up of a yet-to-be-detected non-baryonic weakly-interacting massive particle (WIMP). To find a viable candidate for such a particle, one needs to go beyond the standard model, to *supersymmetry* or other grand-unified theories that predict new massive, stable, weakly-interacting particles, and look at the thermal history of the early universe. If such a particle were created in large quantities in the big bang, and survived annihilation and decay to the present time, then it would make a natural dark matter candidate.

Assuming there is a stable, weakly interacting particle, χ, created in the big bang, at high-temperatures the particle will be in equilibrium with all other species, with a balance between particle creation and annihilation determining the density. The high-temperature number density, n_χ, will be given by the Boltzmann factor $e^{m_\chi c^2/kT}$.

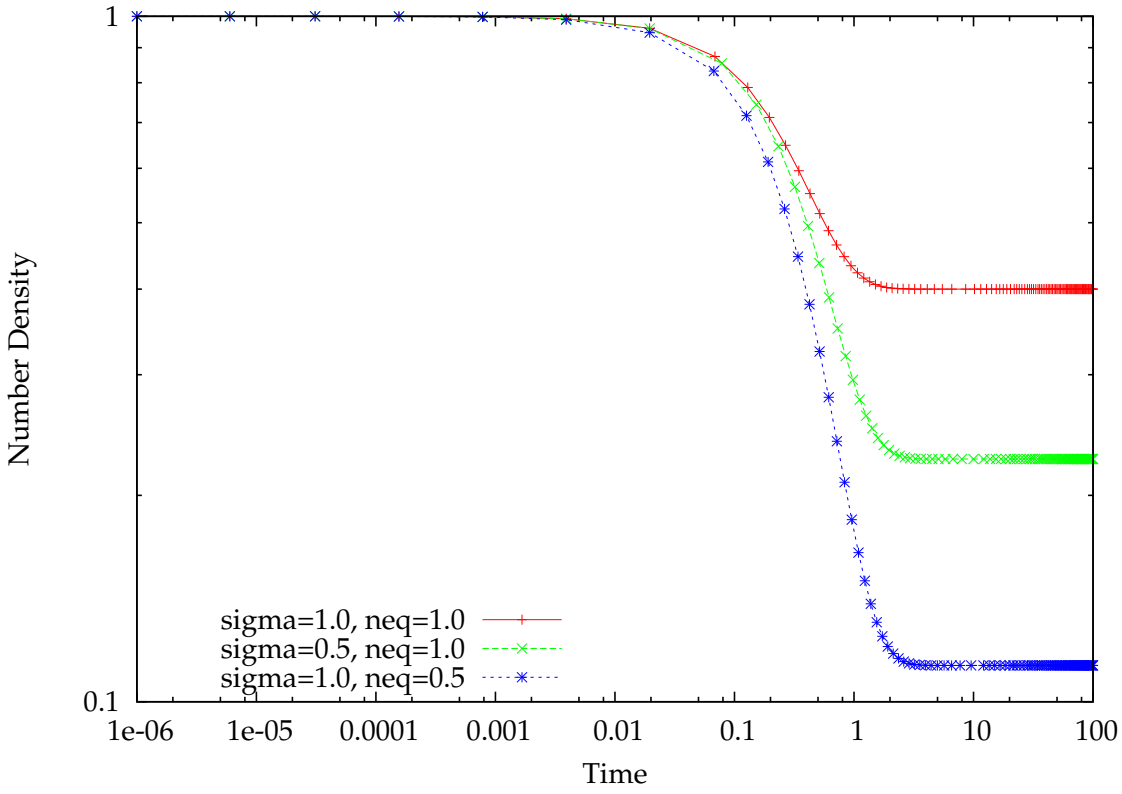

FIGURE 1.5: Plot of the numerically-integrated solution of the Boltzmann equation describing WIMP number density (per co-moving volume) in the early universe (Equation 1.5) for several arbitrary values of the annihilation cross-section and equilibrium number density. The units are arbitrary. Note that after a critical time, the annihilation rate falls to zero due to Hubble expansion and there is a "frozen in" relic density. This relic abundance is heavily dependent on the annihilation cross-section of the WIMP particle. If such a particle exists, simple consideration of the thermal history of the early universe (§1.2.2) shows that the relic density will be typically $\Omega \sim 1$—perfect for explaining dark matter.

As the temperature drops and the annihilation rate falls below the expansion rate, one must turn to the Boltzmann equation to describe the departure from equilibrium or "freeze-out" of the particle species:

$$\frac{\partial n_\chi}{\partial t} + 3H(t)n_\chi = -\langle\sigma_A|\mathbf{v}|\rangle \left[(n_\chi)^2 - (n_\chi^{eq})^2\right] \tag{1.5}$$

where $H(t)$ is the Hubble "constant" describing the acceleration of the universe at time t, σ_A is the annihilation cross-section, n_χ^{eq} is the equilibrium number density, and $|\mathbf{v}|$ is the velocity of the particle. The first term on the right describes WIMP depletion, while the second describes creation. This result is correct for both Dirac and Majorana particles (Jungman et al., 1995). There is no analytic solution to this equation, but it can be integrated numerically, as in Figure 1.5. The annihilation rate, Γ_A, is then proportional to the cross-section by:

$$\Gamma_A \sim n_{eq}\langle\sigma_A|\mathbf{v}|\rangle \tag{1.6}$$

It is important to note that in the early universe, when the WIMPs were relativistic, $H \propto T^2$ and $n_\chi \propto T^3$, where T is the temperature of the universe. Therefore, Γ_A is proportional to some power of T:

$$\Gamma_A|_{early} \sim T^p \tag{1.7}$$

As the universe expands and temperature decreases, the WIMPs become non-relativistic, and their equilibrium number density becomes:

$$n_\chi \sim (m_\chi T)^{\frac{3}{4}} e^{-\frac{mc^2}{kT}} \tag{1.8}$$

so $\Gamma_A(T)$ is an exponentially decreasing function. In either case, $\Gamma_A(T)$ decreases with temperature (and therefore with time). At some critical temperature, $T_f \approx m_\chi/20$, the annihilation rate equals the expansion rate of the universe, and the particle species "freezes out" (Jungman et al., 1995). Thereafter, the number density (per comoving volume) is a constant value called the *relic abundance*. If the freeze out occurs when the WIMPs are non-relativistic, the particles are known as *Cold Dark Matter* (CDM); conversely, *Hot Dark Matter* (HDM) refers to particles frozen in during the relativistic period. The relic abundance has been calculated using entropy density considerations to be:

$$\Omega_\chi h^2 \approx \frac{3 \cdot 10^{-27} cm^3 sec^{-1}}{\langle \sigma_A |\mathbf{v}| \rangle} \tag{1.9}$$

Given a model-dependent WIMP cross-section, σ_A, and the current value for the Hubble parameter (see Table 1.1), Equation 1.9 gives the present-time density of dark matter particles. The inverse dependence on the annihilation cross-section can be understood as follows: particles with larger cross-sections stay in equilibrium longer, and if massive, their number density is Boltzmann-suppressed by a factor of $e^{-m_\chi c^2/kT}$. This gives a negligible relic density unless this cross-section is very small, corresponding to weak interactions. Therefore, the annihilation cross-section is the important quantity to calculate in order to determine if a WIMP will explain the excess dark matter. Interestingly, if we want $\Omega_\chi h^2$ to be in the right range to explain Ω_{dark}, then the cross section must be on the order of weak scattering cross-sections. Moreover, to explain structure formation, massive CDM is required. Thus, any weakly interacting massive particle becomes a natural candidate for the dark matter,

The Minimal Supersymmetric Standard Model (MSSM), an as yet unproven extension of the Standard Model, typically predicts such a new stable, weakly interacting massive particle called the *neutralino*, which has the right theoretical mass range to explain the missing mass in the universe. Even if shown to be incorrect, supersymmetric models can shed some light on the characteristics of non-baryonic dark matter. Since the neutralino is typically a high-mass Majorana particle, it can annihilate with itself producing, among other products, gamma-rays. Accelerators would have seen super-symmetric particles if their masses were smaller than $50-100\,\mathrm{GeV}$, and cosmological constraints (and eventually unitarity) limit the maximum mass to be less than tens of TeV and more naturally $\lesssim 300\,\mathrm{GeV} - 1\,\mathrm{TeV}$ (Ellis et al., 2003). Current dark matter galactic halos calculated for CDM structure formation N-body simulations typically predict a power-law cusp in the density profile near the centers of galaxies, which means that the highest annihilation rate would occur near the gravitational center of our galaxy, or the position of Sgr A*.

Gamma Ray Emission

Neutralinos may emit gamma-rays through several annihilation channels, producing both line and continuum emission as shown in Figure 1.6. Line emission is produced via direct annihilation to gamma rays ($\chi\chi \rightarrow \gamma\gamma$) or by annihilation to a gamma and Z boson ($\chi\chi \rightarrow Z\gamma$). These two lines would be indistinguishable from each other within the spectral resolution of an ACT, and would appear as one line at the mass-energy of the neutralino.

Neutralino annihilation can indirectly lead to electron synchrotron emission. The primary annihilation channel for neutralinos is to quark-antiquark pairs ($\chi\chi \rightarrow q\bar{q}$), which in turn hadronize, forming pions (π^+, π^-, π^0). Neutral pions decay to gamma-rays, while charged pions decay into muons and neutrinos. Since the muons from charged pion decay themselves decay quickly into electrons and positrons which interact with strong magnetic fields surrounding the galactic center, one would expect a continuum of synchrotron photons from this process.

The rate of gamma-ray production from neutralino annihilation is given by:

$$q_\gamma = 2\langle\sigma_A|\mathbf{v}|\rangle n_\chi^2, \tag{1.10}$$

so the density of neutralinos in the Dark Matter halo at the Galactic Center is the most important factor affecting the detectability of gamma rays from this process.

Dark Matter Halo Structure

Since the annihilation rate will depend on how much dark matter there is in a region, a realistic model for the halo density is needed. Typically, the dark matter halo is assumed to be spherically symmetric with respect to the galactic center with a general broken power law density profile of the form:

$$\rho(r) \propto \frac{1}{(r/a)^\gamma \left[1 + (r/a)^\gamma\right]^{(\beta-\gamma)/\alpha}} \tag{1.11}$$

where (α, β, γ) are parameters that define the specific model and a is the scale radius (Bergström et al., 1998). N-body simulations indicate model of $(\alpha, \beta, \gamma) = (1, 3, 1)$

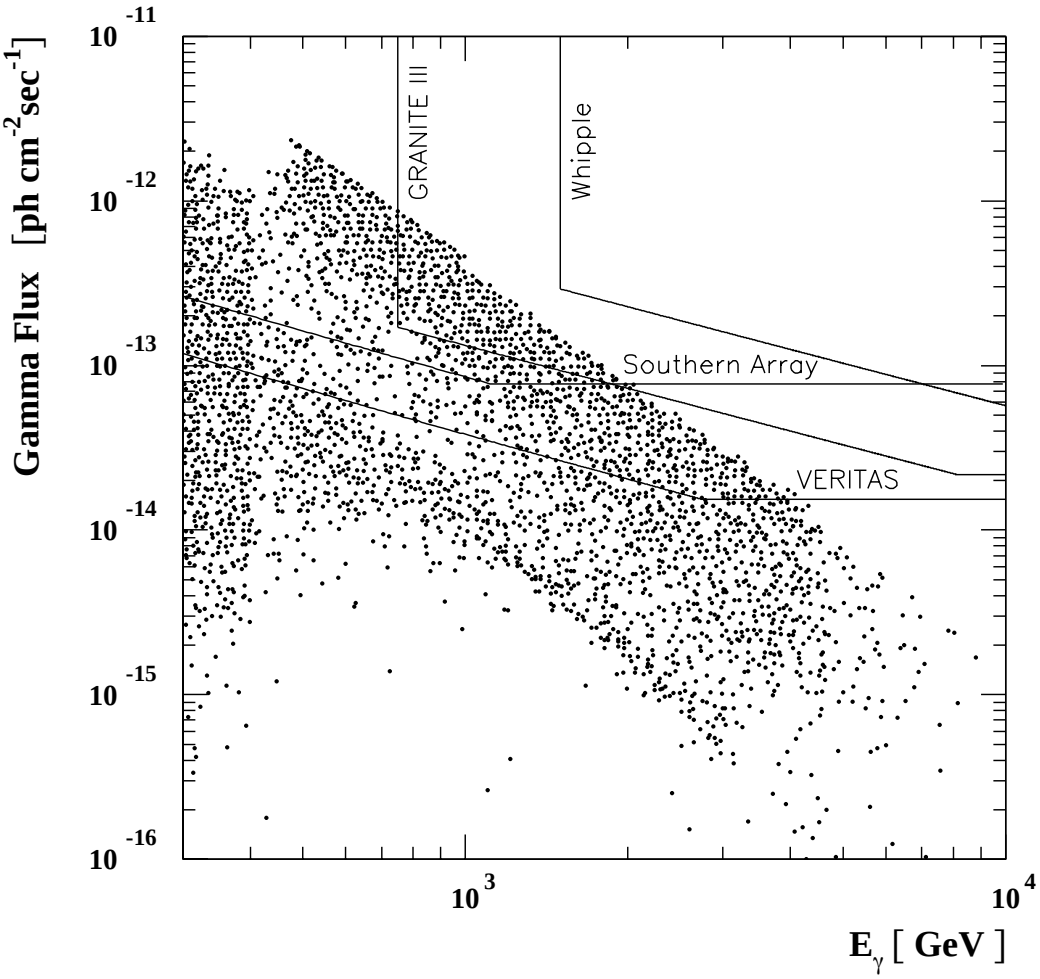

FIGURE 1.6: This figure (from Bergström et al. (1998)) shows the relative sensitivities of ACTs to gamma rays for dark-matter annihilation. Each point corresponds to a different set of model parameters for the neutralino.

(Navarro et al., 1996), giving a profile of

$$\rho(r) = \frac{\rho_c}{(r/r_s)\,(1 + r/r_s)^2} \tag{1.12}$$

where ρ_c is calculated from the knowledge that $\rho(r_0)$ (the density at the Solar System's distance from the Galactic Center) is 0.3 GeV cm^{-3} and the scale-radius $r_s \sim 10 - 20$ kpc. The interesting feature of this profile is that there is a power-law *cusp* ($\rho(r) \propto r^{-1}$ (Navarro et al., 1996) to $r^{-1.4}$ (Moore et al., 1998)) that may continue down to distances very close to the GC ($r \to 0$) (Navarro et al., 1996). If this model is correct, the number density of neutralinos near the galactic center may be high enough that the annihilation emission is detectable.

Observability

By assuming a value for $\Omega_\chi \sim \Omega_{dm}$, it is possible to calculate the flux of the dark matter annihilation photons at Earth. The relic density has been calculated for a number of super-symmetric particle theories (see e.g. Ullio and Bergström, 1998) and has been constrained to be in the range $0.025 < \Omega_\chi h^2 < 1$. From this we can calculate $\langle \sigma_A |\mathbf{v}| \rangle$.

The intensity will be proportional to the square of the density, so the total intensity at angle θ will be given by the line-of-sight integral:

$$I(\theta) \propto \int_0^\infty \rho(r)^2 ds \tag{1.13}$$

$$r = \sqrt{R^2 + s^2 - 2Rs\cos(\theta)}$$

where R is the distance from the observation point to the center of the galaxy, r is the radial distance of an element of the dark halo to the Galactic Center, and s is the line-of-sight distance. What we really want is the integrated flux over a small solid angle representing the field of view of a telescope,

$$\Phi = C \cdot (2\pi) \int_{\theta_{min}}^{\theta_{max}} I(\theta) d\theta \tag{1.14}$$

where

$$C = 3.7 \cdot 10^{-13} \left(\frac{\langle \sigma_A |\mathbf{v}| \rangle}{10^{-29}\ \mathrm{cm}^3\ \mathrm{s}^{-1}} \right) \left(\frac{100GeV}{m_\chi} \right)^2$$

This gives an idea of what the signal intensity should look like to a gamma-ray telescope on Earth. The signal itself would be in a frequency range near the mass of the neutralino (which is somewhere between 300 GeV and 10 TeV). Note that the strength of the annihilation line, $\langle \sigma_A |\mathbf{v}| \rangle$, is calculated based on the one-loop process as described in Jungman and Kamionkowski (1995). This cross-section contains additional uncertainties compared with the total annihilation cross-section since it is not as closely tied to the relic density. The spectrum of the emission is complicated, and must be derived by detailed Monte-Carlo simulation. Typically, one assumes a spectrum of the form $d\Phi/dE \propto E^{-1.5} \exp(E/E_c)$, where the cutoff energy E_c lies a factor of 10 below the neutralino mass ($\sim 0.1 m_\chi$) (Bergström et al., 1998)

Chapter 2

Experimental Technique

All data presented in this dissertation were taken using the Whipple 10m Gamma-ray Telescope in Amado, Arizona. The Whipple group pioneered the *Imaging Atmospheric Čerenkov Technique* to detect VHE gamma rays, that is used in a variety of ground-based gamma-ray telescopes today. The observations of the Galactic Center, which transits at very low elevation at Arizona's latitude, presented multiple challenges that required improvements on the standard techniques used for analyzing the Whipple data. In this chapter, I describe the Atmospheric Čerenkov technique, the standard procedure for data analysis, and the improved techniques for data selection developed for large-zenith-angle observations of the Galactic Center.

2.1 Atmospheric Čerenkov Telescopes

Unlike lower-energy photons, gamma rays cannot be focused using reflective or refractive optics, so their detection relies on techniques that are more familiar in

high-energy particle physics experiments than in traditional astronomy. Further complicating the matter, Earth's atmosphere is opaque to high energy radiation, which while fortunate for those of us who live on the planet's surface, would initially seem to make ground-based gamma-ray astronomy impossible. However, the atmospheric absorption of gamma rays is actually an advantage: though gamma rays themselves do not make it to the ground, their interactions produce a shower of secondary particles whose presence can be detected at ground level. The idea of using the Earth's atmosphere as part of a gamma ray detector—as a Čerenkov radiator—is the basis for an *Atmospheric Čerenkov Telescope*, or ACT. Unlike optical telescopes, which detect photons directly, ACTs work by imaging the faint UV/blue flashes of Čerenkov light emitted by secondary particles in a gamma-ray-induced air shower and reconstructing the energy and direction of the original photon. This technique provides a telescope with a typical field of view of several degrees, sub-arcminute angular resolution, and a much larger effective collection area than could be achieved with direct detection.

Though not the first detector designed to detect VHE gamma rays by collecting Čerenkov photons produced in air showers, the Whipple Observatory's 10 meter ACT, constructed in 1968, was the first one to be successful (Weekes, 2003). It wasn't until 1989, however, after the development of the Atmospheric Čerenkov *Imaging* Technique (discussed later in §2.2), that the first positive detection of gamma-ray emission was made by this telescope (Weekes et al., 1989). The first source detected was a pulsar-powered supernova remnant, the Crab Nebula. This source has become the "standard candle" of gamma-ray astrophysics due to its bright, steady emission.

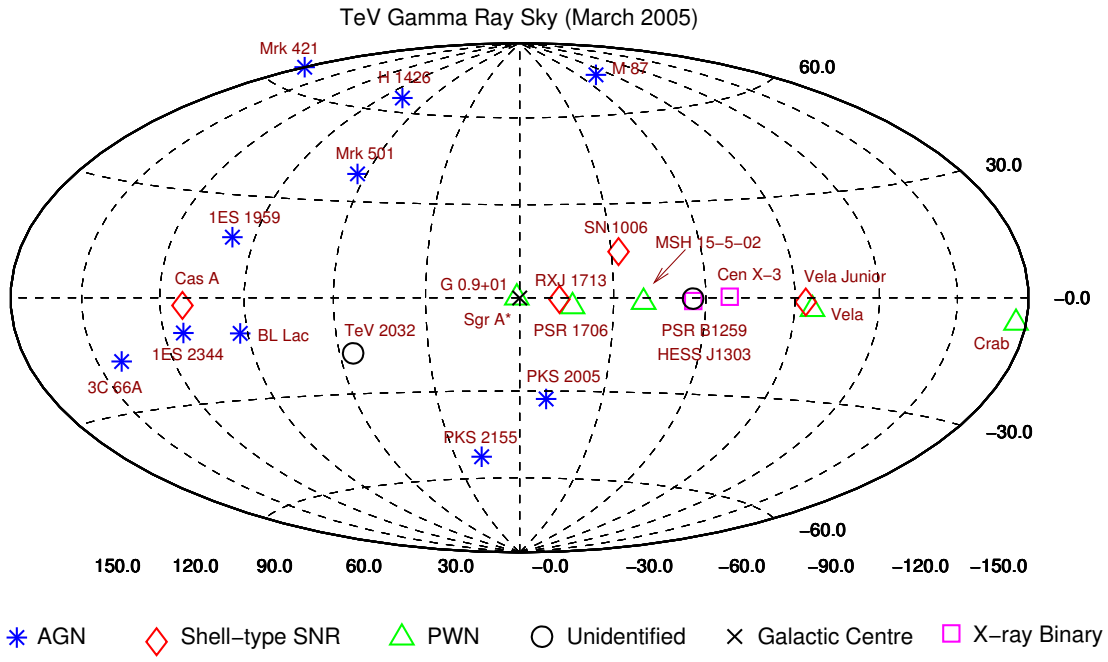

FIGURE 2.1: Sky-map of gamma-ray sources detected by ACTs (Kildea, 2005)

Since the initial detection, the Whipple 10m has been improved and upgraded many times, and the imaging technique re-optimized on both the Crab Nebula data and detailed Monte Carlo simulations. Atmospheric Čerenkov telescopes have now detected perhaps half a dozen extra-galactic sources and about 15 galactic sources (see Figure 2.1). With the advent of next-generation instruments like HESS, MAGIC, CANGAROO, and VERITAS, we can expect that number to grow rapidly over the coming years.

2.1.1 Air-Shower Physics

The Earth is constantly being bombarded with very high-energy (VHE; $E > 600$ GeV) particles, the largest fraction of which are cosmic-ray protons and heavier nuclei. When high-energy particles enter the Earth's atmosphere, they interact with the surrounding nuclei, producing a cascade of secondary pions, nuclear fragments, penetrating $\pi^{+/-}$ decay muons and secondary electromagnetic showers. Primary high-energy gamma rays can pair-produce in the presence of the nuclear field of an atom of atmospheric gas, giving rise to a single electromagnetic cascade. Collectively, these cascades are referred to as *extensive air showers*. Since both gamma-ray photons and cosmic-ray particles produce air showers (Figure 2.2), differentiating between these two types becomes the primary goal of analyzing data from an Atmospheric Čerenkov Telescope. For the brightest sources, gamma rays constitute only a fraction of a percent of the detectable cosmic-ray flux, making the task of detecting gamma rays like finding a needle in a haystack.

Gamma-Ray-Induced Air Showers

The dominant interaction of a very high energy photon in air is pair-production ($\gamma \rightarrow e^+e^-$), which may occur when a gamma ray encounters the Coulomb field of a nucleus[1] . In the limit where the photon energy $E = \hbar\omega$ satisfies $E/(m_e c^2) \gg$

[1] pair-production from photons in free space is forbidden due to the conservation of energy and momentum.

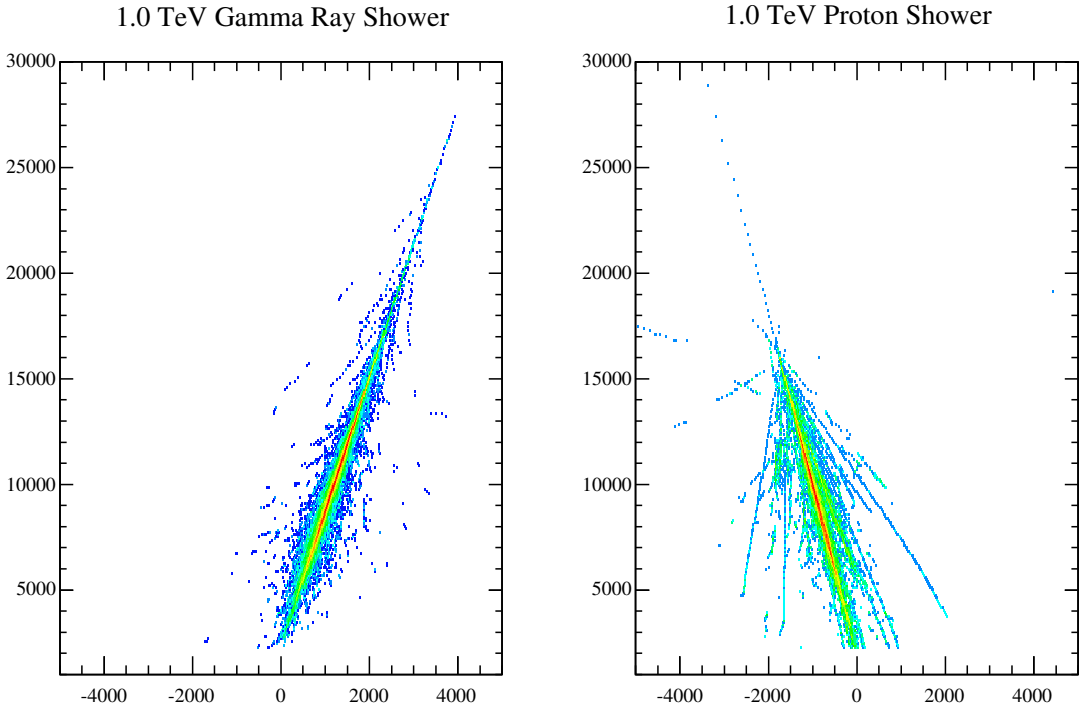

FIGURE 2.2: The plot on the left shows the particle tracks (electrons and positrons) for an electromagnetic air shower produced by a 1 TeV gamma-ray. On the right is a hadronic shower from a 1 TeV proton. The axes are labeled in meters from an arbitrary position at sea-level. The color values are an indication of particle number density. The particle tracks plotted in this figure were produced using the `kascade7` particle air-shower simulation.

$1/(\alpha Z^{\frac{1}{3}})$, the cross-section for pair production becomes a constant:

$$\sigma_{pair} \rightarrow \alpha r_e Z^2 \left[\frac{28}{9}\ln\left(\frac{183}{Z^{\frac{1}{3}}}\right) - \frac{2}{27}\right]\frac{\mathrm{m}^2}{\mathrm{atom}} \tag{2.1}$$

and the rate of energy loss is proportional to E. Here, r_e is the classical electron radius ($e^2/(4\pi\epsilon_0 m_e c^2)$), Z is the charge of the nucleus with which the photon is interacting, and α is the fine structure constant (Longair, 1992, p.118). The opening angle for pair production is approximately $\theta_{pair} \sim 1/\gamma$, where γ is the Lorentz factor of the secondary electron and positron ($\gamma = E_\gamma/m_e c^2$). The electron and positron then undergo subsequent interactions with the atmospheric nuclei, producing more gamma rays by bremsstrahlung. Once again, the rate of energy loss is proportional to energy and can be written as:

$$\frac{dE}{dX} = \frac{-E}{X_0} \tag{2.2}$$

where X is the pathlength in g cm^{-2} ($X = \int \rho(z)dz$) and $X_0 = 36.6$ g cm^{-2} is the "radiation length" in the atmosphere. Thus, a radiation length X_0 is the pathlength over which an electron loses $1 - e^{-1}$ of its energy. It turns out that this is also the distance over which a photon has a 7/9 probability of pair-producing. So, on average the number of secondary electrons, positrons, and gamma rays roughly doubles every X_0.

One usually assumes an exponential (standard) atmosphere with scale height $h \simeq 8.5$ km, where the density is given by $\rho(z) = \rho_0 e^{-z/h}$. Thus, the height of the first interaction, z_1, is found by integrating $X_0 = \int_{z1}^{\infty} \rho_0 e^{-z/h} dz$, giving:

$$z_1 = -h\ln\left(\frac{X_0}{h\rho_0}\right). \tag{2.3}$$

Therefore, when a VHE gamma ray hits Earth's atmosphere, it interacts within a mean-free-path ($\lambda_{pair} = 1/(n\sigma_{pair})$) of 9/7 $X_0 = 47.05\text{g cm}^{-2}$, corresponding to a height of approximately 20 km above sea-level. This initiates an *electromagnetic cascade* in which the resulting electrons and positrons re-radiate gamma-rays through bremsstrahlung, which in turn pair-produce more particles, and the process repeats (see Figure 2.3). As more particles are created, the initial energy of the gamma ray is spread out until the rate of bremsstrahlung energy-loss falls below the rate of ionization loss and the air-shower dies out. This occurs at a critical energy, $E_c \simeq 80\ MeV$. shower reaches this point, in a single radiation length, the electrons lose all of their energy and the shower ceases.

Defining $t \equiv X/X_0$ (the number of radiation lengths traversed), the number of particles $n(t) \propto 2^t$ and the average energy of each particle is $E_0/2^t$ (where E_0 is the energy of the primary gamma-ray). Since the cross-section (and therefore mean-free-path) for pair production is roughly equal to that of bremsstrahlung in the relativistic limit, approximately 2/3 of the particles are electrons or positrons, while the remaining 1/3 are gamma-ray photons. The largest fraction of the particles in an air-shower are produced at pathlength X_{max} (called "shower-max"), which corresponds to an altitude of 7 to 10 km. The altitude (z_{max}) and number of particles (N_{max}) at X_{max} is therefore energy dependent (see Table 2.1.) These showers are well-collimated, having maximum spread proportional to $m_e c/E$ radians from the primary direction.

Energy	X_{max} ($g\ cm^{-1}$)	z_{max} (km)	N_{max}
10 GeV	175	12.8	$1.6 \cdot 10^1$
100 GeV	261	10.3	$1.3 \cdot 10^2$
1 TeV	346	8.4	$1.1 \cdot 10^3$
10 TeV	431	6.8	$1.0 \cdot 10^4$
100 TeV	517	5.5	$9.3 \cdot 10^4$

TABLE 2.1: Shower characteristics for several primary gamma-ray energies. Data from (Weekes, 2003), p 15.

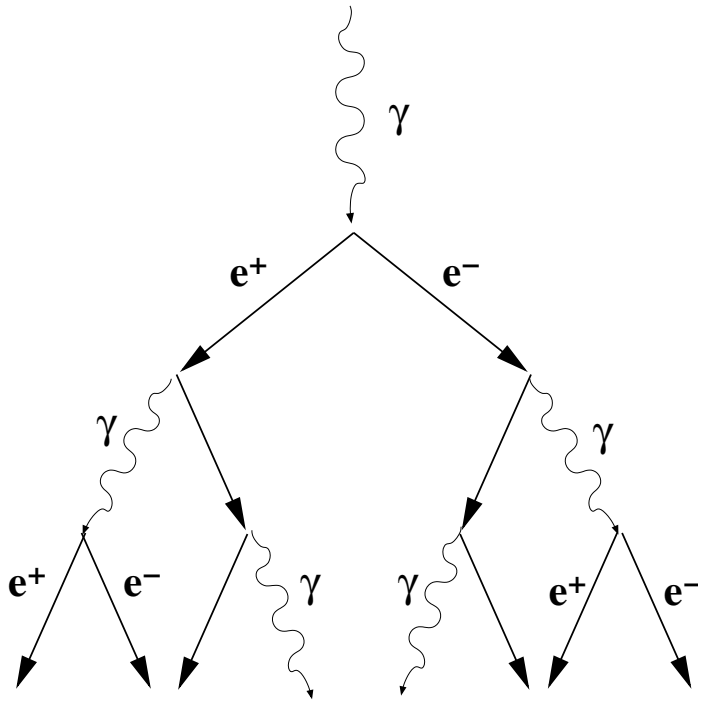

FIGURE 2.3: Simple model for a gamma ray induced air-shower. The primary gamma ray interacts in the atmosphere, starting an electromagnetic cascade. The electrons and positrons produced in the interaction emit more gamma rays via bremsstrahlung, which pair-produce electrons and positrons. The process continues until the threshold for pair-production is reached and the shower dies out.

Cosmic-Ray-Induced Air showers

Gamma rays are not the only high energy particles that interact in the upper atmosphere—cosmic rays, which are primarily protons, may also generate extensive air showers. In fact, even for the strongest gamma-ray sources, cosmic-ray-induced air showers outnumber gamma-ray showers by a factor of roughly 10^3, which means that the process of detecting gamma rays in the atmosphere is typically heavily background-dominated. The air-shower produced by a cosmic-ray primary (a *hadronic cascade*) closely resembles that which is produced by a gamma-ray. When a cosmic ray interacts, it produces a variety of secondary particles, many of which are pions ($\pi^{\pm}, \pi^0$), which decay into muons and gamma rays, producing further electromagnetic cascades (see Figure 2.4). Fortunately, the differences in shower development between gamma and cosmic-ray particles are differentiable—the angular extent of a cosmic-ray shower is spatially broader and less smoothly distributed than that of a gamma-ray shower due to the multiple overlapping electromagnetic showers that are produced. The angular shape of the Čerenkov light image of the shower is the primary factor used to discriminate between electromagnetic and hadronic cascades in a ACT.

Čerenkov Light from Extensive Air Showers

When a charged particle moves through a dielectric medium, it polarizes surrounding nuclei, causing them to oscillate as they return to their equilibrium position. For low particle velocities, the electromagnetic fields generated by this process cancel each

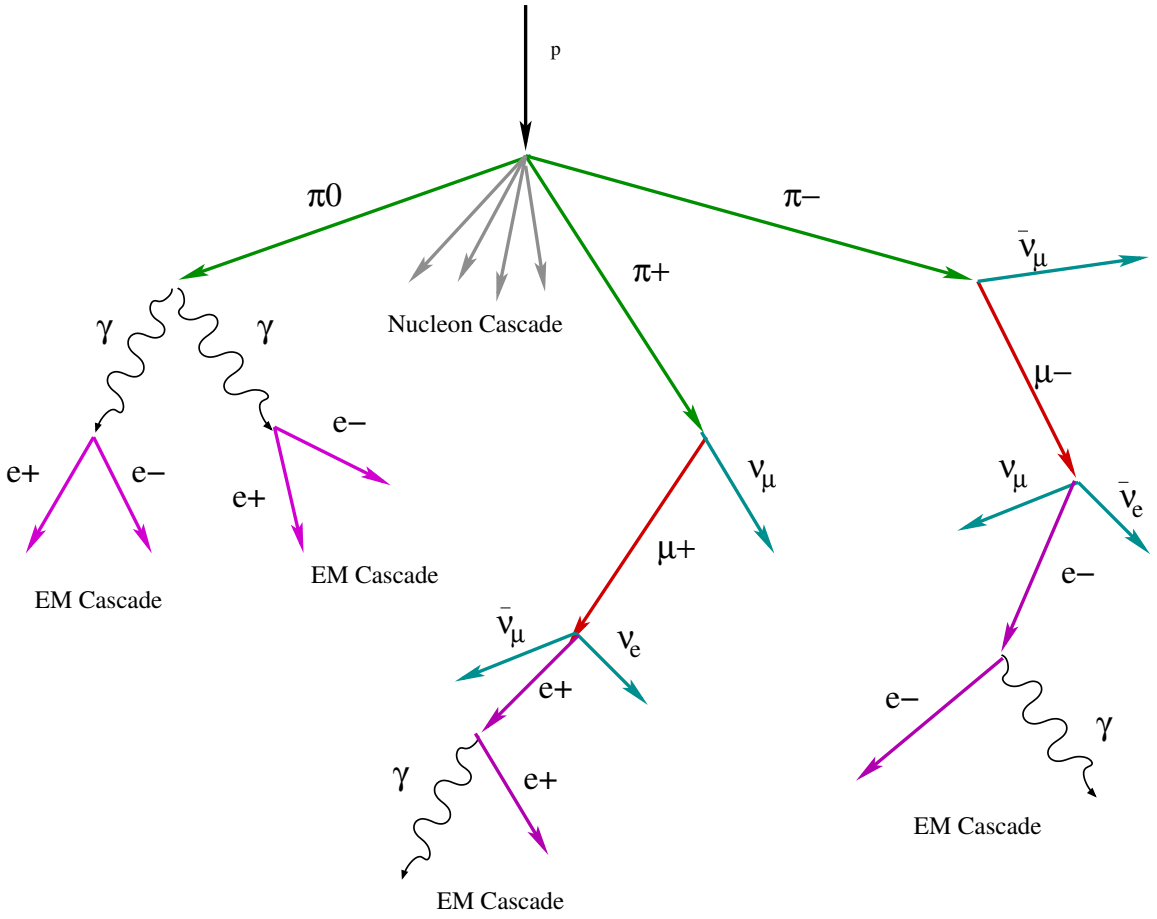

FIGURE 2.4: A model of a cosmic-ray-induced (hadronic) air-shower. (Figure adapted from (Jelley, 1958))

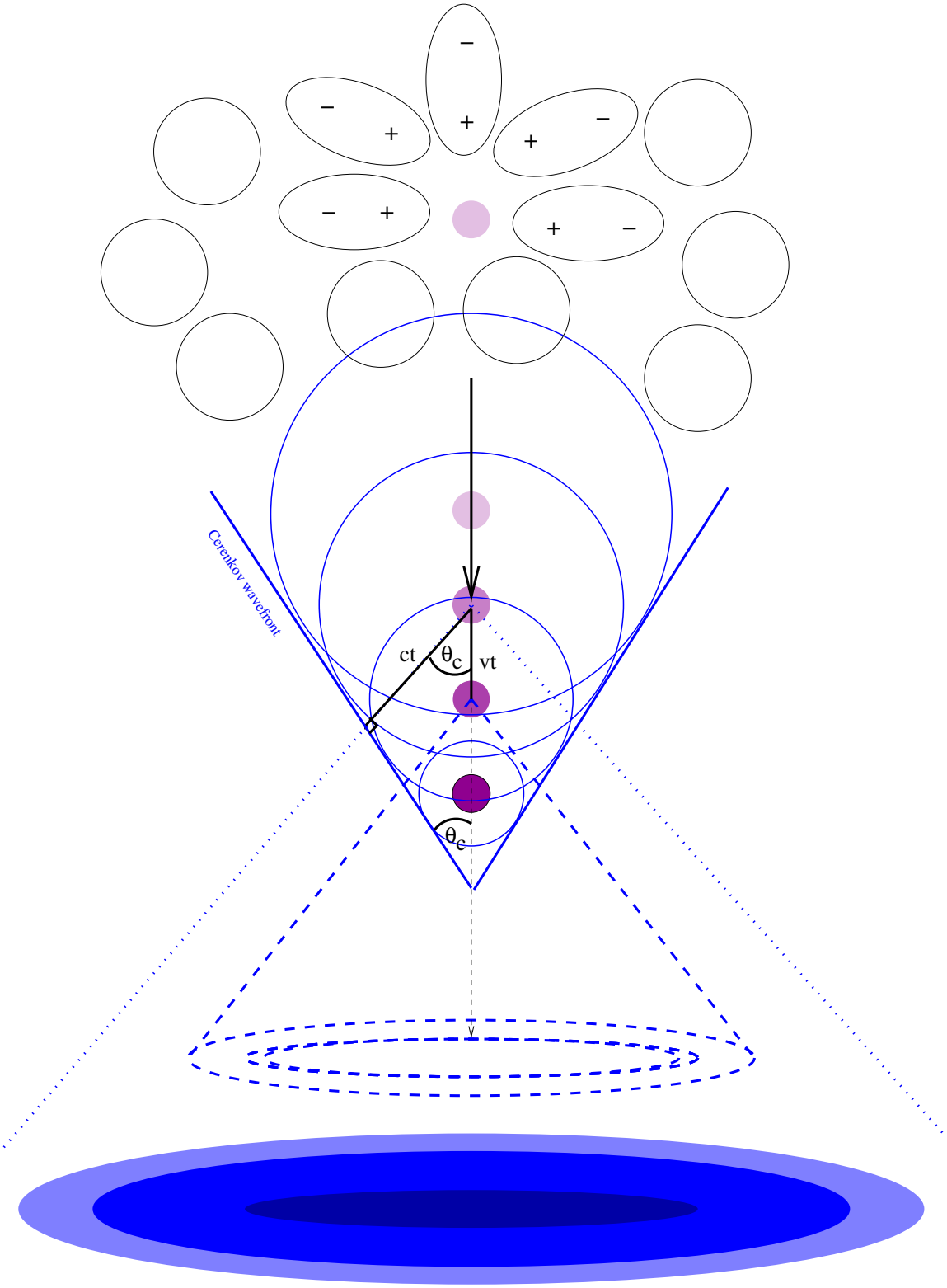

FIGURE 2.5: Čerenkov radiation is emitted in nested cones from a single charged particle traveling faster than the speed-of-light in a medium.

other out, producing no net field and thus no radiation. However, when a charged particle has a velocity greater than the speed of light in the medium ($v > c_{\rm medium}$), the fields created by the oscillation interfere constructively and satisfy the conditions for radiation at a specific angle from the particle's trajectory. The emitted radiation is known as *Čerenkov* light[2] , and the Čerenkov angle (θ_c) can be derived classically from the simple interference diagram shown in Figure 2.5, as:

$$\theta_c = \cos^{-1}\left(\frac{c_{\rm m}t}{vt}\right) = \cos^{-1}\left(\frac{1}{\beta n}\right), \tag{2.4}$$

where $c_{\rm m}$ is the speed of light in the medium (c/n), and n is the index of refraction of the medium. The physical interpretation of this diagram is that along the wavefront, the effect of the retarded potential is such that the dipoles created by the polarized atmosphere oscillate and radiate in phase at θ_c (Jelley, 1958). In the atmosphere, which has an index-of-refraction of $\sim$ 1.0003 (at sea-level), the Čerenkov angle is $\theta_c \sim 1.4^\circ$ with an electron threshold energy for Čerenkov photon production ($E_t \simeq m_0c^2[1/\sqrt{2(n-1)}-1]$) of about 21 MeV. At higher altitudes, the air density is lower, resulting in a smaller index-of-refraction and therefore a smaller Čerenkov angle.

The number of Čerenkov photons emitted per pathlength (dx) per frequency interval ($d\lambda$) for a charged particle with charge Ze is:

$$\frac{dN^2}{\partial x \partial \lambda} = \frac{2\pi\alpha Z^2}{\lambda^2}\left(1 - \frac{1}{\beta^2\, n^2(\lambda)}\right) \tag{2.5}$$

where α is the fine-structure constant, and $n(\lambda)$ is the frequency-dependent index-

[2] Named for I. Čerenkov who discovered it. Čerenkov , along with Frank and Tamm, who came up with the classical theory explaining the emission, won the Nobel prize in 1958

of-refraction. For electrons, this can be integrated to obtain the number of photons emitted in the frequency range (λ_1, λ_2) over a distance l:

$$N = 2\pi\alpha l \left(\frac{1}{\lambda_2} - \frac{1}{\lambda_1}\right)\left(1 - \frac{1}{\beta^2\, n^2(\lambda)}\right) \tag{2.6}$$

Equation 2.5 is proportional to $1/\lambda^2$, leading to emission predominantly in the UV end of the visible spectrum (Jelley, 1958).

In an extensive air-shower, an ensemble of charged particles is created that are moving faster than the speed of light in the atmosphere, each emitting Čerenkov light with an emission spectrum that peaks in the UV-blue range due to atmospheric absorption and scattering. Since the trajectories of the electrons and positrons in the shower are also deflected by multiple Coulomb-scattering, the end result has a footprint of roughly $R \sim 8\,\mathrm{km} \cdot (1.3^\circ/60)$. Within this radius, the shower appears as a faint elliptical shaft of UV/blue light, lasting on average 20ns. The photons that hit the ground (at an altitude of 2 km) are concentrated in a "light pool" of approximately 120 m radius with a typical photon density on the order of 100photons m^{-2} (see Figure **??**). The peak intensity of the light pool occurs near the edge due to geometric effects and changes in the atmospheric index-of-refraction, as shown in Figures 2.6 and 2.7.

For a gamma-ray-induced shower, the lateral angular width of the Čerenkov light image is predominantly determined by the Coulomb scattering angle. This gives an angular size of approximately $\theta \sim R_m/h_{max}$, where R_m is the Molière radius (a characteristic property of multiple Coulomb-scattering that depends on the material composition), and h_{max} is the height of the shower-max position. The longitudinal

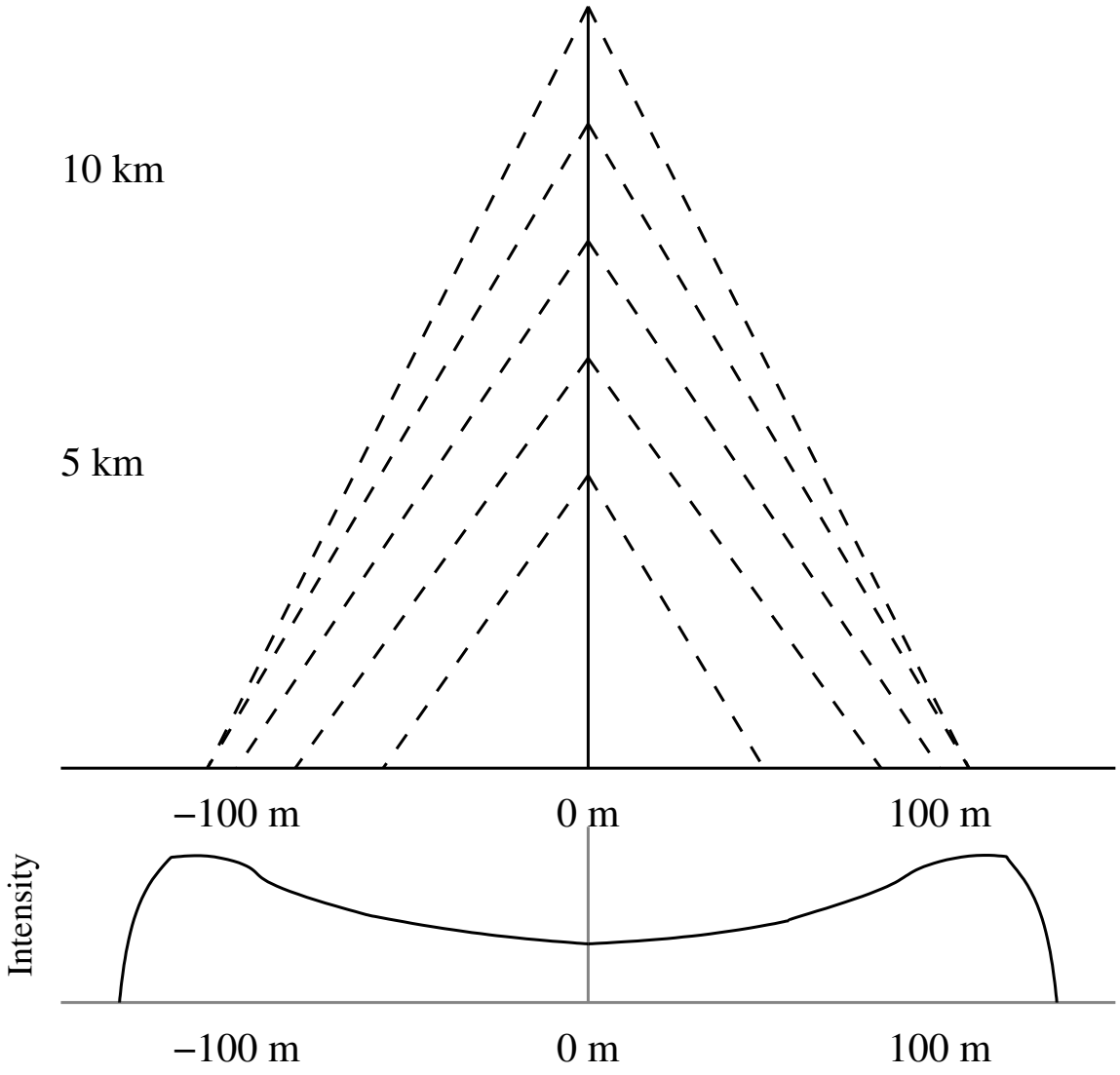

FIGURE 2.6: This diagram shows the Čerenkov light intensity from particles near the shower-max ($\sim 6-10\,\mathrm{km}$) on the ground as a function of radius. The top figure shows the conical Čerenkov light emission at various points in the atmosphere, resulting in an intensity profile that peaks near the edge of the light pool. This is due to variations in the atmospheric index-of-refraction, which alter the Čerenkov angle.

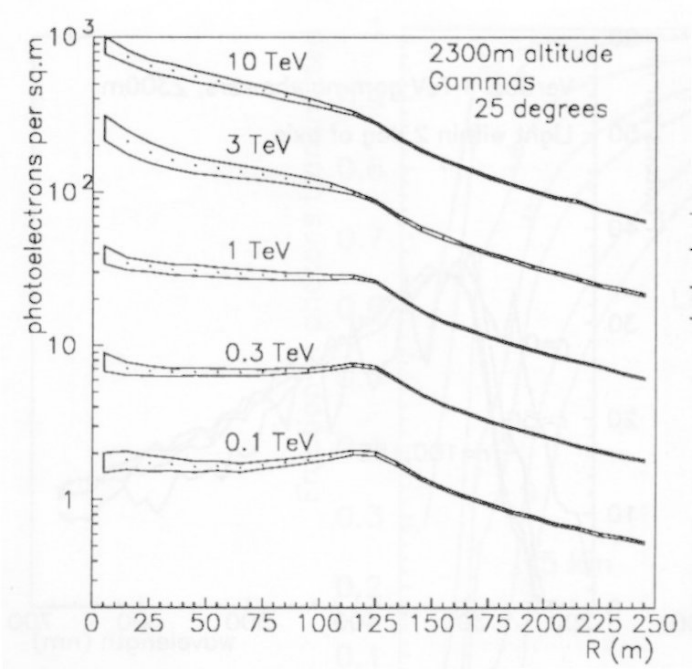

FIGURE 2.7: This diagram (from Hillas et al.) shows the lateral distribution of Čerenkov light on the ground as a function of radius. The light peaks at a distance of roughly 120 m for incident energies under about 1 TeV, and then falls off.

spread of the light from a shower is dependent both on the Coulomb spread and the longitudinal development of the shower ($n(t) \sim 2^t$). The lateral and longitudinal extents of the emission determine the required field of view ($\sim 3^\circ$) and resolution ($\sim 0.1^\circ$) for an ACT.

The number of Čerenkov photons produced in a gamma-ray shower is proportional to the number of particles in the shower $n(t)$. Since the average energy per particle, $\langle E \rangle \propto E_0/n(t)$, the number of particles at shower-max will be proportional to E_0/E_c. Therefore, to first-order, the energy of the primary is directly related to the brightness of Čerenkov photons observed at ground-level. However, there is also a dependence on the impact-parameter of the shower and on the zenith angle; in §2.5, techniques for extracting the primary energy from ACT observations (correcting for these parameters) and for calibrating the absolute energy scale are discussed.

The shower geometry is also zenith-angle dependent. Figure 2.8 shows the particle tracks from a simulated 1 TeV gamma-ray shower observed at a range of zenith angles. As the zenith angle (ϑ) increases, the distance to the shower maximum position increases, the angular extent becomes correspondingly smaller (approximately as $\cos\vartheta$) and the light pool on the ground becomes larger and fainter. These effects on the shower's angular extent must be taken into account when analyzing data from an ACT, and are discussed in §2.3.2.

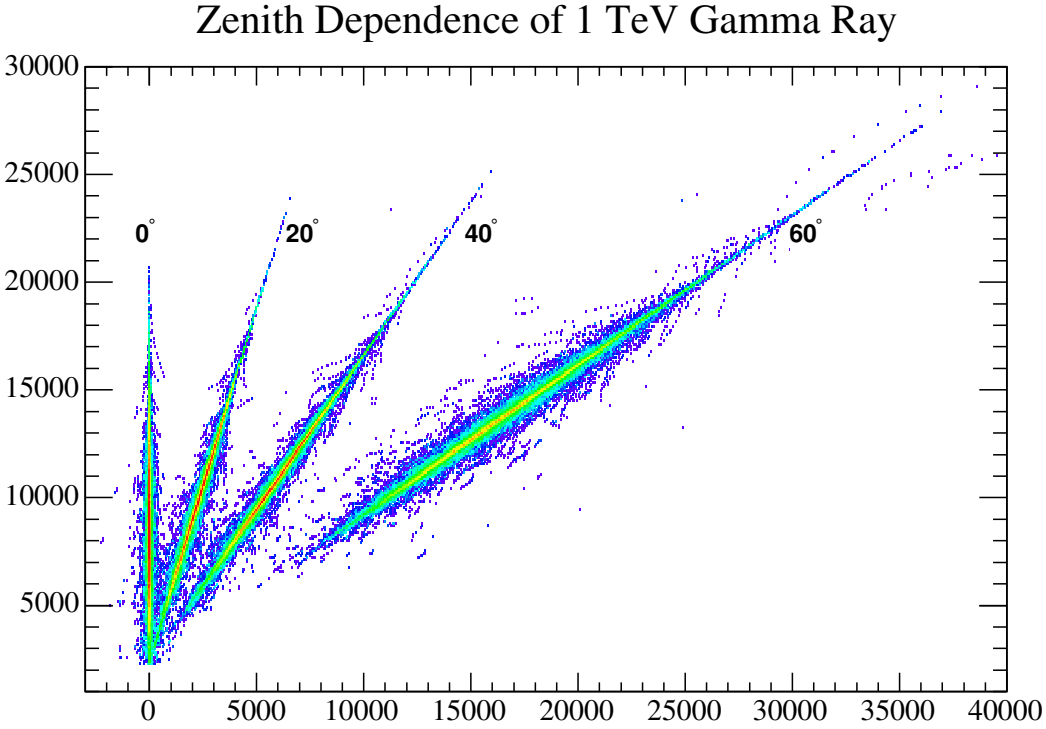

FIGURE 2.8: Particle tracks for a simulated 1 TeV gamma ray shower at multiple zenith angles. The axes are labeled in meters and the color value shows the number density of particles (electrons and positrons) at that position.

FIGURE 2.9: The Whipple 10m Telescope, in its parked position.

2.1.2 Whipple 10m Telescope Description

Optics

The Whipple telescope consists of a spherical, ten meter optical reflector with a 7.3 m focal length (f/0.73) made up of many smaller (73 cm diameter) mirror facets arranged in a Davies-Cotton configuration, where the radius of curvature of the optical support structure is equal to the focal-length of the telescope—one half of the radius of curvature of the individual mirror facets (Davies and Cotton, 1957). This design reduces coma (the dominant off-axis aberration), but makes other aberrations worse. However, this design compromise gives the requisite $< 0.1 - 0.2^{\circ}$ resolution across the entire 3° field of view. Since imaging Čerenkov light from air-showers only requires an angular resolution on the order of arc-minutes and a field-of-view of a couple of degrees, the optics need not be as accurate as typical astronomical telescopes.

Camera

Optical photons are focused by the mirror facets into a camera made of highly sensitive photomultiplier-tube (PMT) pixels, which are capable of detecting single photons in the visible/UV waveband (see Figure 2.10). The angular size of the camera pixels, $\sim 0.2^{\circ}$ (see Table 2.2), is picked to correspond with the resolution needed to resolve a gamma-ray-induced air shower. The circular pixels are arranged in a hexagonal-close-packed pattern to minimize the space between them and are fitted with a series of *light-cones* which reflect photons falling into the dead spaces into the

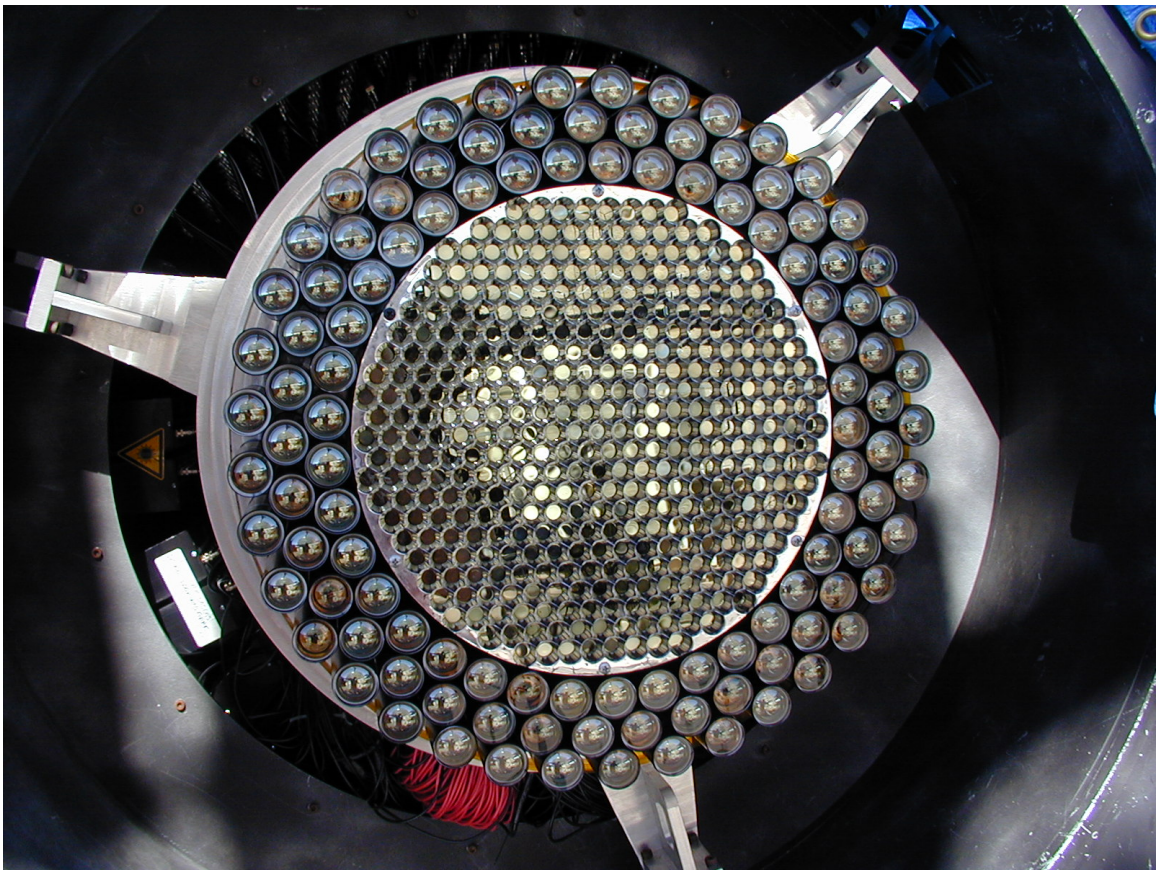

FIGURE 2.10: An image of the Whipple telescope's 379-pixel camera, showing the focal plane and light-cones. The ring of larger-sized phototubes around the central area is not currently used.

		Field-of-View (°)	
Season	N_{pix}	**Pixel**	**Total**
1993-1996	109	0.26	3.0
1996-1997	151	0.26	3.5
1997-1999	331	0.26	4.8
1999-2003	379	0.12	2.8

TABLE 2.2: Whipple camera geometry evolution.

nearest PMT. Throughout its lifetime, the Whipple camera has undergone a series of upgrades, which have increasing the camera area, field-of-view, and resolution (see Table 2.2). Since the data presented in this thesis cover this entire period, we describe methods by which we correct the varying pixel spacing and calibrate for each camera (see Sections 2.3.2 and 3.1).

Whipple Electronics

The Whipple telescope operates in a triggered mode—it only stores digitized data when a shower-like "event" appears in the camera. When this happens, the image of the event in the camera is digitized and stored by the data acquisition system for later offline analysis. To determine what constitutes an event, there is a two-level trigger system. In the first level, the signal for each PMT pixel is split and fed into both the "pixel trigger", where a constant fraction discriminator (CFD) attached to each pixel fires when the signal in the pixel goes above a preset fraction of its peak value, and through a delay line to a gated *charge analog-to-digital converter* (QADC). In the second trigger level, the CFD output pulses are fed into a "pattern" trigger,

which requires N adjacent pixels (N is typically 3) to fire within a short time window to gate the QADCs and initiate the telescope readout.

Since both electronic noise and night-sky background light can cause accidental triggers of the telescope and vastly increase the data rate, the trigger thresholds are set just above these background noise levels by looking at a *bias curve*, or trigger rate-vs-threshold plot for the system (see Figures 2.11 and Table 2.3). Additionally, camera pixels which contain light from bright stars in the field of view during observations are manually turned off to reduce the accidental trigger rate. The operating threshold is a compromise between the need to increase the trigger level to limit the accidental rate and the desire to minimize the threshold to obtain the minimum detectable energy for gamma-ray showers—A lower trigger threshold lets through more low-energy events, but may drastically increase rate of accidental coincidences, eventually exceeding the maximum data-rate (limited by the data acquisition system dead-time). For a threshold of 34 mV and small-zenith-angle observations, the trigger rate is around 15-30 Hz (depending on atmospheric conditions and star light); however it may be as low as 6 Hz at large zenith angles.

2.2 The Imaging Technique

The Atmospheric Čerenkov Imaging technique provides a method for detecting extensive air showers and differentiating between those initiated by gamma rays and cosmic rays (e.g. Reynolds et al., 1993). The raw data recorded by the telescope

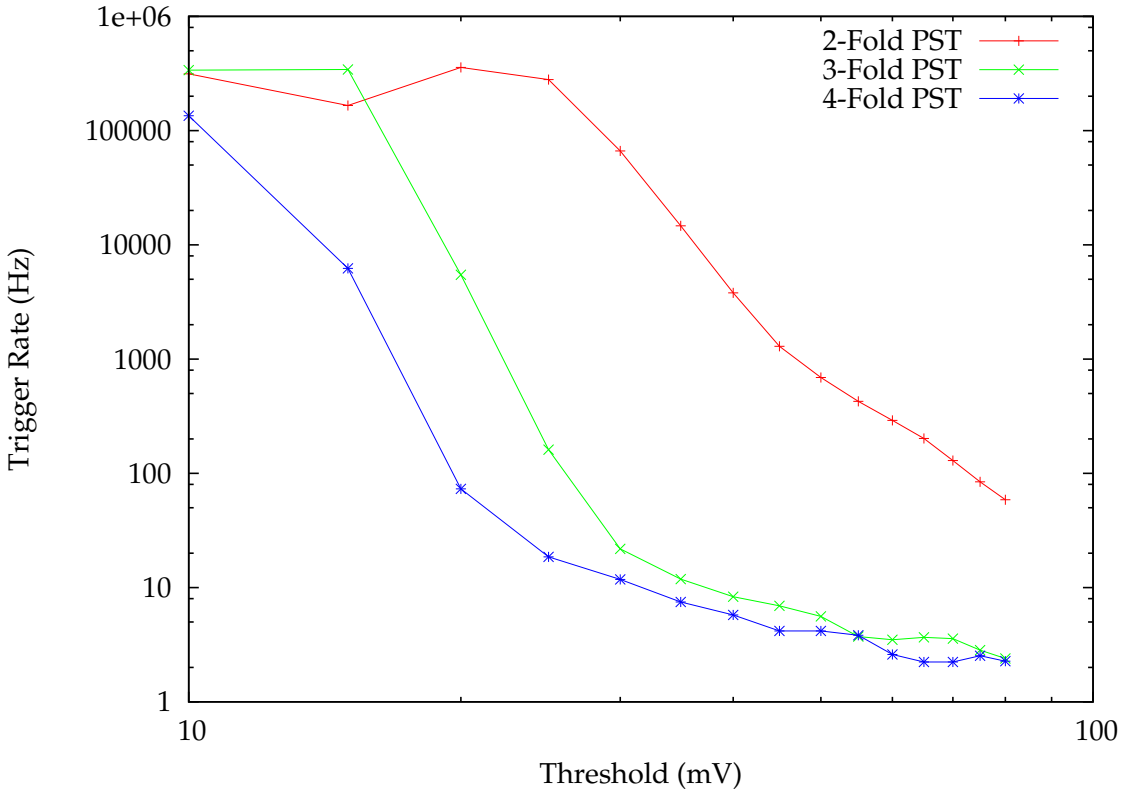

FIGURE 2.11: An example of a bias curve for the Whipple telescope for three different pattern trigger (PST) multiplicities. The trigger threshold is ideally set above (but close to) the electronic and night-sky-background noise to reduce the rate of accidental coincidences while accepting the maximum number of gamma-ray like events.

Season	**Threshold** (mV)	**Multiplicity**	**Trigger Window** (ns)
June 2004	34	3-fold	8
June 2003	30	3-fold	8
June 2002	34	3-fold	8
June 2001	32	3-fold	8
June 2000	36	3-fold	8
June 1996	62	2-fold	15
June 1995	62	2-fold	15

TABLE 2.3: Trigger thresholds levels for observing seasons with Galactic Center data.

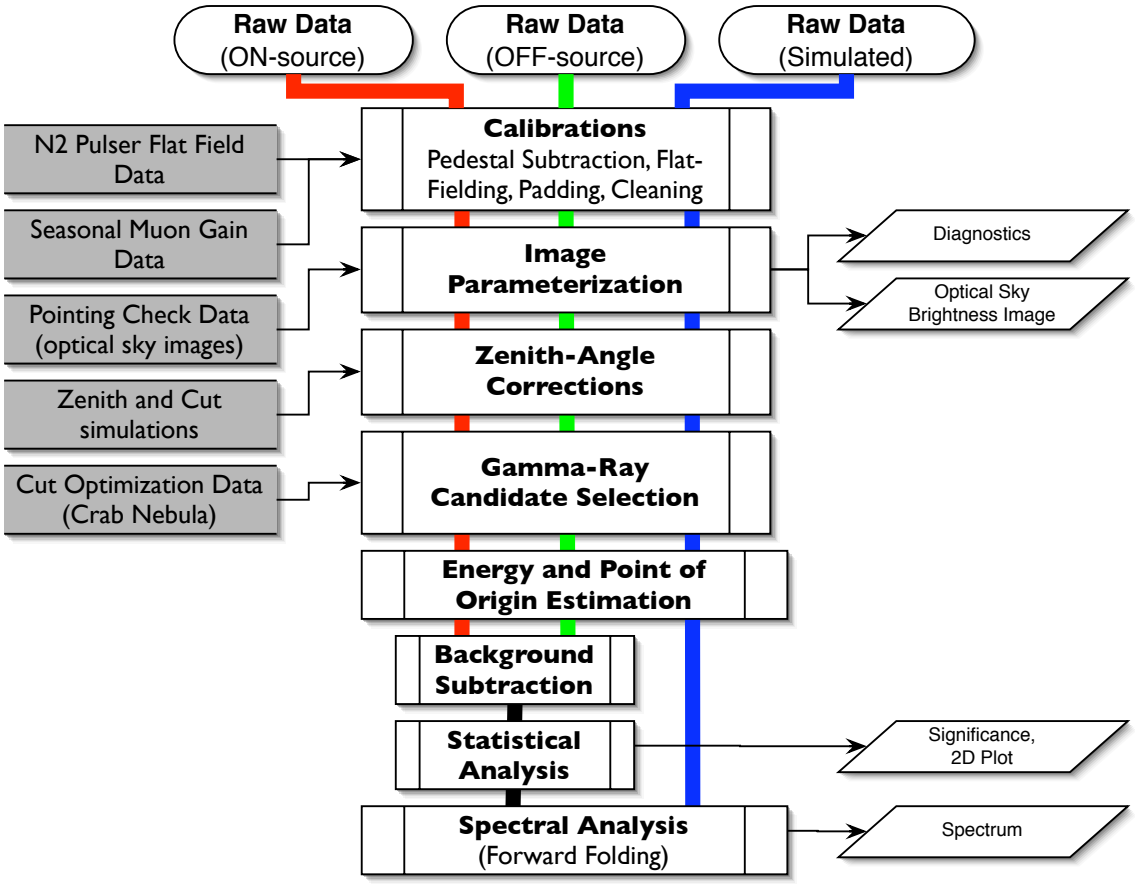

FIGURE 2.12: Summary of Analysis Data Flow

during an observation contains of a series of events that triggered the telescope, each consisting of a set of digitized integrated-charge signals for every pixel. These data are processed by off-line analysis in three steps: image-cleaning, parameterization, and cutting. In the first step, a series of calibrations are performed to calculate the noise-level and gain for each pixel (these are discussed in §2.2.2, 2.2.1). The results of these calibrations are used to perform pedestal subtraction and gain correction on each image as well as *padding* (§2.2.3) and *cleaning* (§2.2.4) procedures, which correct for night-sky background and remove noisy pixels, respectively. Next, a set of parameters based on the moments of the light distribution and signal values are calculated for each cleaned and corrected image (§2.2.5). In the final step of the analysis, selection criteria based on the parameterized shape of the image are applied to the parameterized images to determine which are gamma-ray candidates and which are likely background, recalling that the Čerenkov light distribution from hadronic showers is broader and less smooth due to the superposition of multiple electromagnetic sub-showers. (§2.3). Selected gamma-ray candidate events are used to determine the detection significance, two-dimensional image, and spectrum.

2.2.1 Pedestals

To measure the baseline noise level in each photo-multiplier tube, artificial triggers are injected at random intervals. The pedestal (P_i) and pedestal-variance (σ_i^2) for each pixel in the camera can be found by averaging the PMT signals and signal variance for all such pedestal events. This is performed for every run as the first

stage of the analysis.

The pedestal variances are used to determine which pixels in the camera should be excluded from analysis—tubes with too low a variance were most likely turned off in hardware (or not functioning properly), and tubes with too high a variance contained a star or other source of unwanted background light. The thresholds for excluding these pixels are set at 0.6 and 1.5 times the median pedestal value respectively.

Additionally, the pedestal variances are used for image cleaning (finding PMTs with signals above the noise), noise padding (see §2.2.3), and for generating sky-brightness maps used in pointing calibration (see §3.2).

2.2.2 Flat-fielding

At the start of each night of observing, the camera is uniformly illuminated by a nitrogen arc-lamp that produces pulses of light in the UV/blue frequency range. Data taken while the arc-lamp is active are used to flat-field the camera, correcting for any differences in gain between each photo-multiplier tube.

The flat-fielded gain correction, G_i, for the ith pixel of the camera is found as follows:

$$G_i = \frac{1}{N_{\text{events}}} \sum_{j=1}^{N_{\text{events}}} \frac{\langle S' \rangle_j}{(S'_{ij} - P_i)} \tag{2.7}$$

$$\langle S' \rangle_j \equiv \frac{1}{N_{\text{pix}}} \sum_{i=1}^{N_{\text{pix}}} (S'_{ij} - P_i) \tag{2.8}$$

where S'_{ij} is the signal measured in the ith phototube (in digital counts) for the jth event, P_i is the average pedestal for the ith pixel, and $\langle S \rangle_j$ is the average signal in all

the pixels of the jth nitrogen-pulser event. Normalizing to the average signal value takes into account variations in the amplitude of the nitrogen pulser, however the large variance in the amplitude requires additional care in rejecting pulses that either saturate some pixels or are too dim to be counted. To remove systematic problems and accidental triggers, only pixels with signals that fall within an acceptable range (i.e. not saturated or turned off) are counted in $N_{\rm pix}$, and events that have too small a fraction of pixels in the image with acceptable signals are skipped, and not included in $N_{\rm events}$.

2.2.3 Effects of Sky Brightness

Whipple telescope data are traditionally taken as pairs of 28-minute exposures, one ON-source and one OFF-source to subtract background. The OFF-source position is offset $30'$ in Right Ascension (RA) so that the telescope tracks exactly the same range of altitude and azimuth angles in the OFF run as the ON. For the Galactic Center analysis, the OFF run is taken first, while the ON run is taken 30 sidereal minutes later. The effects of night-sky-background light and changes in atmospheric conditions can be largely removed by analyzing both data sets in an identical manner, and using OFF-source data to subtract background. However, since the field observed in the OFF run corresponds to a different region of the sky, it will have still a different star field and may also have a different level of diffuse brightness than the ON run. Additional noise when added to the background Čerenkov images can cause a systematic bias in the number of background events passing data-selection cuts,

and therefore these brightness differences must be corrected before further analysis is done.

Before each image is parameterized, a Gaussian deviate is added to each pixel to bring overall noise in the ON and OFF data to the same level, a procedure called *padding*. The level of noise injected into each pixel is equal to the higher of the two pedestal dispersions in the ON and OFF source data. Failure to pad runs with noise can in some extreme cases even lead to false source detection or incorrect energy spectra when the final statistics are subtracted.

After the gains and pedestals have been calculated, the padded signal S_i in the ith pixel of an event is calculated by adding a random Gaussian deviate to the signal:

$$S_i = (S'_i - P_i) \cdot G_i + \underline{\mathcal{R}}\sigma_i \tag{2.9}$$

where $\underline{\mathcal{R}}$ is a stochastic sample of a unit Gaussian distribution, σ_i is the higher of the two pedestal dispersions for pixel i of the ON and OFF runs, G_i is the pixel gain factor, S'_i is the original (uncorrected) signal in digital counts, and P_i is the average pedestal.

2.2.4 Image Cleaning

The final step before parameterizing a shower image is to remove all pixels that most probably contain only noise and no signal from the shower. The image is "cleaned" using a two-threshold process: First, all pixels with a signal above a fixed *picture* threshold are marked to be included in the analysis. For the present analysis,

this threshold is 5 times the pedestal dispersion of a particular pixel ($S_i > 5.0\sigma_i$). Then, any pixels which are above a lower *boundary* threshold ($S_i > 2.5\sigma_{ped}$) and which have *at least one* neighboring *picture* pixel are also included. The choice of these thresholds depends on the camera configuration and is usually re-optimized for different cameras and different analysis procedures. The resulting thresholds are chosen to reject accidental fluctuations in background light, while maintaining the minimum threshold. Rejection of such out-lier hits is particularly important to reliably calculate the higher-order moments of the image. Any pixel not marked as *picture* or *boundary* is excluded in the subsequent analysis. Figure 2.15 shows a several shower images with the clean pixels marked with darker circles.

2.2.5 Shower Parameterization

The final step to characterizing a Čerenkov light image is to calculate a set of parameters describing the distribution of light. These parameters, referred to as *Hillas parameters* (after Michael Hillas, whose paper originally describes them), are then used to differentiate between gamma-ray and hadron showers. The Hillas parameters are based on the moments of the roughly elliptical Čerenkov light distribution, up to third order and are defined as follows:

LENGTH (λ): the RMS angular size of the major axis of the ellipse, related to the longitudinal development of the shower.

WIDTH (ω): the RMS angular size of the minor axis of the ellipse, related to the

lateral development of the shower.

SIZE (S): the total (integrated) signal in the shower image. This parameter gives an approximate measure of the primary energy of the gamma-ray, as described in section 2.5.

DISTANCE (d) the angular distance from the center of the camera to the centroid of the light distribution. This parameter gives a measure of the parallax angle to shower-max and is related to the impact parameter. Showers that fall too close to the center of the camera will be circular and thus have ambiguous LENGTH and WIDTH. Similarly, showers with too large a DISTANCE may be clipped by the edge of the camera, and are thus unusable.

ALPHA (α): the angle made between the major axis of the ellipse and the line between the camera center and centroid. This measures the degree to which the ellipse points toward the center of the camera. From simple geometry, showers that originate from an object in the center of the field of view should have an ALPHA value close to zero degrees.

MAX1, MAX2, MAX3: the signal values in the highest three pixels of the image.

LENGTH/SIZE: Though not a independent parameter, this fraction is useful for rejecting muon events. Because muon images have roughly constant amount of light per unit arc-length, the distribution of LENGTH/SIZE (the inverse of this characteristic) shows two distinct populations of events, the lower of which are

predominantly muons (see Figure 2.13)

Mathematical formulae for each of the Hillas parameters may be found in Appendix A, along with source code for parameterization in Appendix D.2.

2.3 Gamma-ray Selection Criteria

Single-telescope ground-based gamma-ray astronomy is predominantly background-dominated; even for the strongest sources, most of the events seen by an ACT are noise or cosmic rays. Therefore, the process of differentiating between gamma-ray showers and hadronic showers is extremely important to minimize background while controlling systematic biases. Selection criteria based on the Hillas parameterizations of each image recorded by the telescope is the primary method of extracting signal from background. Figure 2.15 gives an example of actual events recorded by the Whipple telescope, including candidate gamma-ray, cosmic-ray, and muon shower images. Notice that gamma-rays have a relatively compact, smooth shape, while protons are larger and more spread out. Single muons produce arc or ring-shaped showers, which are easily rejected, but are useful for calibration purposes (this is discussed in detail in Chapter 3.1). All gamma-hadron separation techniques work by defining a particular subset of the Hillas parameter space which contains predominantly gamma rays and cutting out the rest of the events. Cuts on these parameters are optimized to maximize the signal to background ratio, $S/\sqrt{B}$, keeping a good fraction of signal events (typically about 50%), while rejecting the majority of background.

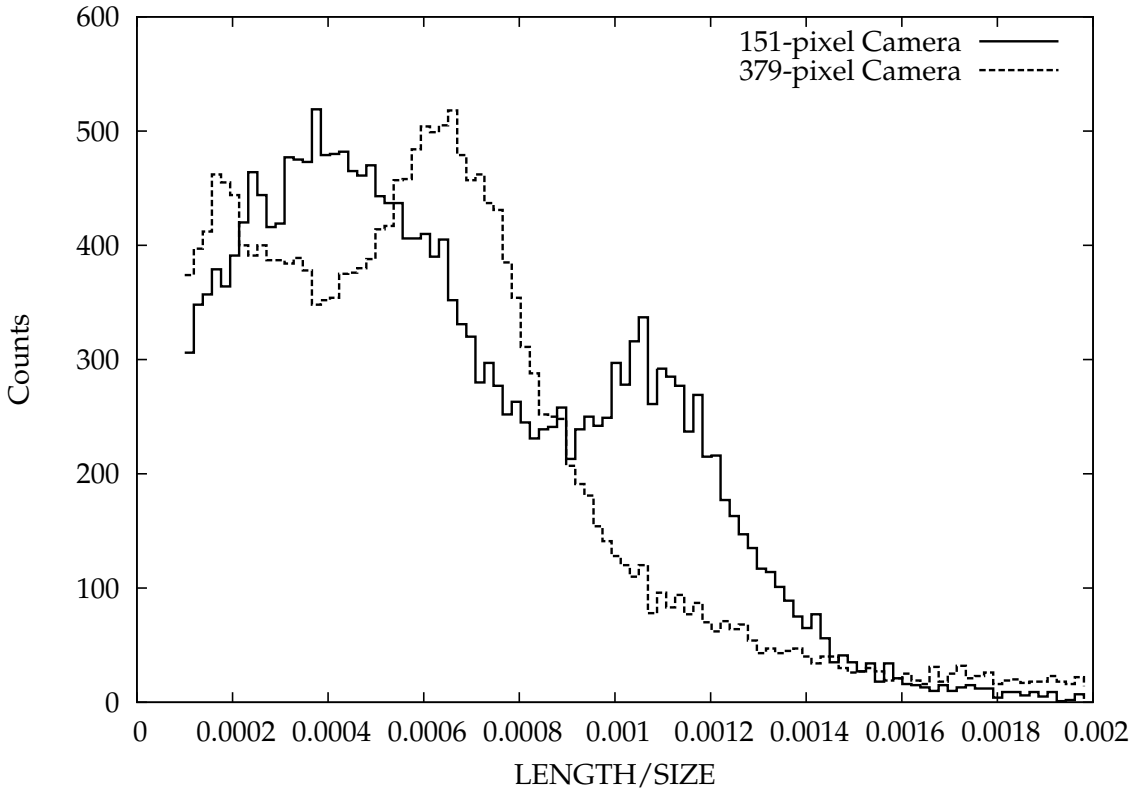

FIGURE 2.13: The LENGTH/SIZE (λ/S) distribution for Crab Nebula data taken with the older 151-pixel camera and the 379-pixel camera. Two peaks can be seen in both distributions: the right bump is produced predominantly by muons, while the left contains gamma rays and cosmic rays. The LENGTH/SIZE data selection cut is used to reduce the muon background. For EZCuts analysis, discussed later, this distribution is modified by a gain correction factor (See Figure 3.5) which allows one cut value to be used for multiple seasons.

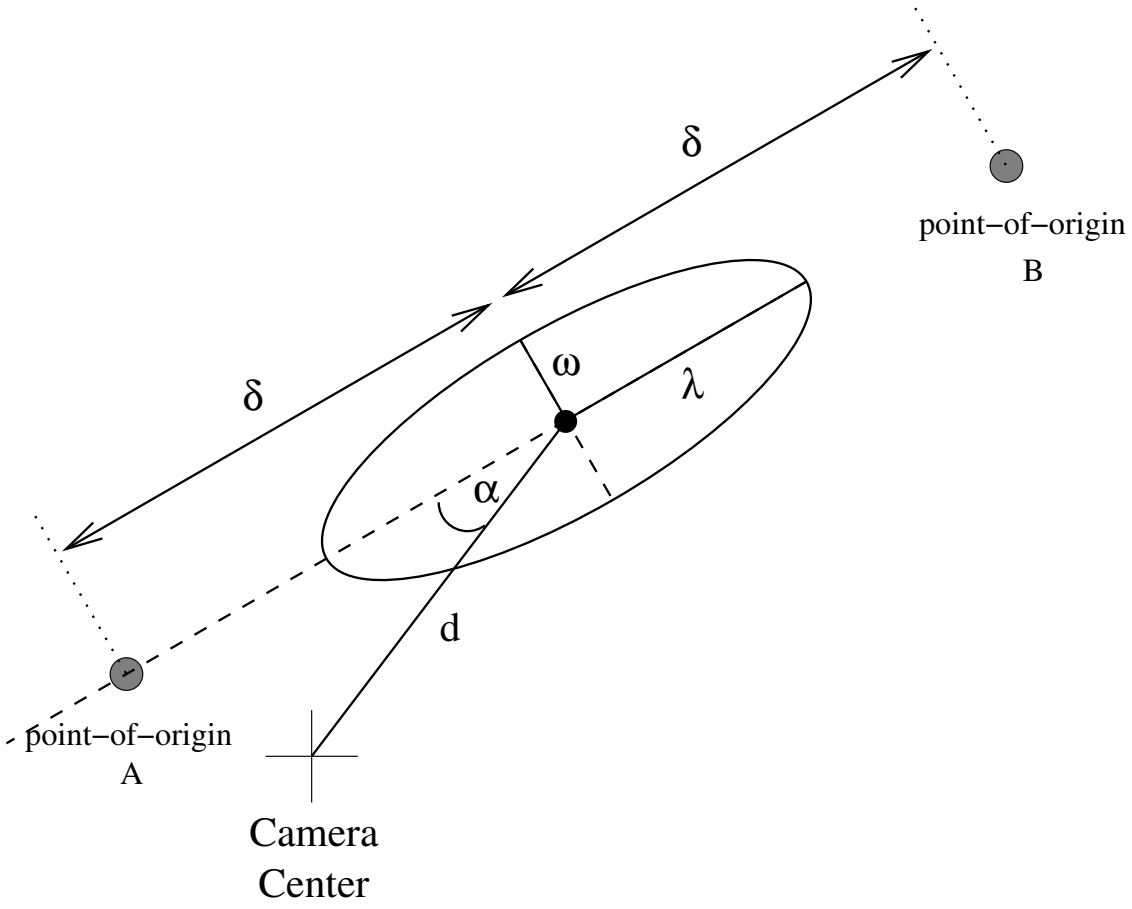

FIGURE 2.14: A graphic representation of the geometric Hillas parameters. The ellipse represents the extent of the shower image with overlaid LENGTH (λ), WIDTH (ω), DISTANCE (d), and ALPHA (α) parameters. The image centroid plotted as a black dot, along with the the two-dimensional points-of-origin and their corresponding displacement from the centroid (δ), which are discussed later in §2.4.

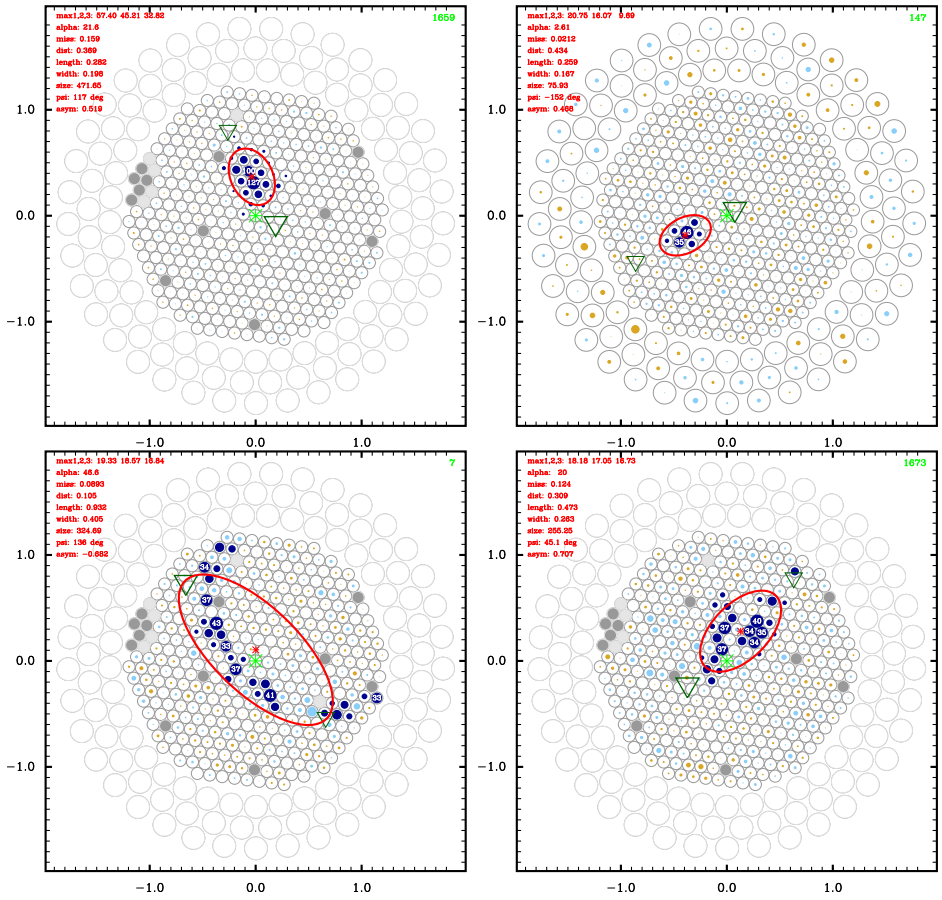

FIGURE 2.15: Examples of images produced in the camera by different types of showers. The upper-left image shows a likely gamma-ray shower from real Crab Nebula data, the upper-right shows a simulated gamma-ray shower, the lower-left shows a muon arc, and the lower-right shows a likely cosmic-ray shower taken from real data. Pixels that passed the cleaning thresholds are marked with darker circles. The overlaid ellipse on each image comes from the Hillas parameterization, and the possible points of origin (for gamma-rays) are plotted as triangles.

	SuperCuts 1995		SuperCuts 2000	
Parameter	Lower Cut	Upper Cut	Lower Cut	Upper Cut
ALPHA	0.0	10.0	0.0	15.0
WIDTH	0.073	0.15	0.05	0.12
LENGTH	0.16	0.30	0.13	0.25
DISTANCE	0.51	1.1	0.4	1.0
SIZE	400	∞	1.0	∞
LENGTH/SIZE	0.0	∞	0.0	0.0004
MAX1	100	∞	30	∞
MAX2	80	∞	30	∞
MAX3	0	∞	0	∞

TABLE 2.4: SuperCuts cut ranges for 1995 and 2000. These cuts used a *picture* cleaning threshold of $4.25\sigma_{ped}$, and a *boundary* cleaning threshold of $2.25\sigma_{ped}$

2.3.1 Traditional *SuperCuts*

The *SuperCuts* gamma-ray selection method is the standard method applied to Whipple telescope data. In this method, data are cut by comparing each Hillas parameter to simple, predetermined minimum and maximum values (Punch et al., 1992). The actual cut ranges are optimized for detection significance on real data from the Crab Nebula[3] at a fixed zenith angle, and are typically re-adjusted whenever the telescope changes configuration. The optimization is done on an iterative basis for each parameter. Table 2.4 shows the standard data cuts used in the 1995-2000, and 2000-2004 seasons.

SuperCuts work well for bright sources that are observed at low-zenith angle (less than 40°), but they have three major drawbacks: First, they do not scale well to

[3] The Crab Nebula, a supernova remnant, is used as a standard source for gamma-ray (and some X-Ray) observations because it is a very steady and bright source of high-energy emission. Often gamma-ray fluxes are quoted in units of *Crab*, which is useful for cross-calibration of different detectors.

larger zenith angles. To get around this, the cuts must be re-optimized for every range of zenith angles over which the source was observed. Secondly, *SuperCuts* change with each season and camera configuration, making it difficult to combine data from multiple seasons. Finally, the fixed cut ranges used in SuperCuts are not energy independent, making it difficult to perform spectral analysis.

Since the Galactic Center was observed only at very low elevation and over multiple seasons, the limitations of standard SuperCuts made them unsuitable. Instead, improvements had to be made to the gamma-ray selection process, prompting us to produce a new gamma-ray selection method which we call *EZCuts* (or *"extended zenith angle scaled cuts"*)[4] .

2.3.2 Improved *EZCuts*

The basic idea behind *EZCuts* is to remove the geometric and systematic effects of the atmosphere and telescope configuration from a parameterized shower image and look at the intrinsic properties of the shower—properties that are independent of zenith angle, energy, etc. For instance, instead of looking at the WIDTH of the shower, which gets smaller with increasing zenith angle, it would be nice to measure the Molière radius of the shower itself. Similarly, instead of cutting on the LENGTH of the shower, it would be better to cut on the extent of the longitudinal development in units of radiation length. While these intrinsic quantities are not readily availably,

[4] The "Extended" part of EZCuts is an homage *Extended SuperCuts*, which are another set of energy (but not zenith angle) independent scaling laws that have been used by other members of the Whipple Collaboration for spectral analysis (Hillas et al., 1998)

it is possible to re-scale WIDTH and LENGTH to obtain parameters which are more intrinsic. To this end, we use the WIDTH, LENGTH, DISTANCE, and MISS Hillas parameters along with the known zenith angle of the telescope, the pixel size of the camera and functional forms derived from simulations to define a new set of parameters: ZWIDTH, ZLENGTH, ZDISTANCE, and ZMISS. Additionally, we scale the SIZE, MAX1, MAX2, and MAX3 parameters by a factor which takes into account the changing photoelectron to digital-count (P.E./D.C) ratio of the telescopes between seasons (this procedure is described in §3.1). These new "Z" parameters are closer to the "intrinsic" parameters of the shower and allow the same data selection cuts to be applied to *any* dataset.

As one observes at increasing zenith angles, the distance to the core of the air-shower increases and thus the angular size of the shower and parallactic displacement of the image centroid are reduced. To first order, one would expect parameters such as WIDTH, LENGTH, DISTANCE, and MISS to scale by $\cos\vartheta$, where ϑ is the zenith angle of the telescope. The DISTANCE and MISS parameters simply scale by a factor of $\cos^{-1}\vartheta$, which makes sense from basic spherical geometry and are independent of energy. However, the LENGTH and WIDTH parameters are more complicated—air-shower simulations show that LENGTH and WIDTH also scale as the logarithm of the energy, which in turn must be derived from the total camera signal (S) and the zenith angle.

Since a final goal is to be able to look at gamma-ray spectra, EZCuts must also be energy independent. The energy of a shower is some function of the total signal (SIZE)

of the shower, the zenith angle, and its impact parameter (essentially, DISTANCE). Again, to first order we expect $E \propto S/\cos^2\vartheta$. Therefore, ZLENGTH and ZWIDTH need to be a function of ϑ, and $\log(SIZE)$.

$$\begin{aligned} ZWIDTH &= w'(\mathrm{WIDTH}, \vartheta, \log \mathrm{SIZE}) \\ ZLENGTH &= l'(\mathrm{LENGTH}, \vartheta, \log \mathrm{SIZE}) \end{aligned} \tag{2.10}$$

But what is the functional form of w' and l'? For that, one must look at distributions of Monte-Carlo simulated gamma ray events.

Monte Carlo Fits

To determine the functional form of the ZLENGTH and ZWIDTH scaling laws, a large number of gamma-ray events at fixed zenith angle ranges were simulated using a combined air shower, Čerenkov light, and detector simulation[5] . These simulations start with a full Monte-Carlo simulation of particle interactions forming the electromagnetic cascade, where the path of each secondary particle is traced, using a detailed model for atmosphere. From the particle tracks, Čerenkov photons are randomly generated and propagated to ground level. These simulated Čerenkov photon trajectories are then passed to an instrument simulation which ray-traces their path through the optics and electronics of the telescope, taking into account mirror reflectivities, camera PMT quantum efficiencies, and the response of the data acquisition electronics. The PMT quantum-efficiencies were re-measured for this analysis

[5] The *GrISU* simulation package from Grinell and Iowa State Universities was used which combines the KASKADE7 particle air-shower simulation with the `cerenkf` Čerenkov light simulation and `grisudet` instrument simulator.

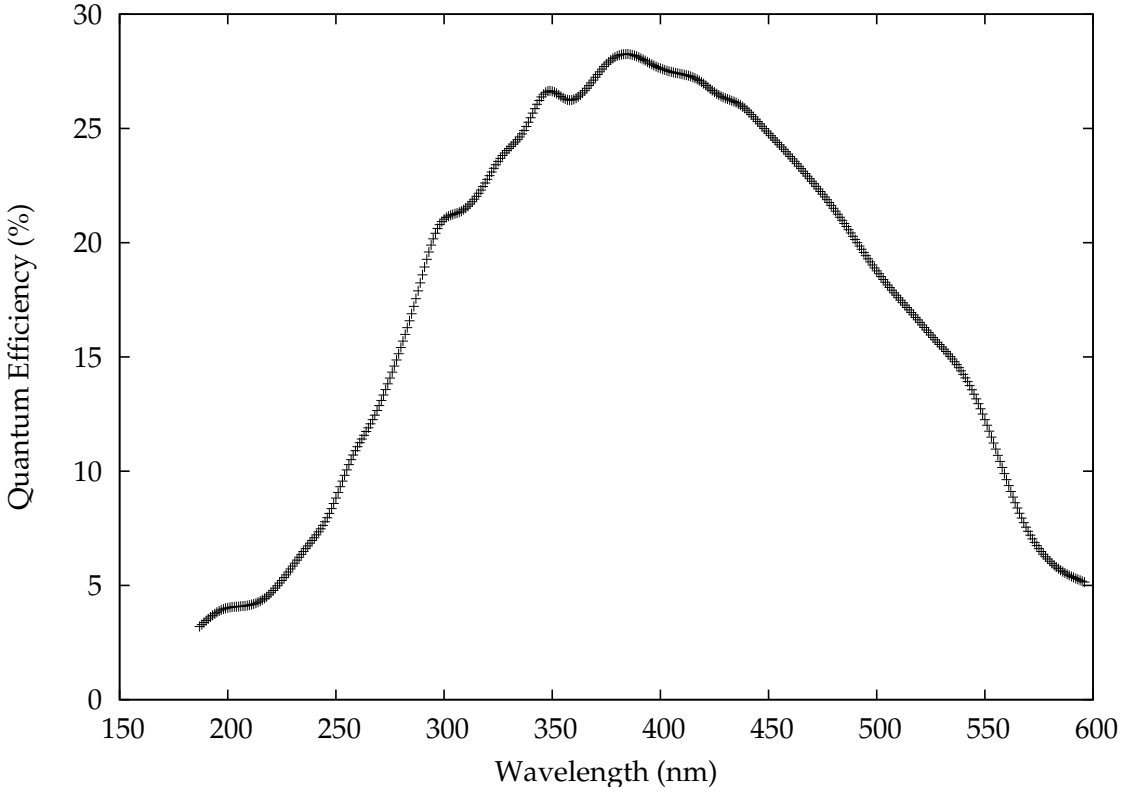

FIGURE 2.16: Measured quantum-efficiency curve for a Whipple camera phototube which was used to calibrate the simulations (Rebillot, 2003).

in-house (see Figure 2.16) and the simulation gains were re-calibrated. The data from these simulated events are analyzed with the same software as real events, providing an excellent tool for developing selection criteria.

To determine the WIDTH and LENGTH scaling, we start with a general functional form of:

$$w'(x) = \left\{ \left[(w^2 - \sigma_{\rm psf}^2 - \sigma_{\rm pix}^2)^{\frac{1}{2}} + B(x-C) + E(x-C)^2 + F(x-C)^3 \right]^2 \cdot \right. \\ \left. \cdot \mathcal{Z}(\cos\vartheta) + \sigma_{\rm psf}^2 + \sigma_{\rm pix}^2 \right\}^{\frac{1}{2}} \quad (2.11)$$

Where w is either the LENGTH or WIDTH value, x is $\ln SIZE$, ϑ is the zenith angle, $\sigma_{\rm psf}$ is the width of a Gaussian describing the point spread function of the telescope optics, $\sigma_{\rm pix}$ contains the effect of a finite pixel size and any other factor not dependent on energy or zenith angle, $\mathcal{Z}(\cos\vartheta)$ is a function describing the zenith angle scaling (defined later), and B, C, D, E, F are free parameters.

Due to time and data storage limitations, the fits to this function were done in two stages: first the parameters B, C, D, E, F (with $\mathcal{Z}(\cos\vartheta) = 1$) were fit to a distribution of simulated gamma rays at a fixed zenith angle of 60°—which takes care of most of the SIZE and DISTANCE scaling. Then, the resulting function was applied to simulations made at a different zenith angle (21°) and a functional form for $\mathcal{Z}(\cos\vartheta)$ was inserted account for the change. Figure 2.17 shows the results for the first stage fit, which was done to simulations generated at large (60°) zenith angle.

For the second stage fit, $\mathcal{Z}$ is defined as:

$$\mathcal{Z}(\cos\vartheta, \cos\vartheta_{\rm fixed}) \equiv \frac{\cos^{\beta}(\vartheta_{\rm fixed})}{cos^{\gamma}(\vartheta_{\rm fixed})} \cdot cos^{\gamma}(\vartheta) \tag{2.12}$$

where $\vartheta_{\rm fixed}$ is the fixed zenith angle from the first stage fit (60°), ϑ is the zenith angle variable, and γ and β are free parameters. The parameters B, C, D, E, F are held fixed at their previous values and γ, β are fit to simulates generated one or more zenith angles (in this case $\vartheta = 20°$).

Figure 2.18 shows the final functions for ZLENGTH and ZWIDTH applied to the second-stage data. Note that the only parameters fit to this data were β and γ. The fact that it was not necessary to change the fit parameters B,C,D,E,F for the smaller-

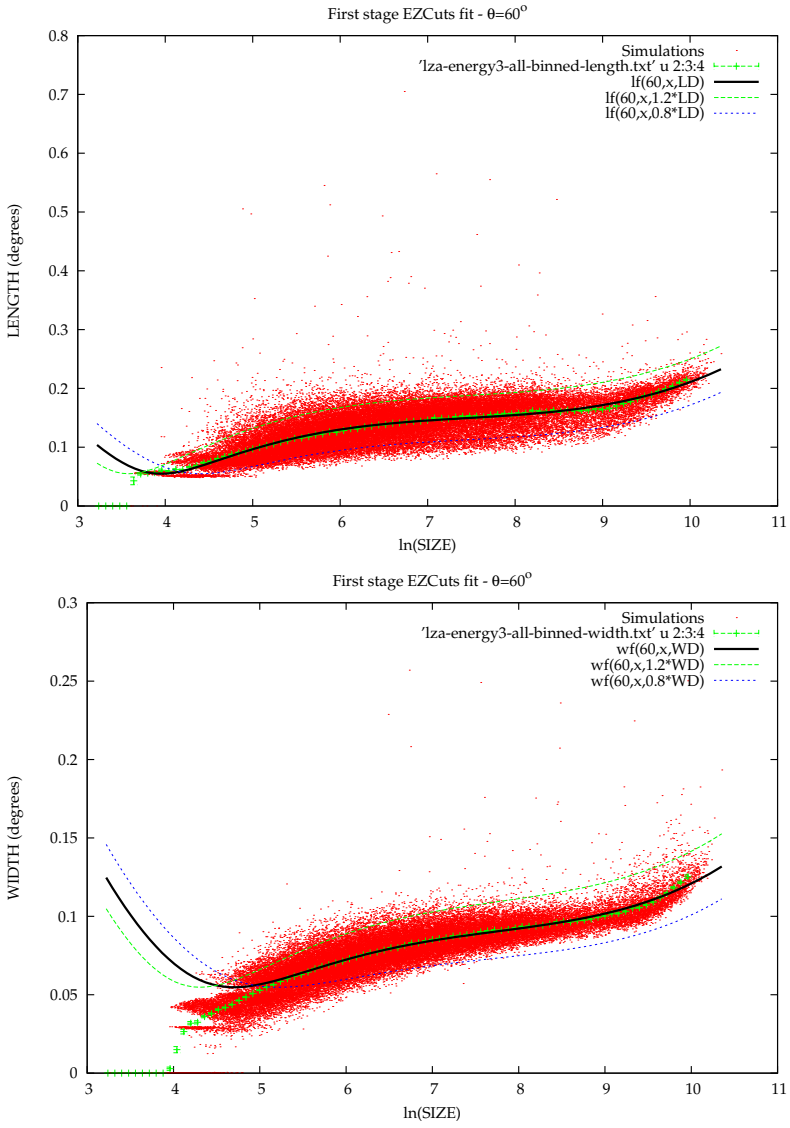

FIGURE 2.17: Fits of EZCuts ZLENGTH and ZWIDTH free parameters for stage 1 analysis at a fixed zenith angle of 60°. The dark line shows the final fit, while the dotted lines show an initial guess at a cut range (the actual range is later determined via optimization on real data).

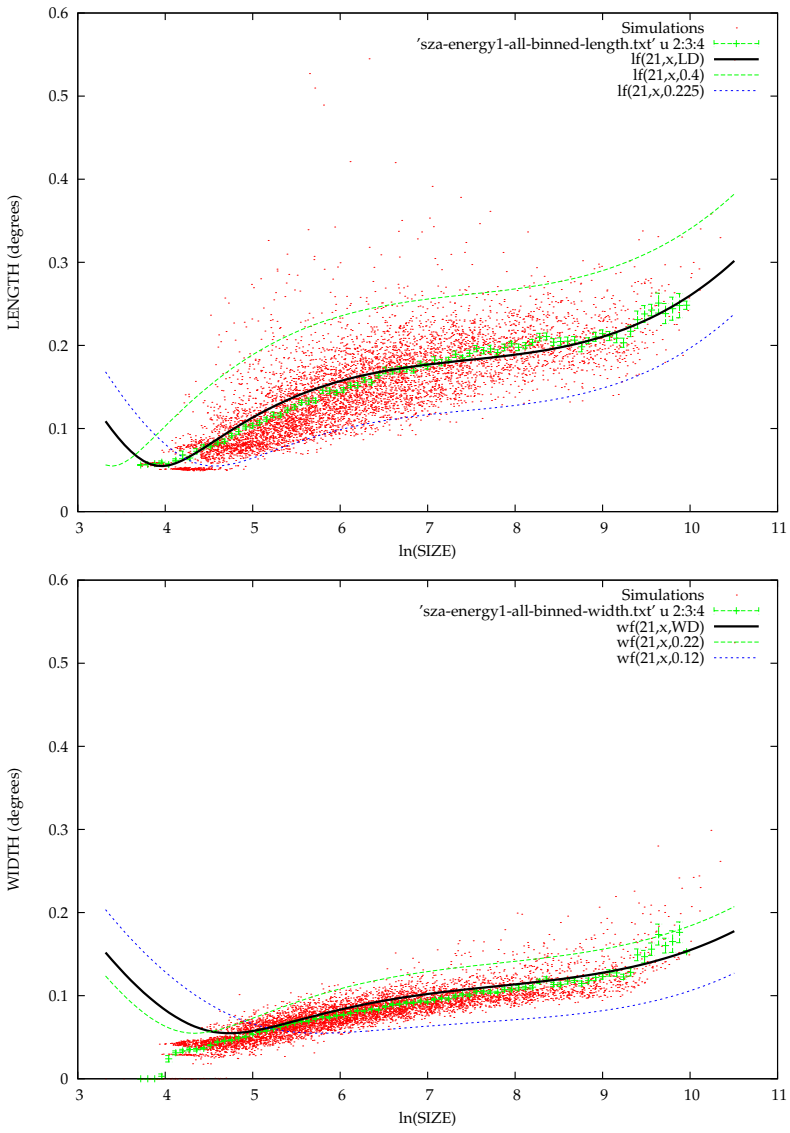

FIGURE 2.18: Fits of EZCuts ZLENGTH and ZWIDTH free parameters for stage 2 analysis at a fixed zenith angle of 21°. The dark line shows the final functional forms, while the dotted lines the cut range (determined via optimization on real data). Note that the functions scale well to this zenith angle even though most of the parameters were fit to data generated at 60°.

Parameter	ZWIDTH	ZLENGTH
A	0.003	0.003
B	0.047 ± 0.063	9.86 ± 2.08
C	9.8 ± 2.0	9.8 ± 2.0
D	0.18 ± 0.09	0.302 ± 0.001
E	0.015 ± 0.015	0.027 ± 0.001
F	0.0025 ± 0.0004	0.0037 ± 0.0002
β	1.5	1.2
γ	0.714 ± 0.02	0.949 ± 0.04

TABLE 2.5: Parameters for the ZLENGTH and ZWIDTH scaling functions (see Equation 2.11). A is derived from geometric considerations, B through F are from a least-squares fit to simulated data, and β, γ are fit (by hand and by least-squares, respectively) to a second set of data at differing zenith angle.

zenith-angle data set is a significant feature of our physically motivated scaling law (Equation 2.11). The deviation of the fit function at small values of $\log(SIZE)$ comes from the irreducible errors that occur when the shower images (defined by the pixels above the cleaning threshold) become closer in size to the dimension of a single pixel. The cuts on the Hillas parameters exclude this deviated region entirely. Source code for applying EZCuts "Z" corrections to standard Hillas parameters can be found in Appendix D.3.

Optimization

At this point, gamma rays can be selected by applying an upper and lower bound to ZLENGTH, ZWIDTH, and the other Hillas parameters. In the previous plots, these bounds are shown to bracket the data, however the best values are determined by applying a range of bounds to real Crab Nebula data (see Table 2.6) and optimizing

for the both the maximum statistical *significance* and gamma-ray count rate of the signal. The statistics of detection are outlined in Appendix B.

As an example, Figure 2.19 shows the optimization curve for the upper bound of ZWIDTH. The optimization was done on a large database of Crab Nebula runs with a wide range of zenith angles. The plot shows both the significance and number of accepted gamma-ray like events (excess) as a function of the cut bound. Usually, only the significance is used, however to minimize systematics for the spectral analysis and expand the sensitive energy range, it is also useful to look at the excess of gamma-ray like events and loosen the cuts to avoid systematic errors in the spectral reconstruction that might arise if the cuts are too restrictive (or if the energy scaling predicted by the simulations is not exactly the same as the real data). The upper cut gives a good balance of significance and excess at a value of 0.22.

Since optimization is a very computation intensive process, optimizing all parameters simultaneously was not feasible; instead, each parameter was optimized separately, and the process was iterated several times to produce refined optimizations. The final results are shows in Table 2.7.

2.4 2-D Imaging

In principle one can calculate most of the interesting astrophysical parameters (e.g. the flux and spectrum) of a gamma-ray source using only a one-dimensional analysis by placing an upper cut on the $ALPHA$ Hillas parameter. This method

ON	OFF	N2	UT Date	Elevation (°)
gt017039	gt017040	gt017025	2001-01-26	33
gt017160	gt017161	gt017151	2001-02-16	48
gt017265	gt017266	gt017256	2001-02-22	37
gt017522	gt017523	gt017521	2001-03-24	58
gt017524	gt017525	gt017521	2001-03-24	44
gt017568	gt017569	gt017565	2001-03-26	45
gt018386	gt018387	gt018371	2001-10-18	59
gt018697	gt018698	gt018677	2001-11-16	60
gt018833	gt018834	gt018826	2001-12-07	57
gt018965	gt018966	gt018958	2001-12-20	70
gt019106	gt019107	gt019105	2002-01-12	62
gt019159	gt019160	gt019143	2002-01-14	35
gt019298	gt019299	gt019296	2002-02-08	75
gt019304	gt019305	gt019296	2002-02-08	71
gt019689	gt019690	gt019688	2002-03-13	72
gt019899	gt019900	gt019901	2002-04-05	49
gt022717	gt022718	gt022708	2002-09-15	53
gt023072	gt023073	gt023069	2002-11-14	80
gt025761	gt025762	gt025743	2003-11-21	80

TABLE 2.6: Data runs taken of the Crab Nebula which were used for optimizing EZCuts.

Parameter	Lower Cut	Upper Cut
ALPHA	0.0	15.0
ZWIDTH	0.12	0.22
ZLENGTH	0.225	0.40
ZDISTANCE	0.28	2.5
SIZE	1	∞
LENGTH/SIZE	0	0.0008
MAX1	33	∞
MAX2	25	∞
MAX3	0	∞

TABLE 2.7: EZCuts cut ranges for all seasons. These cuts scale with zenith angle, energy, and use a *picture* cleaning threshold of $5.0\sigma_{ped}$, and a *boundary* cleaning threshold of $2.5\sigma_{ped}$

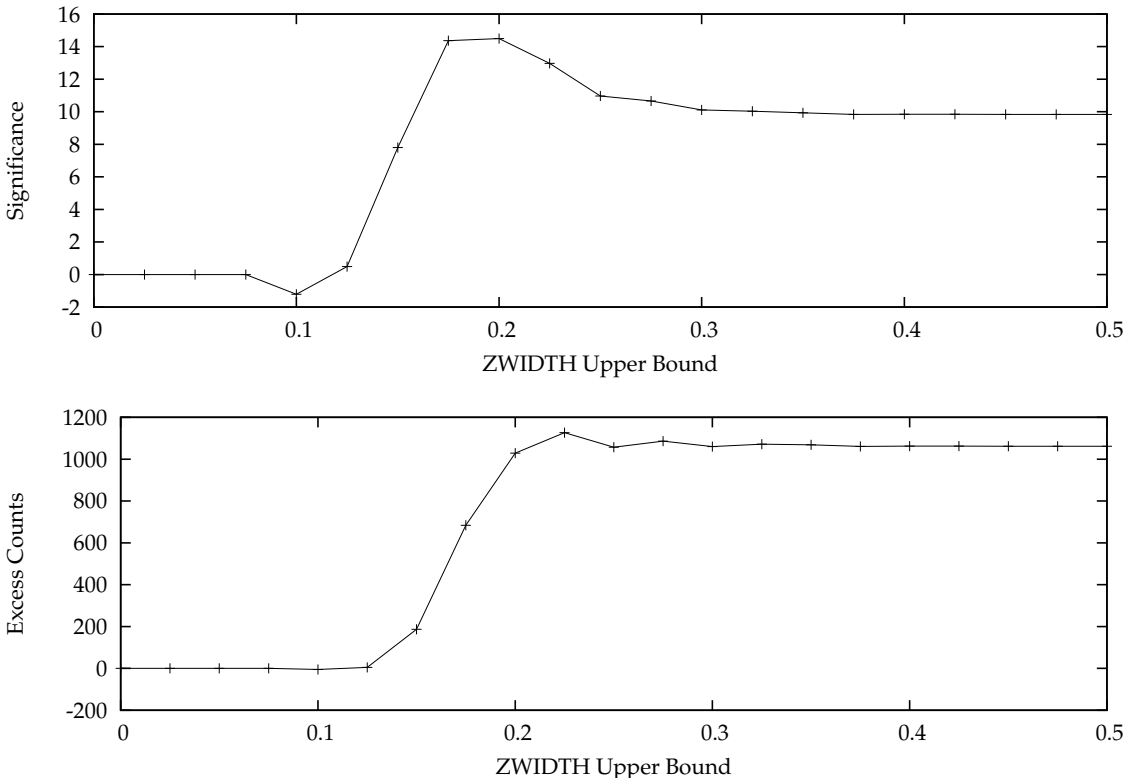

FIGURE 2.19: An example of an optimization curve for the ZLENGTH upper bound. Optimization was done on a large set of data taken of the Crab Nebula at various zenith angles. The top graph shows the statistical significance of the data set as a function of the cut value, while the bottom shows the number of gamma rays accepted.

consists of selecting only gamma-ray shower images that point back toward the source location to determine the detection significance and energy spectrum. This method does not provide any information about the position of the source in the field of view, or the angular distribution of gamma-ray emission—both of which are of potential importance for the Galactic Center. Additionally, it is known that the telescope's physical structure sags at low elevation, so even if the source location is well known, the actual position in the camera may not be at the center (this is discussed in more detail in Chapter 3.2). Finally, for an unknown source like the Galactic Center, there may be multiple sources or diffuse emission within the field of view that would confuse a 1-D analysis. For these reasons, it was necessary to generate a 2-D map of gamma ray emission across the field of view. Though two-dimensional gamma-ray analysis requires a more detailed understanding of the systematic errors in the analysis, it provides a useful tool for detecting unknown sources.

Two-dimensional analysis initially proceeds in much the same way as previously described—events are cleaned, parameterized, and selected based on their Hillas parameters. However, the ALPHA (or "orientation") cut used in the standard 1-D analysis is ignored—meaning that all gamma-ray like events are retained regardless of whether they came from a source at the center of the camera. The next step is to determine the point of origin each gamma ray candidate. The shower's point of origin can be determined by looking at the ellipticity of the image - which is related to the WIDTH and LENGTH parameters (or ZLENGTH and ZWIDTH, for EZCuts analysis)(Buckley et al., 1998). A gamma ray coming directly down the axis of the

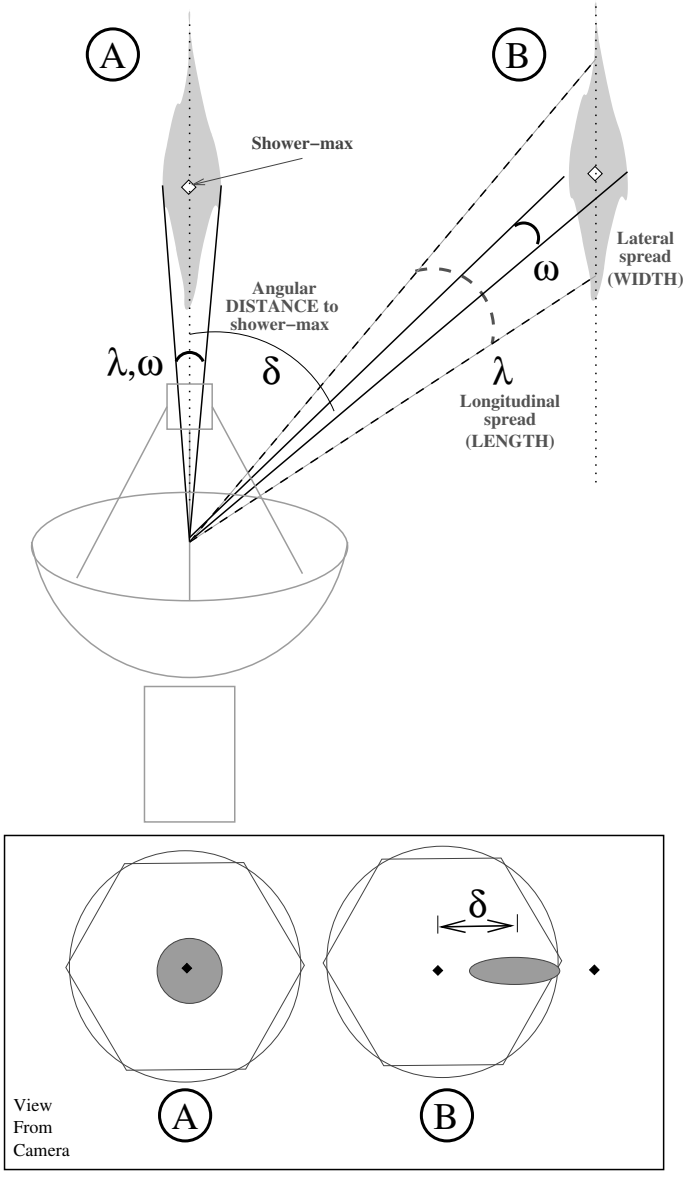

FIGURE 2.20: This figure shows the geometry involved in reconstructing the point-of-origin of a gamma-ray shower. In **A**, the shower is arriving directly down the axis of the telescope, so there is no displacement ($\delta = 0$) from the shower centroid, and the longitudinal and lateral extents of the shower appear equal ($\lambda = \omega$). In **B**, the shower has a finite impact parameter, producing an ellipsoidal shower image with two possible points-of-origin (marked as diamonds in the camera view), offset by a displacement $\delta > 0$ (see Equation 2.13). In both scenarios, the shower's point-of-origin is the same, at the center of the camera. In this case the displacement δ is equal to the DISTANCE Hillas parameter, which would not be the case for showers with points-of-origin offset from the center.

telescope's mirror would produce a circular image, while one arriving from an offset position creates an elongated image (see Figure 2.20, where ω is the WIDTH or ZWIDTH parameter, λ is LENGTH or ZLENGTH, ϵ is the elongation factor, and δ is the displacement from the image centroid to the point of origin). The displacement of the point of origin (δ) from the image centroid is related to the elongation by an energy-dependent elongation factor $\epsilon(\log S)$, where S is the SIZE parameter, and can be expressed by the following formula:

$$\delta = \epsilon(\log S)\left|1 - \frac{\omega}{\lambda}\right| \tag{2.13}$$

If the elliptical images were completely symmetric, there would be two degenerate points of origin for each image which lie on the major axis of the ellipse—one at the centroid position *plus* the displacement, and the other in the opposite direction. However, detailed simulations show that gamma-ray events have a consistent skew (third moment of the light distribution) resulting in a cometary shape with the head pointing toward the true point of origin. This skew (or *asymmetry*) of the image can be used to differentiate between these points of origin (see §A.4, Equation A.11) with mixed success. While one can see that gamma-ray images are usually skewed in the expected sense, the gain in signal-to-background obtained by cutting on asymmetry is marginal. This is due to the fact that significance, defined as $(N_{on} - N_{off})/\sqrt{N_{on} + N_{off}}$, benefits only if there is a much larger background rejection factor than the gamma-ray detection efficiency. The utility of this cut also depends on the camera: Cameras with limited fields of view truncate images resulting

in asymmetries that always point toward the edge. Since asymmetry is a higher-order moment of the distribution ($\sim \langle x^3 \rangle, \langle y^3 \rangle, \langle xy^2 \rangle$, etc), it is also the least robust. In periods where the light cone efficiency was low, holes in the images (when light falls in gaps) will also produce errors in the asymmetry.

The elongation factor, ϵ, was determined by fitting a line to simulated data, resulting in the following formula:

$$\epsilon(\log S) \equiv 1.0894 + 0.092611 \log S \tag{2.14}$$

where S is the gain-corrected SIZE parameter. In the methods first introduced by Buckley et al. (1998), ϵ is a constant (with an optimized value of 1.68). Using our simulation database, we were now able to take into account the detailed energy dependence of this parameter. Making ϵ energy dependent is shown (qualitatively) to improve the angular resolution and significance of 2-D detections.

To produce the final 2-D gamma-ray image, both points of origin are calculated for each shower which passes the gamma-ray selection cuts. If the asymmetry is high enough and the image falls within a range of $0^\circ < d < 0.8^\circ$ (not close to the edge of the camera), the incorrect point is discarded, otherwise both are accepted (the wrong point simply adds to the background noise). This upper bound on asymmetry is demonstrated in Figure 2.22. The points are accumulated into a two-dimensional radially-smoothed histogram (where all bins in the histogram within the fixed radius R of the point of origin are incremented). If, as occasionally may happen, both points fall in the same radial bin, one is excluded. This slightly cumbersome procedure

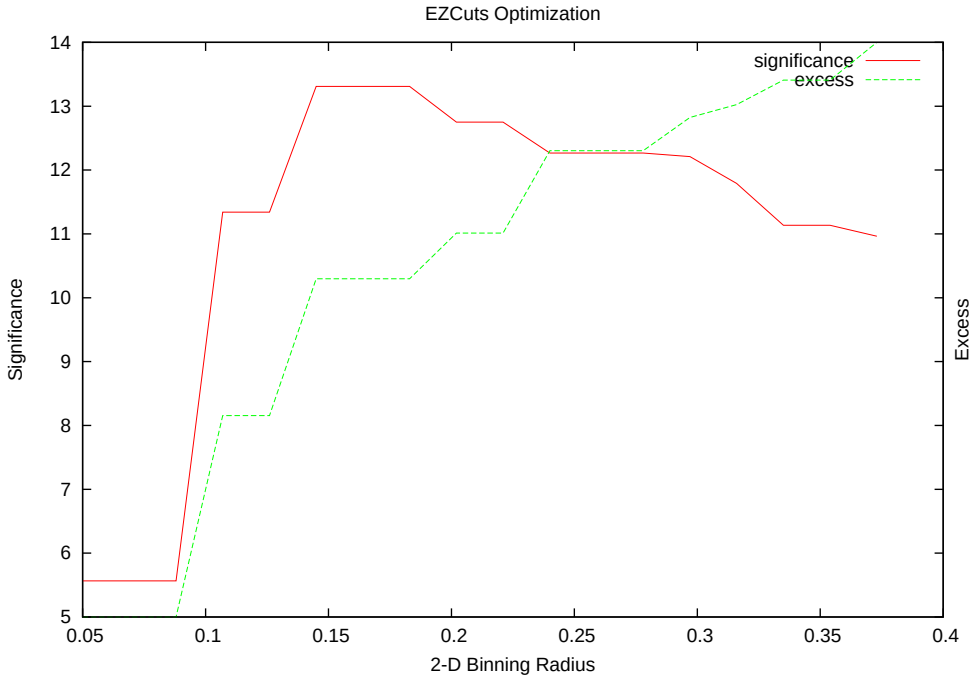

FIGURE 2.21: This figure shows the significance (solid line) and gamma ray excess (dashed line) measured in the center 2-D bin for data from the Crab Nebula optimization data set as a function of smoothing radius.

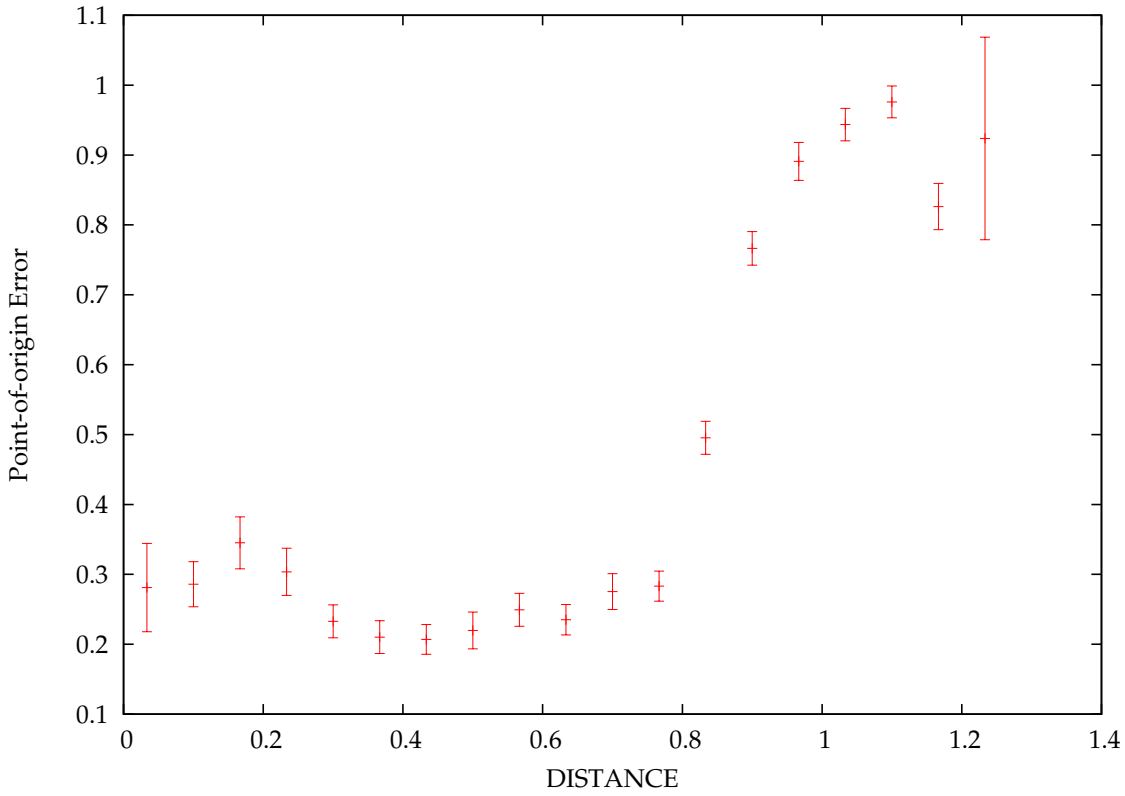

FIGURE 2.22: Plotted here is the distance between the asymmetry-selected point-of-origin and the true point-of-origin (the point-of-origin error) versus the DISTANCE parameter for the simulated data using the Whipple 379-pixel camera. From this, one can see that using asymmetry, the correct point-of-origin is chosen reasonably well up to a DISTANCE of 0.8°, after which image truncation effects at the edge of the camera cause asymmetry to fail.

ensures no double-counting of gamma-ray candidates. R is related to the point-spread function of the telescope and is determined by optimization on real Crab Nebula data. Figure 2.21 shows the significance of the center 2-D bin of the Crab Nebula optimization data set as a function of smoothing radius. ON and OFF data are treated in the same manner, and following the same procedure as the 1-D analysis, the significance and gamma ray excess counts are calculated at each 2-D bin. Figure 2.23 is an example of a two-dimensional gamma-ray image of the Crab Nebula at large zenith angle (Table 2.8) produced by this procedure. Note that this is not the optimization data set, but a separate set reserved to evaluate the quality of the cuts and to provide flux normalization for the Sgr A* data. Figure 2.24 shows another 2-D image of Crab Nebula data taken with the telescope offset 0.5° in declination (data is shown in Table 2.9, while a small-zenith-angle Crab image is shown in Figure 2.25.

The angular resolution of the 2-D analysis technique is determined by fitting an exponential function to a histogram of the square of the distance of each point-of-origin from the center of the observations position and extracting the full-width-half-max value. Table 2.10 shows the resolution and the gamma-ray acceptance rate for the Crab Nebula (which is to good approximation a point source) at large and small zenith angle, and at the 0.5° offset position.

2.4.1 2-D Orientation Cut

When the statistical significance is calculated in the traditional 1-D analysis, the final cut applied to each event is the orientation, or ALPHA cut, which selects only

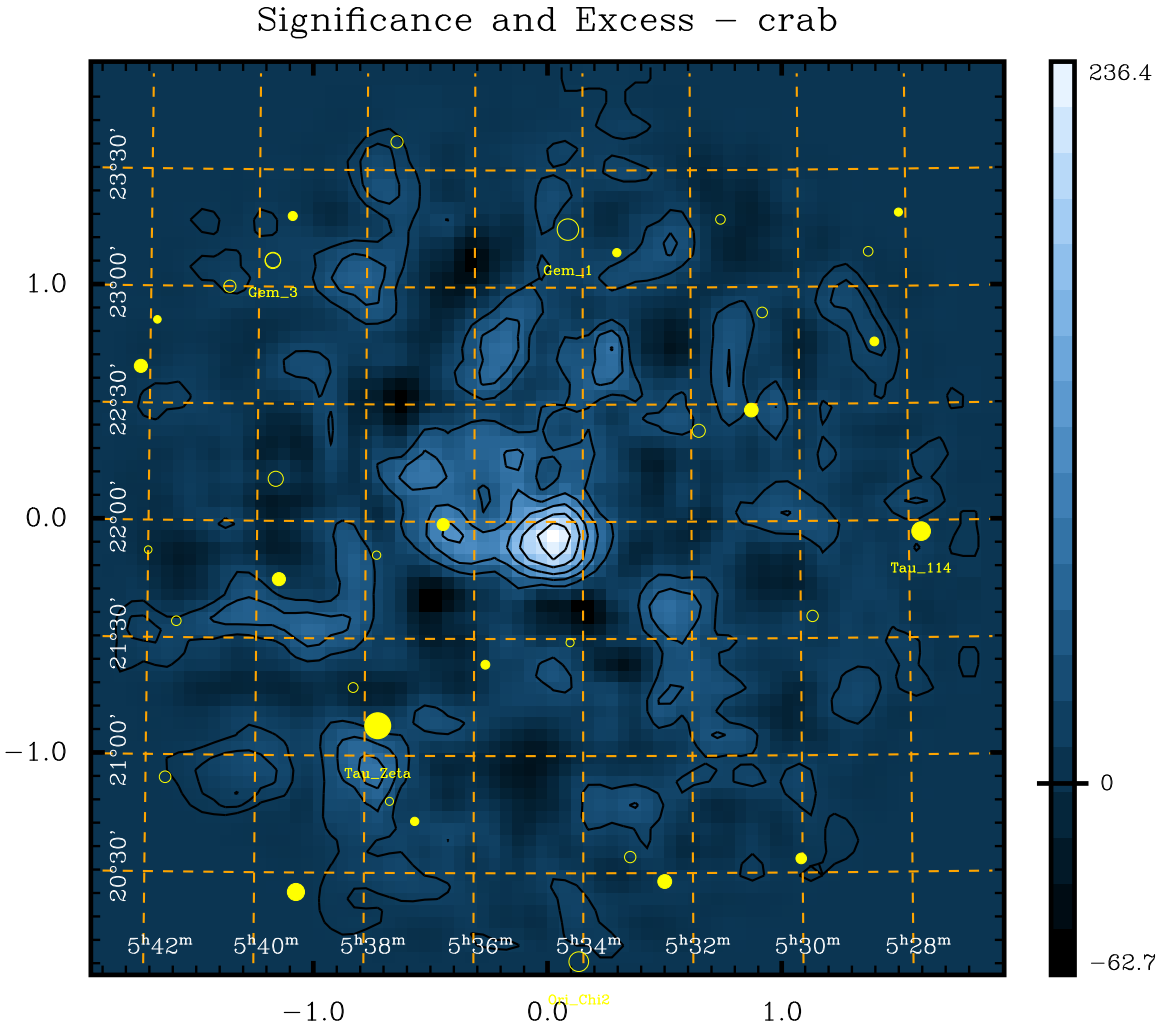

FIGURE 2.23: A 2-D image of the Crab Nebula at large zenith-angle (LZA) processed with EZCuts analysis. The image (with scale on the right) shows excess counts with overlaid significance contours (1 standard deviation per contour). The axes are labeled in degrees from the camera center position, and the dashed lines show the equatorial (RA/Dec) coordinate grid. Also plotted are the positions of nearby bright stars in the ON-source (filled circles) and OFF-source (open circles) fields. The significance at the center is 7.05σ, for 7.9 hours on-source observation time.

ON	OFF	N2	UT Date	Elevation (°)
gt014758	gt014759	gt014755	000309	27.52
gt014775	gt014776	gt014774	000310	31.52
gt014889	gt014890	gt014888	000401	31.75
gt016789	gt016796	gt016775	001230	29.41
gt016817	gt016818	gt016804	001231	26.89
gt017039	gt017040	gt017025	010126	30.26
gt017056	gt017057	gt017048	010130	28.17
gt017203	gt017204	gt017197	010219	30.48
gt017225	gt017226	gt017214	010220	25.03
gt017368	gt017369	gt017361	010315	27.54
gt017381	gt017382	gt017371	010316	27.00
gt017396	gt017397	gt017388	010317	31.74
gt017414	gt017415	gt017407	010318	25.24
gt017570	gt017571	gt017565	010326	26.7
gt017605	gt017606	gt017604	010328	32.37
gt019159	gt019160	gt019143	020114	32.38
gt022698	gt022699	gt022695	020914	31.26

TABLE 2.8: LZA Crab Nebula Dataset. These runs were used to calibrate the analysis for Galactic Center observations. See Figure 2.23 for the resulting analysis image.

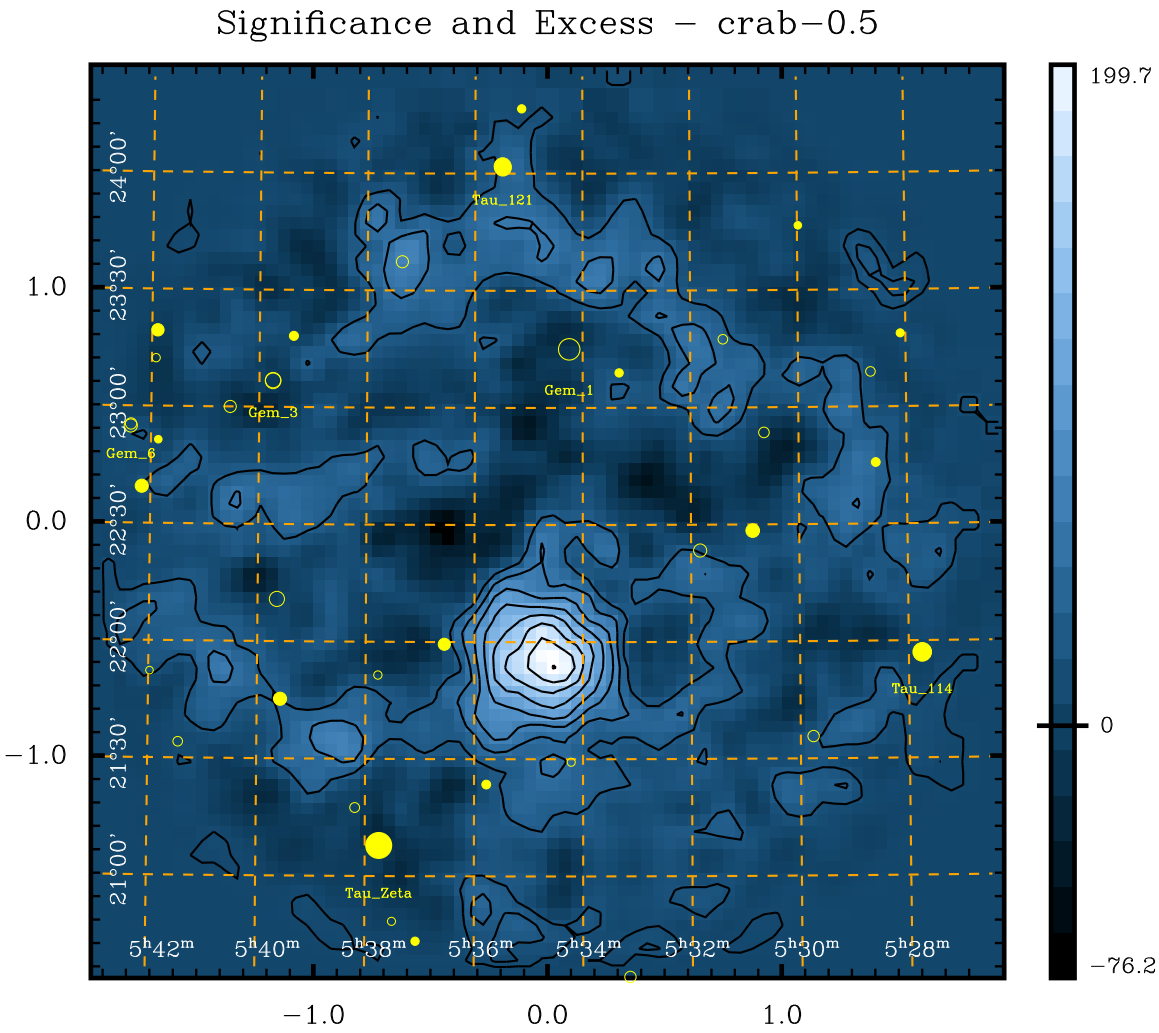

FIGURE 2.24: 2-D Image of the Crab Nebula taken with an offset of -0.5 degrees in declination and a total on-source exposure time if 2.8 hours (6 run pairs). The significance at the offset position is 7.2σ. These data were used to test the 2-D analysis, and show that a source can be located accurately when not positioned at the center of the camera. The image (with scale on the right) shows excess counts with overlaid significance contours (1 standard deviation per contour). The axes are labeled in degrees from the camera center position, and the dashed lines show the equatorial (RA/Dec) coordinate grid. Also plotted are the positions of nearby bright stars in the ON-source (filled circles) and OFF-source (open circles) fields.

events which point toward the center of the camera. However, in the interest of spectral analysis, which must be energy independent, we found that skipping the

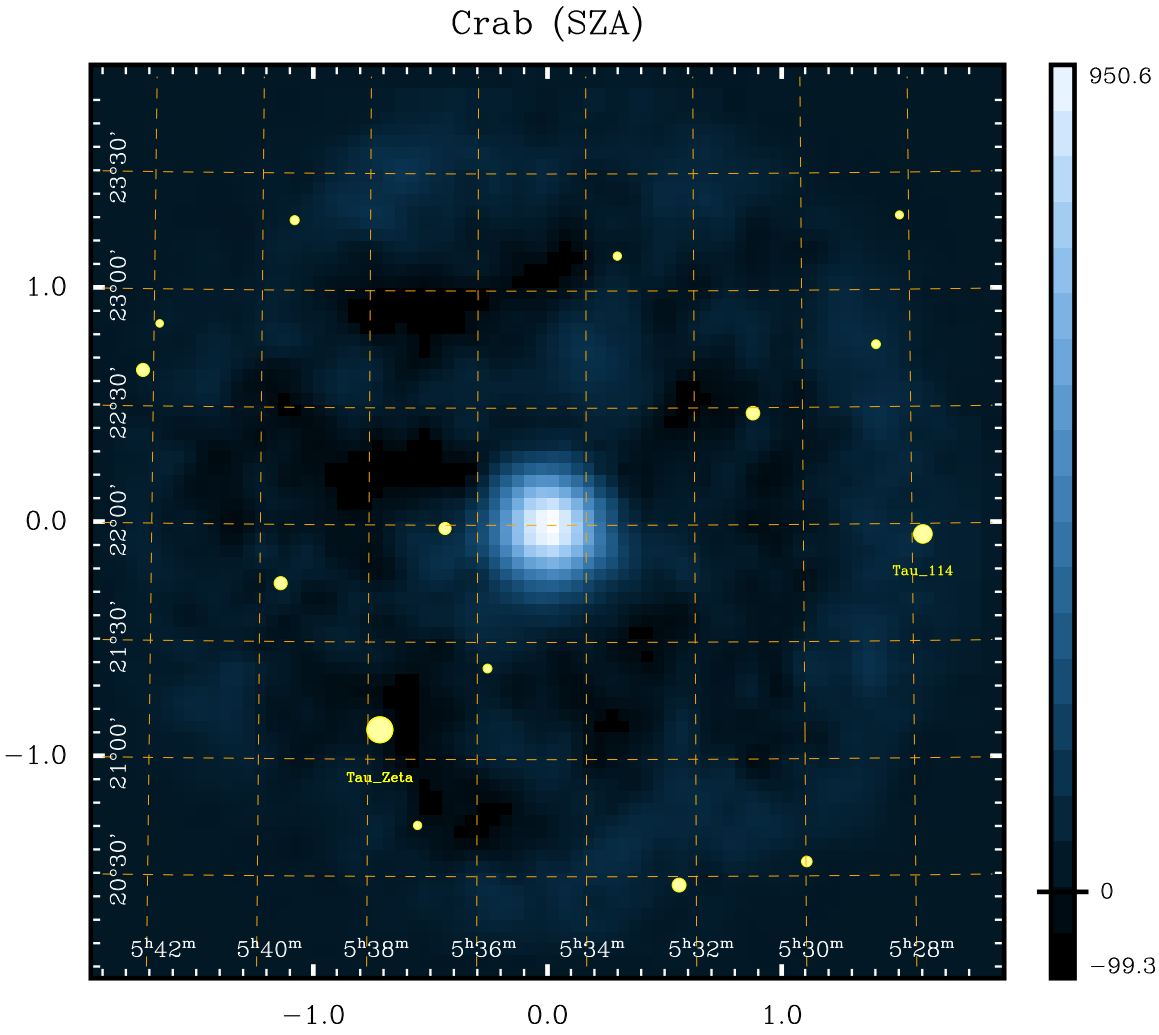

FIGURE 2.25: For comparison, this figure shows a 2-D image of the Crab Nebula at small zenith-angle (SZA) processed with EZCuts analysis. The significance is 17.2σ for 8 hours on-source observation time. The significance contours were omitted here to better show the image.

ON	OFF	N2	UT Date	Elevation (°)
gt019588	gt019589	gt019585	020305	64.48
gt019608	gt019609	gt019605	020309	58.86
gt019650	gt019651	gt019644	020311	54.86
gt019668	gt019669	gt019667	020312	70.68
gt019731	gt019732	gt019730	020315	65.09
gt019962	gt019963	gt019964	020409	43.39

TABLE 2.9: Crab Nebula Offset Dataset. These runs were used to test the 2-D analysis. See Figure 2.24 for the resulting 2-D image.

Data Set	**Resolution** FWHM (deg)	**Rate** (γ/min)
SZA	0.17 ± 0.009	1.80
LZA	0.18 ± 0.03	0.65
Offset	0.26 ± 0.03	1.11

TABLE 2.10: EZCuts angular resolution (FWHM) and gamma-ray acceptance rate for small zenith-angle (SZA), large zenith-angle (LZA), and 0.5° offset Crab Nebula observations.

ALPHA cut and instead selecting events whose 2-D points of origin fall within a radius R of the center of the camera (or a specified observation position) gave a substantially better energy resolution (and, of course, spatial resolution) at the expense of rejecting more events. This *radial cut* was adopted as the standard orientation cut for EZCuts, and is used throughout the spectral analysis results. Figure 2.26 shows the advantage of the radial cut over the ALPHA cut for energy estimation. We attribute this improvement to the fact that only relatively well-defined gamma-ray events with well-determined impact parameters pass the radial cut.

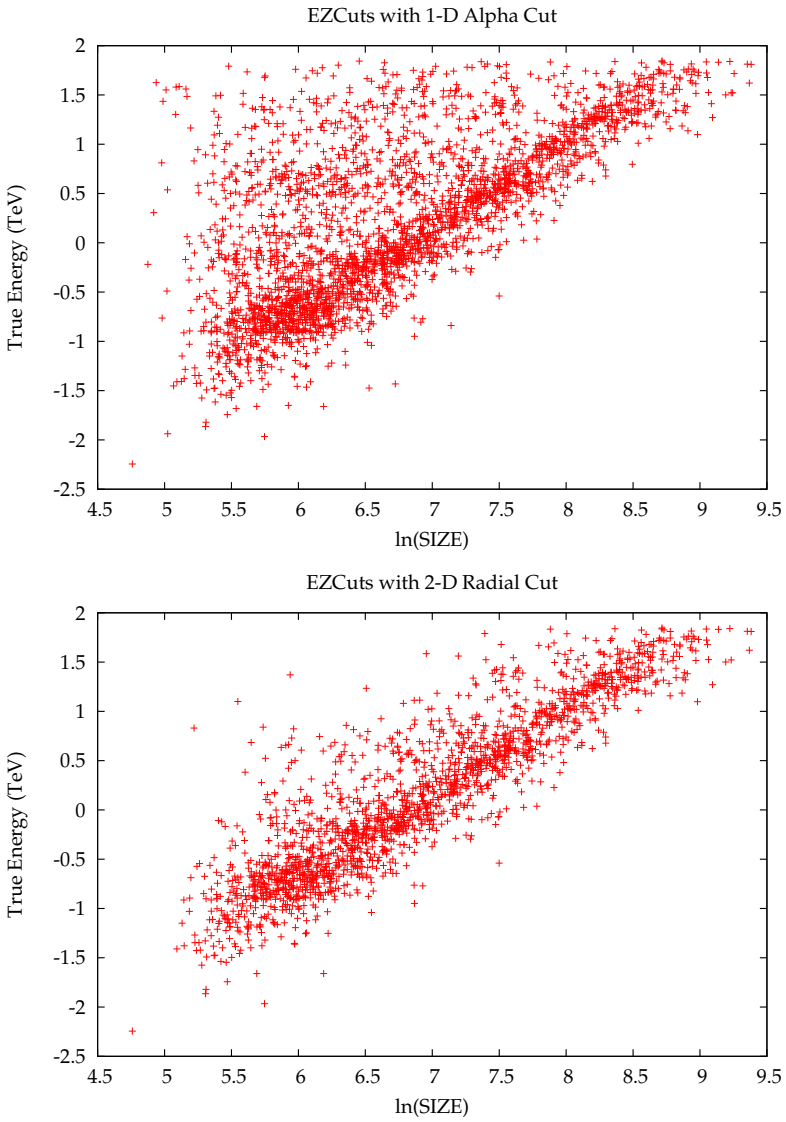

FIGURE 2.26: Shown here is a comparison of the effect of a 1-D ALPHA cut versus a 2-D radial cut on simulated data. Note that many simulated events which pass the ALPHA cut have ambiguous energies for a given SIZE value. The radial cut removes many of these events, resulting in better energy resolution. The function used for energy estimation is discussed in section

2.5 Spectral Reconstruction

Spectral reconstruction proceeds as follows: first, a data set of simulated gamma ray events is produced that span the entire sensitive energy range of the instrument. From this data set, an energy estimator function is derived, which connects the incident energy of the gamma ray to a function of the shower SIZE and DISTANCE. Then, a second series of simulated data sets are produced in fixed energy bins, each with a known spectral index. These Monte-Carlo events are later used for the spectral fitting; simulated model spectra are produced by weighting this data set to produce model spectra.

2.5.1 Energy Estimator Function

The first stage of spectral reconstruction of gamma-ray data is to define an energy estimator function. The energy of an incident gamma-ray is approximately related to the logarithm of the SIZE parameter, with higher energy showers producing a larger total signal. The actual relation of $\log(SIZE)$ to energy is also affected by the impact parameter of the shower (closely related to the DISTANCE parameter), as can be seen in Figure 2.20. Therefore, the energy estimator can be derived by fitting a function of DISTANCE and $\log(SIZE)$ to simulated data with known energies. For the present analysis, we derived different energy estimator functions for the small and large zenith-angle data.

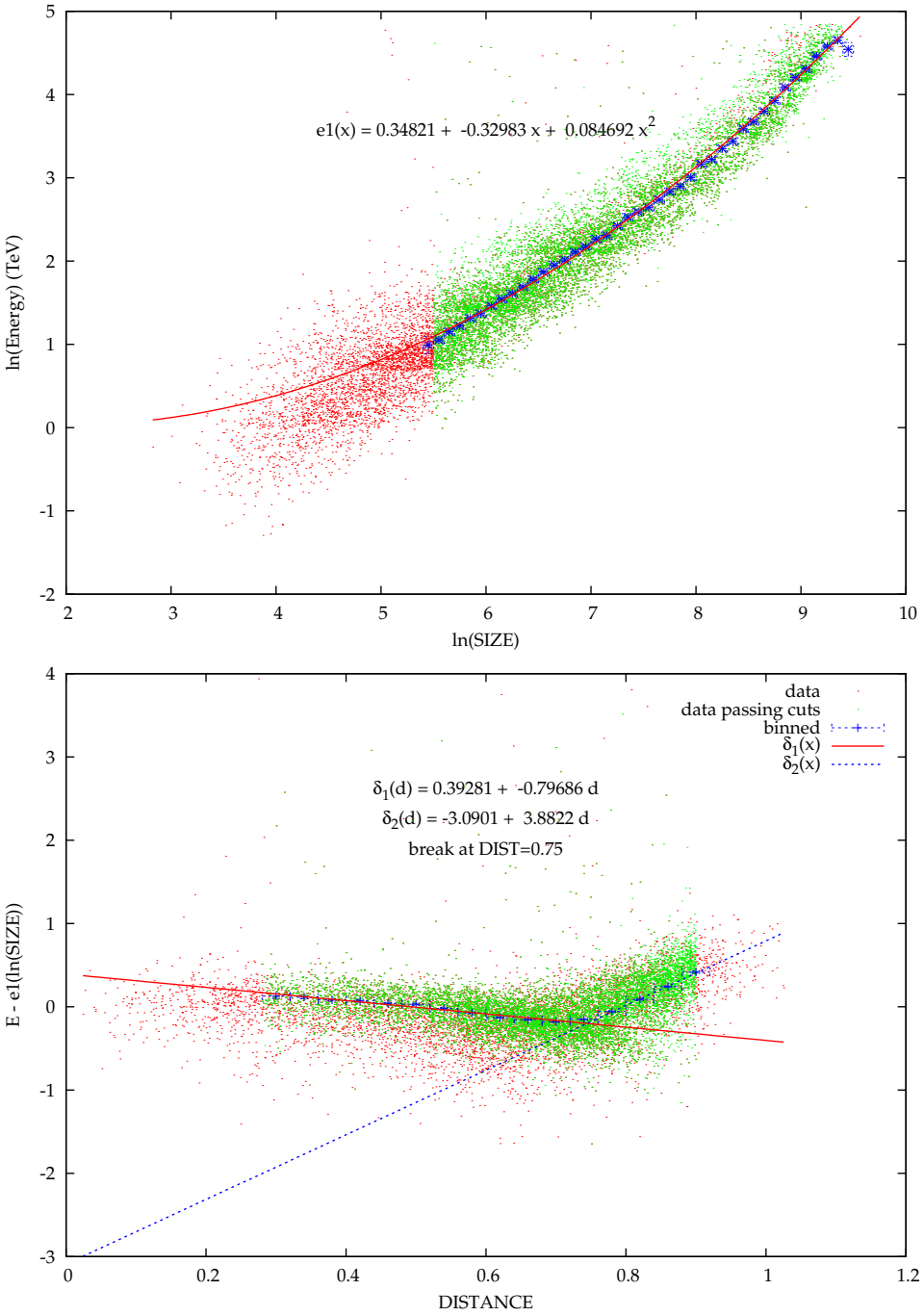

FIGURE 2.27: LZA Energy Estimator fits. The top graph shows the fit of the SIZE-dependent part of the energy estimator (e_1) while the bottom graph shows the DISTANCE-dependent part (e_2).

$\vartheta(^\circ)$	A	B	C	D_1	E_1	D_2	E_2
61	0.348	-0.329	0.084	0.392	-0.797	-3.09	3.88
21	-7.05	1.295	-0.034	0.057	-0.199	-1.964	2.443

TABLE 2.11: Energy estimator fit parameters from the LZA and SZA simulated data sets. These parameters apply to Equation 2.15.

Energy estimator functions were derived by fitting a formula of the form:

$$ENERGY(x, d) = e_1(x) + e_2(d) \tag{2.15}$$

with

$$e_1(x) \equiv A + Bx + Cx^2 \tag{2.16}$$

$$e_2(d) \equiv \begin{cases} D_1 + E_1 d, & \text{if d} \leq d_0 \\ D_2 + E_2 d, & \text{if d} > d_0 \end{cases} \tag{2.17}$$

to a large set of simulated gamma-ray events, where $x = \log S$ and d is the $DISTANCE$ parameter, and d_0 is the break point in the energy estimator function (see Figure 2.27b). The fits are done in two parts: first the polynomial e_1 function is fit to the distribution of $\log(E)$ versus $\log(SIZE)$, and then the piecewise linear function e_2 is fit to the the residual versus DISTANCE distribution. For this analysis, two simulation data sets were produced at 21° (SZA) and 61° (LZA) zenith angle, and in principle this must be done at each zenith angle where there are data. EZCuts were applied to both sets (using a radial 2-D cut instead of the ALPHA cut), and two energy estimator functions were derived. Figure 2.27 shows the fits to the large-zenith-angle data, and the resulting fit parameters are shown in Table 2.11.

2.5.2 Forward-Folding technique

The *forward folding* method is used to derive a spectrum from the data by comparing energy estimator distributions from real data to Monte Carlo simulations. This comparison of the measured distribution avoids having to deconvolve (unfold) the instrument response functions.

Monte-Carlo events are generated with a known power-law spectral index in a set of energy bins that span the sensitivity of the telescope. The Monte-Carlo data sets used for the spectral results in §4.4 are shown in Table 2.12. For this analysis, two Monte Carlo data sets were generated: one at 61° zenith and the other at 21°, to correspond with the SZA and LZA energy estimator functions derived in §2.5.1. In principle, an energy estimator and Monte Carlo database must be generated for every zenith angle range over which observations were made. Note that while our approximate scaling laws give roughly zenith-angle independent cut-efficiencies, we ultimately rely on simulations at definite zenith angles to accurately calibrate the procedure.

The differential photon flux ($\Phi(E)$) is assumed to be a power-law of the form:

$$\Phi(E) = N_0 E^{\gamma_0} \tag{2.18}$$

where N_0 is the normalization factor (in units of $\mathrm{m}^{-2}\mathrm{s}^{-1}\mathrm{TeV}^{-1}$), and E is the energy in TeV. To determine the spectrum, first a histogram of estimated energy for the real data is generated ($E_j^{(est)}$). The number bins in this estimated energy distribution does not need to correspond to the Monte Carlo database bins, and are selected to

	LZA Data Set ($\vartheta = 61°$)			SZA Data Set ($\vartheta = 21°$)		
i	$E_{\rm min}$ (TeV)	$E_{\rm max}$ (TeV)	n	$E_{\rm min}$ (TeV)	$E_{\rm max}$ (TeV)	n
0	0.25	0.50	20000	0.05	0.10	20000
1	0.50	1.0	14000	0.10	0.20	14000
2	1.0	2.0	10000	0.20	0.40	10000
3	2.0	4.0	8000	0.40	0.80	8000
4	4.0	8.0	6000	0.80	1.60	5000
5	8.0	16.0	5000	1.60	3.20	4000
6	16.0	32.0	3000	3.20	6.40	2500
7	32.0	64.0	3000	6.40	12.8	2000
8	64.0	128.0	2500	12.8	25.6	2000

TABLE 2.12: Monte Carlo Datasets used in the forward folding technique for spectral analysis. Two data sets (for large and small zenith angle) were generated to correspond to the two energy-estimator functions derived in §2.5.1. Each energy bin was simulated with a fixed differential spectral index of -1.5 and maximum impact parameter of 450 m.

roughly balance the statistics in each bin for a typical power-law spectrum. A grid-search is then made over possible values of N_0 and γ_0. For each trial, each event in the simulation database is weighted (by a fractional factor W) to correspond to the new power-law flux. The fractional weighting factor is used to fill a trial histogram of estimated energy with the same bins as the real-data energy-estimate histogram. The fractional weighting factor (W) is defined as:

$$W(E, N_0, \gamma_0) = \frac{N_0 E^{\gamma_0} \tau}{N_0' E^{\gamma_s} (\pi b_{\rm max}^2)^{-1}}$$
$$N_0' \equiv -(\gamma_s + 1) n_i \left[(E_{{\rm min},i})^{\gamma_s+1} - (E_{{\rm max},i})^{\gamma_s+1} \right]^{-1} \quad (2.19)$$

where N_0 is the trial value of the normalization factor, N_0' is the integral normalization, γ_0 is the spectral index trial value, n_i is the number of simulations in database bin i (which spans $E_{{\rm min},i} - E_{{\rm max},i}$ and contains E), γ_s is the spectral index used in building the simulation database, $b_{\rm max}$ is the maximum impact parameter used in

the simulation, and τ is the total integration time of the observation. By minimizing the χ^2-difference between the real and trial Monte-Carlo estimated-energy histograms over the search grid, we find the best-fit values for γ_0 and N_0. The final spectrum is generated by weighting the power-law model function by the ratio of the real and Monte-Carlo excesses in each bin using the following equation:

$$\Phi(E_i) = \left(\frac{n_i^{(\mathrm{on})} - \alpha n_i^{(\mathrm{off})}}{n_i^{(\mathrm{Monte-Carlo})}} \right) \cdot N_0 E_i^{\gamma_0} \tag{2.20}$$

where $n_i^{(\mathrm{on})}$, $n_i^{(\mathrm{off})}$, and $n_i^{(\mathrm{Monte-Carlo})}$ are the number of events in spectral bin i for the ON-source, OFF-source, and simulated data respectively, α is the ratio of the ON-source to OFF-source integration time, and E_i is the center of spectral bin i. The confidence intervals on N_0 and γ_0 are determined by varying the parameters independently until χ^2 changes by 1.0.

The standard Whipple spectral analysis method (Mohanty et al., 1998) assumes a power-law spectrum with log-normal errors and relies on a deconvolution of the energy resolution function. In general, deconvolutions are unstable when noise is present in the data and can lead to correlated errors. The forward-folding method of spectral reconstruction has some advantaged over this standard method in that it does not require a deconvolution or any assumptions about the shape of the energy resolution function. Since it amounts to an explicit model comparison, it is simple to fit other functional forms for the spectrum, such as a power-law with a cutoff, by changing the denominator of the weighting factor.

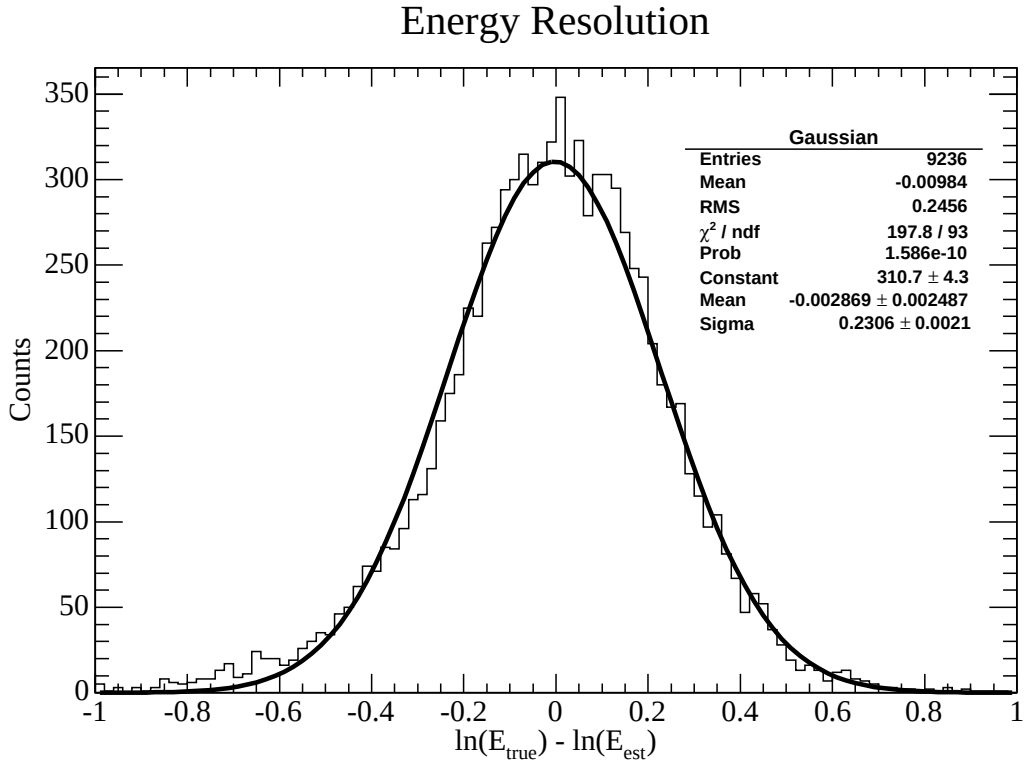

FIGURE 2.28: Energy Resolution for the LZA energy estimator function generated from simulated data. The resolution is related to the width of the Gaussian.

2.5.3 Energy Resolution

The energy resolution, σ_E/E, can be determined by looking at the distribution of $(\log E_{true} - \log E_{estimated})$ for simulated data. The full-width-half-max of this log-normal distribution, Γ is related to the resolution by:

$$\frac{\sigma_E}{E} = \left[e^{\Gamma/2.354} - 1\right] = \left[e^{\sigma} - 1\right]. \tag{2.21}$$

Figure 2.28 shows this distribution for the energy estimator used in this analysis, yielding an energy resolution of 26%.

Chapter 3

Instrument Calibration

Additional calibrations were needed in order to analyze the data from the Galactic Center and reduce systematic errors. First, the data from the Galactic Center span a wide range of observing seasons during which the Whipple Telescope camera was upgraded twice; combining such observations required a careful understanding of the instrumental characteristics, in particular the changes in gain between seasons. Second, due to flexure of the telescope at large zenith-angles, the exact deviation of the telescope from its center position needed to be measured. Presented here are the results of these calibrations, which were applied during the analysis process.

3.1 Gain Calibration

With each change in hardware or high-voltage setting, the overall gain of the camera shifts. Traditionally, new selection criteria are developed for each gain value by re-optimizing the gamma-ray cuts on a large set of Crab Nebula data taken during

each epoch. However, if one wants to combine data from multiple seasons or perform a detailed spectral analysis, these shifts must be taken into account in a more general fashion. The procedure used in this analysis is to calculate the gain factor for each season (relative to a chosen standard season) and scale the SIZE, MAX1, MAX2, and MAX3 shower parameters accordingly so that data from a range of epochs can be combined using the same set of cuts.

The overall gain factor can be measured by looking at muon events. Muons are produced as byproducts of charged pion decay in hadron-induced air showers and propagate to Earth's surface. Muons, like all charged particles, emit Čerenkov light in cones as they propagate through the atmosphere, where the angle of the cone, θ, can be found with the following formula:

$$\beta \sin^2 \theta_c = \frac{1}{\gamma_0^2} - \frac{1}{\gamma^2} \tag{3.1}$$

where γ is the Lorentz-factor of the particle and γ_0 is the minimum Lorentz factor for Čerenkov emission. Given the energy spectrum of muons in the atmosphere, one can show that most muons have Lorentz factors $\gamma \gg \gamma_0$, so the cone angle can be very crudly approximated by the saturation Čerenkov angle $\sin \theta_c \approx 1/\gamma_0$. The Čerenkov light from an electron looks like a fuzzy ring, that is actually made up of many cone-shaped emissions that are jittered around by multiple scattering in the atmosphere. The ring structure is lost since the electron Coulomb scattering angle is large compared with the angle of Čerenkov light emission. Muons have the same electric charge as electrons, but a much larger mass, and therefore a much smaller

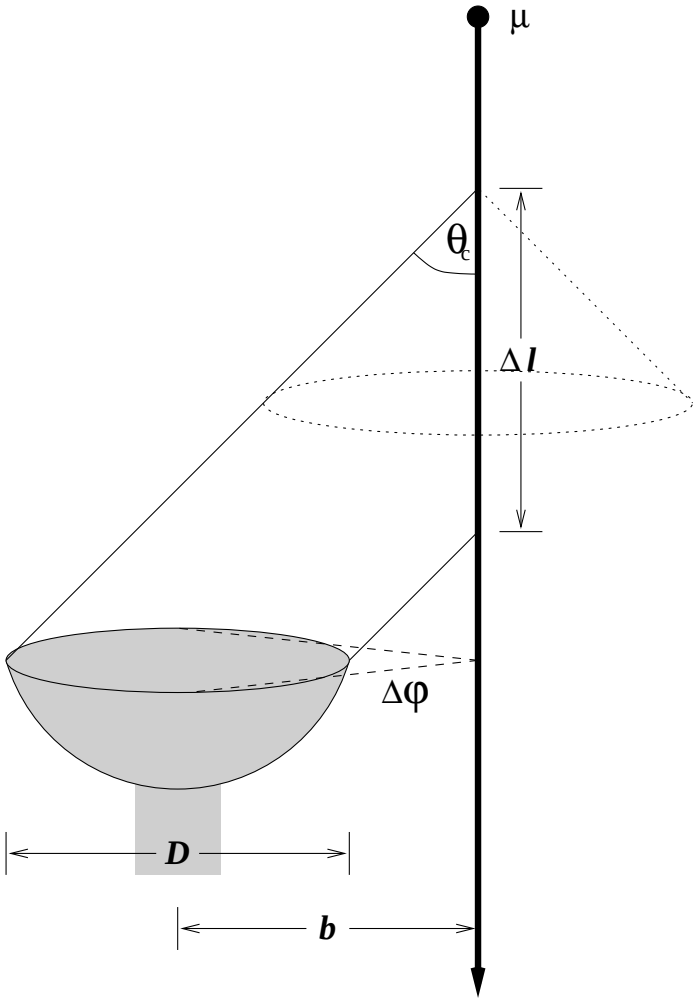

FIGURE 3.1: The geometry of a muon event with impact parameter b arriving in the spherical mirror of an ACT. The muon arrives from the top producing Čerenkov light in cones with angle θ_c such as the one shown with dotted lines. The light produced during path-length Δl makes it into the mirror, which has diameter D.

Coulomb scattering angle—small enough that muons travel in approximately straight lines through the atmosphere, producing well-formed ring images.[1] The amount of Čerenkov light from a muon that is incident on the mirror of an ACT is proportional to the path-length Δl as shown in Figure 3.1. As parallel rays are focused to a point in a spherical mirror, Čerenkov light emitted at a constant angle in nested cones will be focused to a ring by the telescope. Depending on the impact parameter, only a subset of photons with azimuthal angle ϕ subtended by the dish will result in an image on the camera. Therefore, a muon coming straight down the camera axis will produce a complete ring image in the camera, while one with an offset trajectory will produce an arc, with diminishing arclength $\psi \propto D/b$ as the impact parameter, b, increases.

The light emitted by a muon per unit path-length ($\partial L/\partial l$) is proportional to $\sin^2\theta_c$ (Frank and Tamm, 1937). The path-length Δl can be written as $D/\tan\theta_c$ where D is the diameter of the mirror. The total light falling on the telescope, L, is then:

$$\begin{aligned} L &\simeq \frac{\partial L}{\partial l}\cdot\Delta l\cdot\frac{\Delta\phi}{2\pi} \\ &= \sin^2\theta_c\cdot\frac{D}{\tan\theta_c}\cdot\frac{\Delta\phi}{2\pi} \end{aligned} \tag{3.2}$$

Since the arc-length of a muon image is proportional to $\Delta\phi$, one can see that the Čerenkov light per unit arc-length produced by a muon is

$$\frac{L}{\text{arclength}} \simeq \sin^2\theta_c\cdot\frac{D}{\tan\theta_c}\cdot\frac{\Delta\phi}{2\pi}\cdot\frac{1}{\Delta\phi}, \tag{3.3}$$

[1] The effect of the change in Čerenkov angle due to increasing atmospheric density is small compared to the resolution of the detector.

which is a *constant* independent of impact parameter and direction. The approximate constancy of the muon light per arclength makes the LENGTH/SIZE cut an effient means of rejecting muon triggers and also implies that muon rings (at the saturation radius) provide an excellent tool for measuring the absolute gain of the camera. In the next section, I describe the detailed procedure for measuring the mean signal/arclength for a large set of muon events.

3.1.1 Selecting Muon Events for Gain Calibration

While muon and proton events are easily rejected using the standard Hillas parameter image technique, selecting only ring-like muon images is surprisingly difficult using computational techniques. The procedure described here is only partially effective at selecting muon events (it is fooled by many proton events) therefore the final decision for each candidate muon event was made by eye.

Algorithm for Detecting Arcs in Images

Muon arcs are detected using the following procedure:

1. For each set of three pixels in the image (from now on referred to as a *triplet*), we assume the pixels lie on an arc, and calculate the position of the assumed ring-center by drawing the perpendicular bisector lines between them and finding their intersection point. A perpendicular bisector is a line drawn at a right angle to the line segment connecting two pixels, beginning at the mid-point between them. This is shown pictorially in Figure 3.2. Compared with fitting,

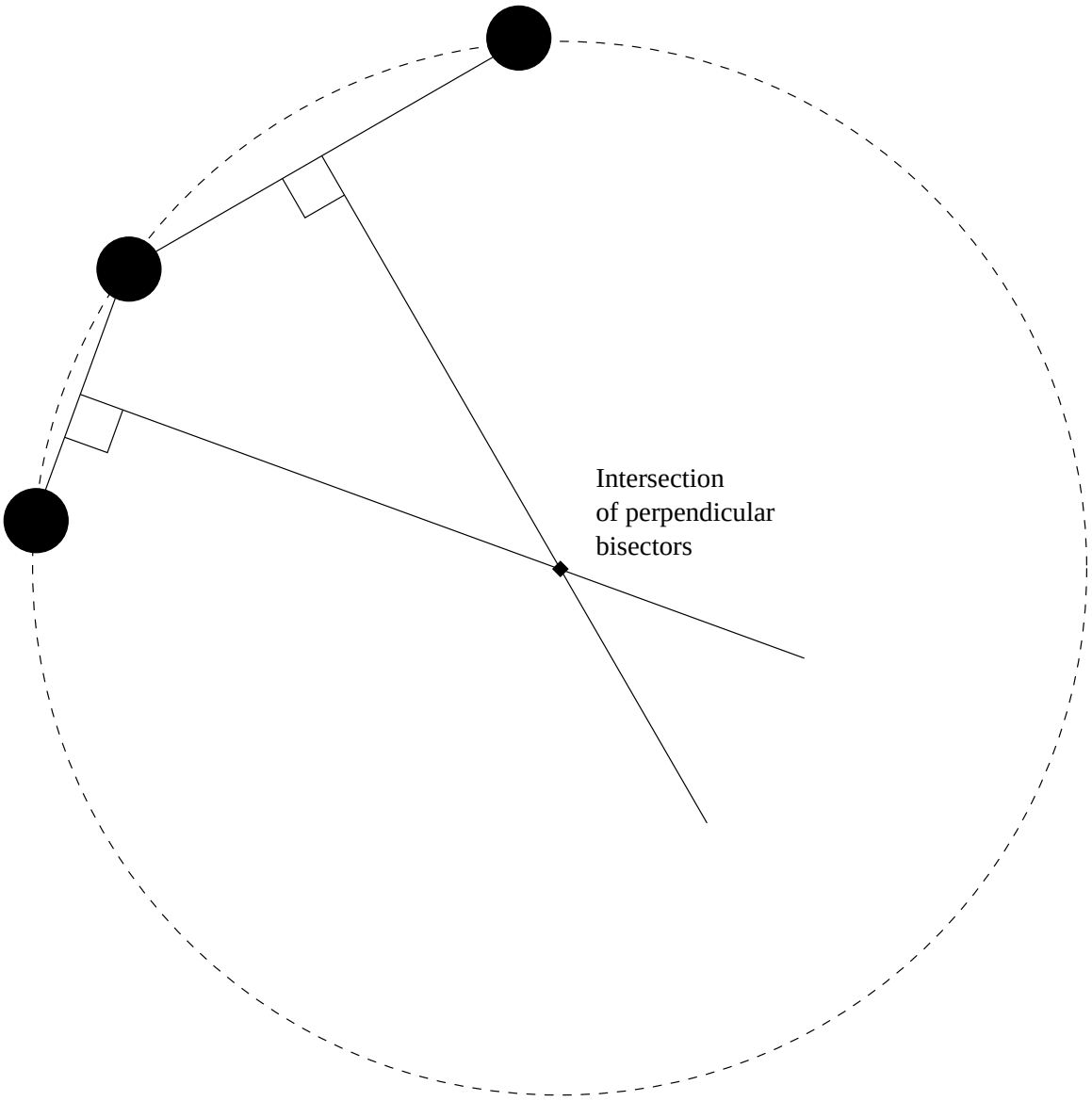

FIGURE 3.2: The center of a ring passing through any three points can be found by calculating the intersection point of the two perpendicular bisectors drawn between them. The dotted line shows the ring corresponding to the triplet center position.

this procedure is robust and fast but is still computationally intensive given the $n(n-1)(n-2)/3!$ triplets in an image of n pixels.

2. A 2-D histogram of triplet center positions is generated. At each point in the histogram, the running average radius, center position and also an n-bit mask (where n is the number of camera pixels) is stored. When a triplet center bin is incremented the pixels contributing to the center are *or*-ed into the bit-mask. The resulting 2-D histogram can be thought of as the original image transformed into "ring-center space", where bright spots in this correspond to positions of the centers of ring-like structures in the original.

3. The next step is to find the grid position (index) of the boxcar-smoothed "ring-center space" image which contains the maximum number of triplet centers. This corresponds to the center of the most arc-like part of the image, and the bit-mask contains the pixels in the original image that contributed to the arc. The average center position (x, y) for this bin, and the radius r, are extracted from the corresponding arrays at this index. We also generate a distribution of the angle of a vector from the most probably ring center to each pixel contributing to the ring (ϕ) . The contributing pixels can be looked up in the bitmask)

4. Next, we derive the following set of parameters useful for characterizing the arc:

   Arcstrength The fractional number of ring centers in the peak bin compared to the total number of centers.

Muskew Length of the vector from the centroid of the distribution to the ring-center divided by the ring-radius.

Arcangle (η) The length of the arc calculated from the second moment of the ϕ distribution. $\eta \cdot r$ gives the length of the arc.

Total Signal (S_{tot}, S_{arc}) We loop through *all* pixels, calculating the total amount of light in an annulus around the ring (S_{tot}) and the total light in the annulus which is within an angular distance less than η (S_{arc}).

SOAL The signal per unit arc-length is the integrated signal in the arc segment (S_{arc}) divided by the arc-length (SOAL $\equiv S_{arc}/(\eta \cdot r)$).

Muonness We also calculate the degree of "*muonness*", defined as S_{tot}/SIZE. Events with high *muonness* are likely muon candidates. It is possible to improve this measure by including such factors as the smoothness of the ϕ distribution or the radial spread of the pixels in the arc.

5. Finally, using we events with *muonness*$>$ 0.7 are selected as candidate muon events. An example of a muon fit based on this procedure can be seen in Figure 3.3.

3.1.2 Gain Correction Results

Table 3.1 shows the average signal per arclength for several Zenith runs taken in June or July of each season (at about the same time as the data taken of the Galactic

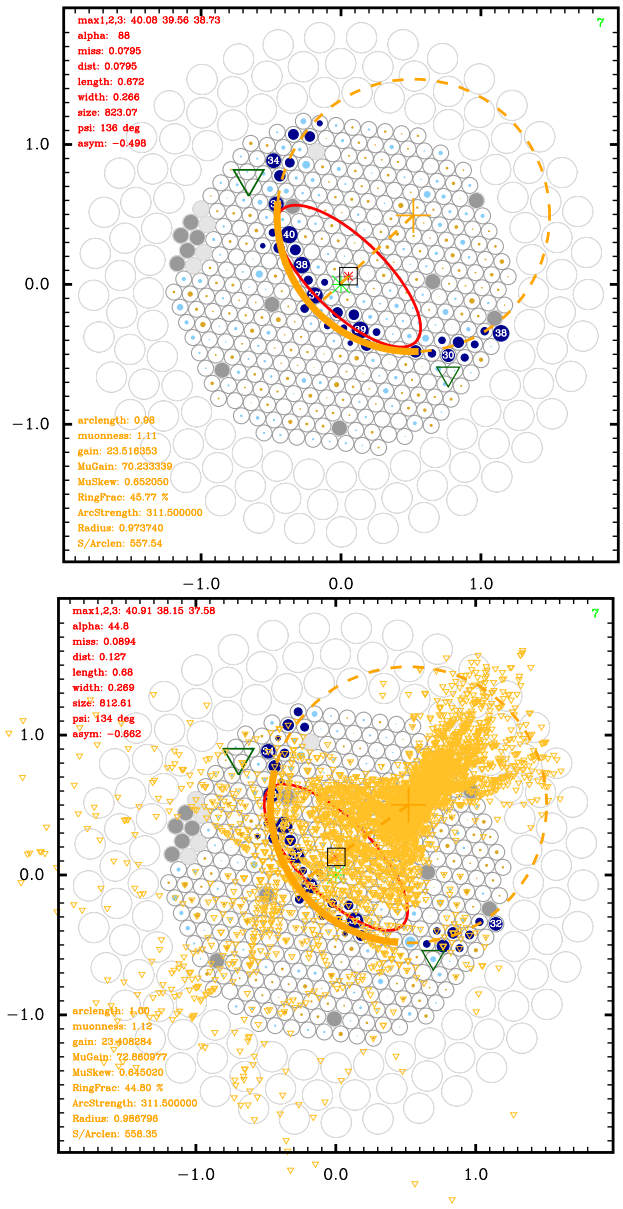

FIGURE 3.3: The first image shows a fit to a muon arc event using the arc-selection algorithm. The dotted line shows the ring fit, the solid part of which is the length of the arc used to calculate the signal/arc-length. The solid ellipse is the standard Hillas parameterization of the event. The second is the same image with a subset of the triplet centers over-plotted showing the centroid in ring-center space.

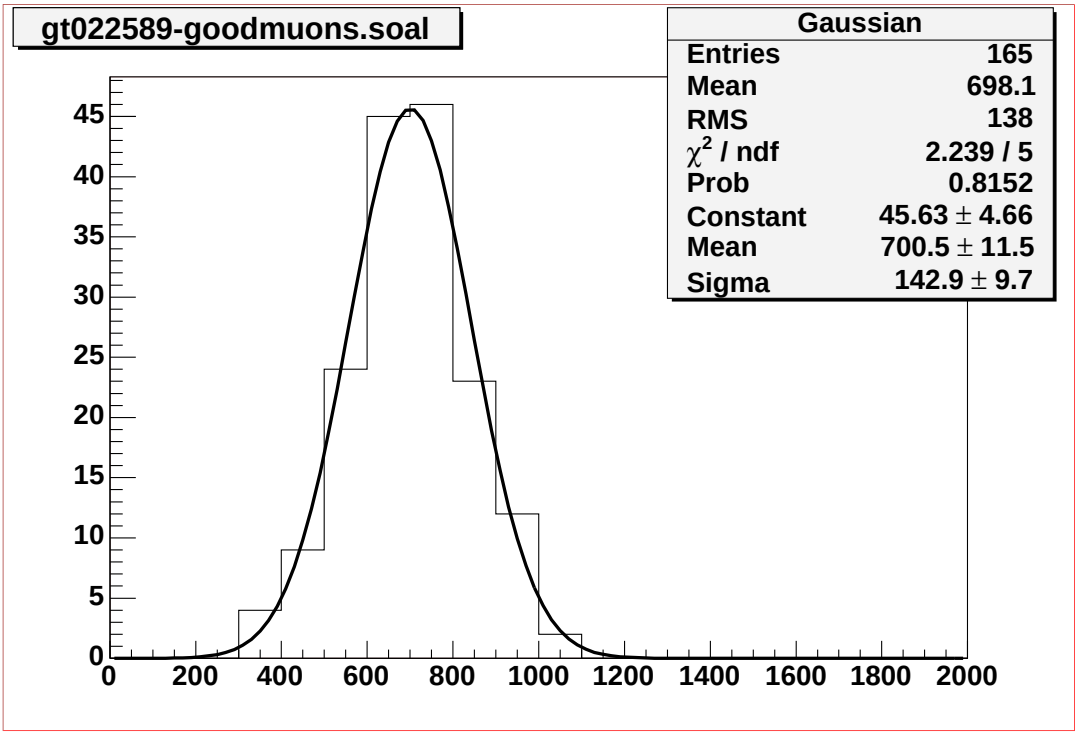

FIGURE 3.4: Example of a signal-per-arclength distribution for a particular run.

		Peak S/Arclength			P.E./D.C. factor
run ID	**Date**	**SOAL**	σ	N_{events}	**g**
05555	June 1996	340.2	9.8	86	1.0
18043	June 2001	799.9	12.7	187	0.4462
22589	July 2002	700.5	11.5	165	0.5095
24917	June 2003	669.9	17.7	93	0.5352
27279	June 2004	747.5	15.5	124	0.4776

TABLE 3.1: Peak signal/arclength values for several seasons. N_{events} is the number of muon events used in the calculation. The correction factor scales the camera gain relative to run 05555, where the P.E./D.C. ratio is approximately 1.0.

Center). Historically, we do not separately change the PMT quantum-efficiency or mirror-reflectivity values for simulations of different seasons or take them into account for instrument calibration. Instead, all these seasonal values are absorbed into the gain factor converting detected photoelectrons to digital counts (D.C.)[2] . Since the photoelectron to digital count ratio ($g \equiv P.E./D.C.$) was measured to be approximately 1.0 in 1996, we chose the muon signal per arclength from that season as the "standard" and compute relative gain correction factors for each successive season. Multiplying the SIZE, MAX1, MAX2, and MAX3 values for events from any season by the corresponding correction factor has the effect of matching the gains and photon detection efficiency between them. To show that the scaling is reasonable, we plot the LENGTH/SIZE distribution (another crude statistic reflecting the gain changes) of several runs with and without the scale factor applied in Figure 3.5.

[2] More precisely, we should refer to this gain factor as the ratio of incident photons to digital counts, but the term P.E./D.C. is deeply ingrained in the Whipple Collaboration nomenclature!

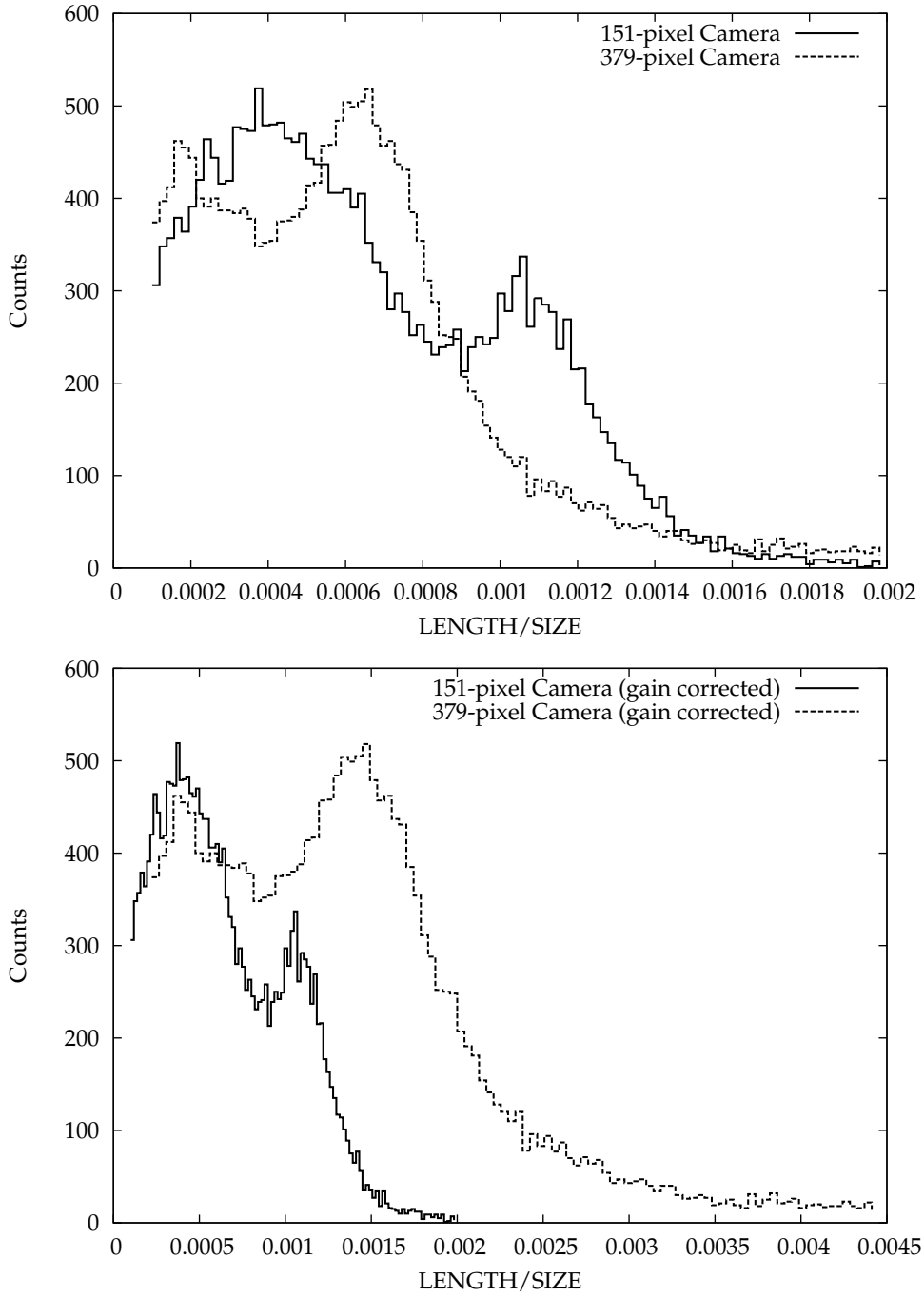

FIGURE 3.5: LENGTH/SIZE histograms for the 151-pixel and 379-pixel cameras. The top shows the raw LENGTH/SIZE distribution, while the gain correction factor has been applied in the bottom. The gain correction factor allows the same LENGTH/SIZE cut (~ 0.0008) to be used for both data sets.

3.2 Pointing Calibration

Knowing the precise position on the sky at which the telescope is pointing is critically important when looking for emission from a weak source since there must be a clear *a priori* reason to determine the detection significance at a particular point in the field-of-view, and selecting the peak significance introduces a hidden trials factor. Though the Whipple Telescope's tracking system provides relative positions with a precision of a few arc-minutes, we found that the absolute pointing errors can be much larger, and observations taken at low elevation can be particularly problematic due to flexure of the optical support structure. The degree of pointing error can be measured by looking at the position of known stars in the field of view.

Since stars do not emit gamma rays, it is necessary to construct an optical image of the sky from the camera to determine their positions. Fortunately, since the phototube pixels in the camera are designed to look at optical Čerenkov flashes, it is possible to use them to make a low-resolution image of visible sky. Though the PMT signals are AC-coupled at the input of the digital-to-analog converters, the presence of visible light in the field of view (other than the Čerenkov flashes which trigger the telescope) adds to the pedestal *variance* in the corresponding pixel. By rotating into a common frame and accumulating the pedestal variations of each pixel into a two-dimensional histogram, an optical *sky-brightness* map may be generated from *any* observation. These maps can be used to determine the absolute pointing error as well as for combining a series of observations which have differing pointing offsets.

RunID	dx (°)	dy (°)
gt025109	0.0402	0.0603
gt025110	0.0517	0.0660
gt025111	-0.0345	0.0920
gt025112	0.0258	0.0833
average	0.0208	0.0754
std error	±0.0197	±0.0073

TABLE 3.2: Pointing error measurements for each run taken on the two pointing-check stars.

The full algorithm for generating a skybrightness map is shown in Section D.1.

The absolute pointing error for the Galactic Center observations was measured by looking at special observations taken with the telescope pointing at two stars that were at approximately the same elevation as the Galactic Center. *Sky-brightness* maps were generated for each observation (without de-rotation, since we were looking for an altitude/azimuth offset in the camera), and the deviation of the centroid of the star light from the center position of the camera was measured. Figure 3.6 shows one such observation. We find that the telescope has a pointing error in elevation of $0.754 \pm 0.007°$ for the 2003 season (see Table 3.2), and this is attributed to the sagging of the optical support structure of the telescope when pointed at low elevation.

To correct for this error, we translate the coordinates of each camera pixel by the measured offset prior to parameterization. This must be done before derotation of the images because the offset is fundamentally in the "altitude/elevation" coordinate frame, and not related to the right-ascension or declination of the source (RA/Dec coordinate). Figure 3.7 shows an image of the Crab Nebula at large zenith angle with and without the pointing offset correction. Note that the corrected image is better

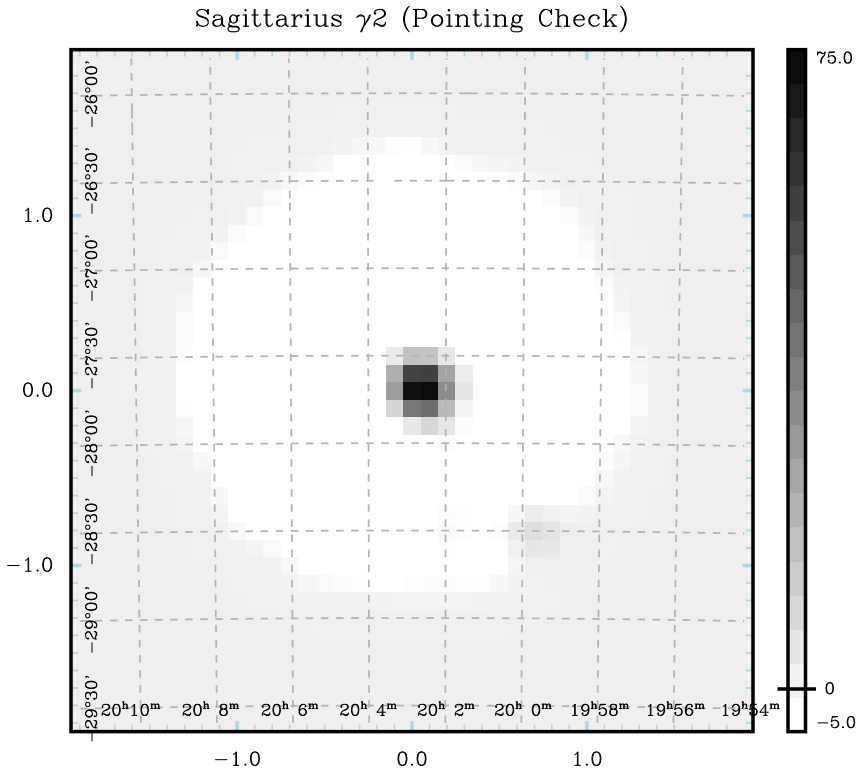

FIGURE 3.6: An optical *sky-brightness* image of a pointing star (Sgr γ_2). This star was one of two used for calibrating the absolute pointing error of the telescope at low elevation.

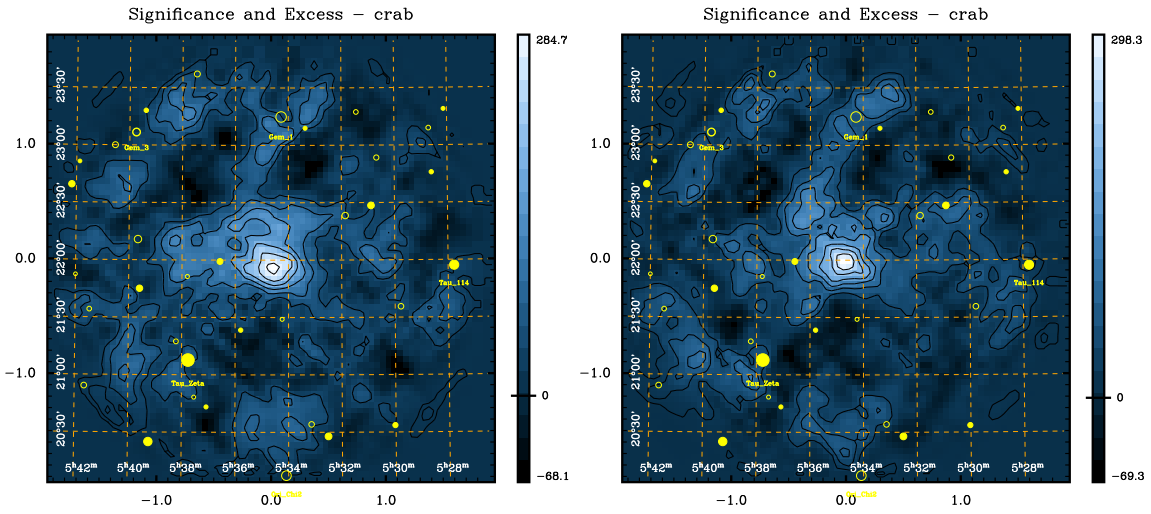

FIGURE 3.7: These figures are 2D images of the Crab Nebula taken at large zenith angle ($\sim 29°$). The left figure is without any pointing corrections, while the right figure has an elevation-offset of 0.0754° applied to each run before parameterization. After correction, the centroid of the gamma-ray emission moves to the (0,0) position and becomes brighter.

centered and brighter, since images analyzed with an elevation offset get smeared out due to camera rotation during the run.

3.2.1 Relative Pointing Error

Often, it is necessary to combine several observations that were taken at slightly differing RA/Dec offsets from a particular source location, for instance if the coordinates derived from the encoders were slightly inconsistent or if the location source in the tracking computer were marginally incorrect. *Sky-brightness* maps generated for each data run can be used to move the two-dimensional images for each observation to a common center point (a procedure called *stacking* in optical astronomy.)

Assuming each observation contains similar stars or brightness variations, the

relative offset between any pair of runs can be measured by cross-correlating their respective sky-brightness maps and finding the peak correlation. The cross-correlation, C of two images A and B is found with the following formula:

$$C_{ij} = \sum_m \sum_n A_{mn} B_{(m+i)(n+j)} \tag{3.4}$$

To combine all images, a run is chosen as the "standard", and each other run is cross-correlated with it. When the images are summed to produce the final output, the resulting coordinate shift is added to the point of origin for each event. To test this procedure, we combined several Crab Nebula runs taken centered on the camera with several taken with a -0.5° offset in declination. We then analyzed the data with the blind cross-correlation procedure, which correctly aligned all images (as demonstrated in Figure 3.8.)[3]

[3] It should be noted that this procedure does not always work well for observations where many pixels are manually turned off to avoid bright stars in the field-of-view (as is often the case with data from the Crab Nebula). Pixels disabled in hardware create holes in the sky-brightness map which throw off the cross-correlation algorithm.

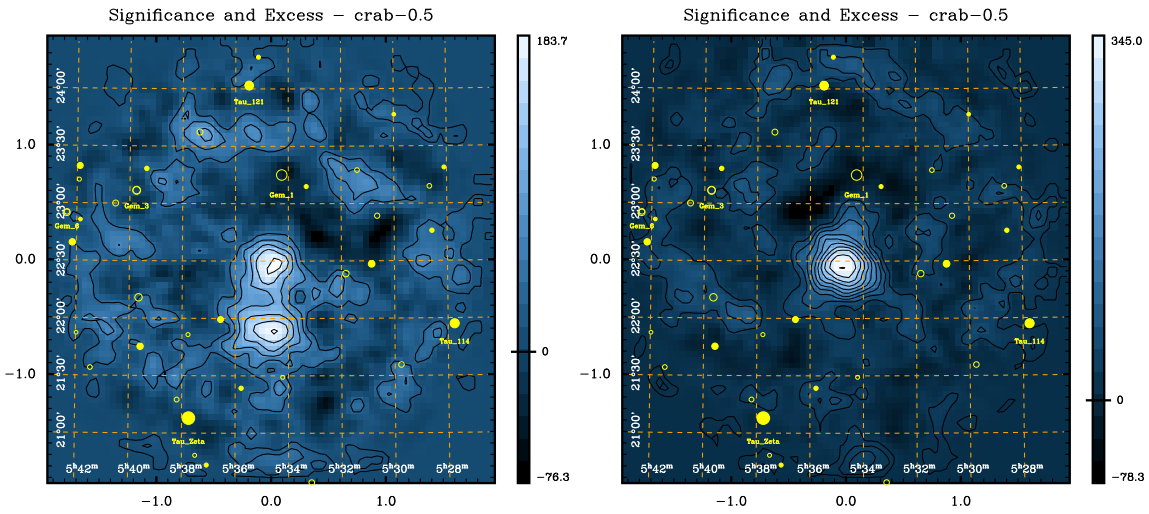

FIGURE 3.8: A test of the relative alignment procedure. The figure on the left shows the results of the 2D analysis for a set of runs taken of the Crab Nebula that combines 3 on/off runs taken with the source centered in the field of view, and 6 runs taken at an offset of 0.5° (to simulate a badly mis-aligned run). The peaks from the two combined data sets are clearly visible. In the right figure, the same 9 runs have been processed with the relative stacking alignment, which automatically shifted the offset data to the center by analyzing the sky brightness maps.

Chapter 4

Results

The Whipple observations of the Galactic Center region were originally made to place an upper limit on gamma-ray emission from Neutralino Dark Matter annihilation from a cusp centered on the position of Sgr A*, as described in Chapter 1.2.2. Though this area emits brightly at other wavelengths, we did not expect to see any appreciable TeV emission (from an astrophysical source or from dark matter annihilation) and made every attempt to avoid biasing our results toward detection. All analysis techniques were developed *a priori*, optimized on data that were *not* part of the Galactic Center data set, and were applied first to independent data from the Crab Nebula—only after the data analysis was proven was it applied to the Galactic Center.

Since the Galactic Center region is one of the most difficult locations to observe (due to low elevation, large optical background, source confusion, etc.), calibration of the telescope attention to systematic errors in our analysis techniques was extremely

important.

In the end, the observations lead to the detection of a source of TeV gamma-rays from the Galactic Center, with no clear astrophysical mechanism for its production. Empirically, our results show a very high energy measurement with a flat spectrum extending above 3 TeV, and no evidence for variability over the period 1995-2004.

4.1 Observations

The Galactic Center ($\alpha = 17^h45^m40^s,\ \delta = -29°00'28''$, J2000) transits at a very large zenith angle (on average 61°) as seen from the latitude ($30.4°N$) of the Whipple Observatory and is only visible for a few hours each night during the months of May through July. Because of these limitations and scheduling conflicts with other sources, the total exposure time on the Galactic Center was 31 hours (62 hours including OFF-source observations), though observations were made over the course of the 1995,1996,2001,2002,2003, and 2004 seasons. Observations were taken in OFF-ON mode, with the OFF-source observation offset 30 arcminutes in right-ascension *before* the position of Sgr A* to deal with a bright field of view in the standard OFF region. Further complicating matters, the Whipple camera was upgraded twice over the course of this time period. During the 1995-1996 observing seasons, the camera consisted of 109 pixels (each with 0.26° diameter); it was upgraded at the end of 1996 to 151 pixels and again in 1999 to 379 smaller-diameter (0.12°) pixels. The *EZCuts* data selection criteria described in Section 2.3.2 were developed for low-elevation

	ON	OFF
Number of Runs	55	55
Duration (min)	1529	1526
Total Events	897841	904830
Passing Trigger Cuts	252295	252516
Passing Shape Cuts	39089	38215
Passing Orientation Cut	6452	6063

TABLE 4.1: Summary of the Galactic Center data set. Detailed run-by-run statistics are given in Appendix C.

observations and to take care of the changes in Camera geometry. A summary of the Galactic Center data set is shown in Table 4.1, while the detailed run-by-run results are given in Appendix C.

For the flux and variability measurements, data from the 1995-2003 seasons were used (totaling 26 hours exposure), while the spectral analysis, which was done later, included the 2004 data.

4.2 Emission from the Galactic Center

We have combined all observations of Sgr A* from 1995 through 2003 resulting in 26 hours of on-source exposure at an average zenith angle of 61° using the EZCuts analysis (§2.3.2). Following the procedure outlined in Section 3.2, observations were also taken centered on two nearby bright stars at the same average elevation as Sgr A* to determine the pointing offset. Figure 4.1 shows the resulting 2-D map of gamma-ray excess with overlaid significance contours. The true center of the camera, correcting for the offset, is plotted as a cross in the image. This image shows a 4.2

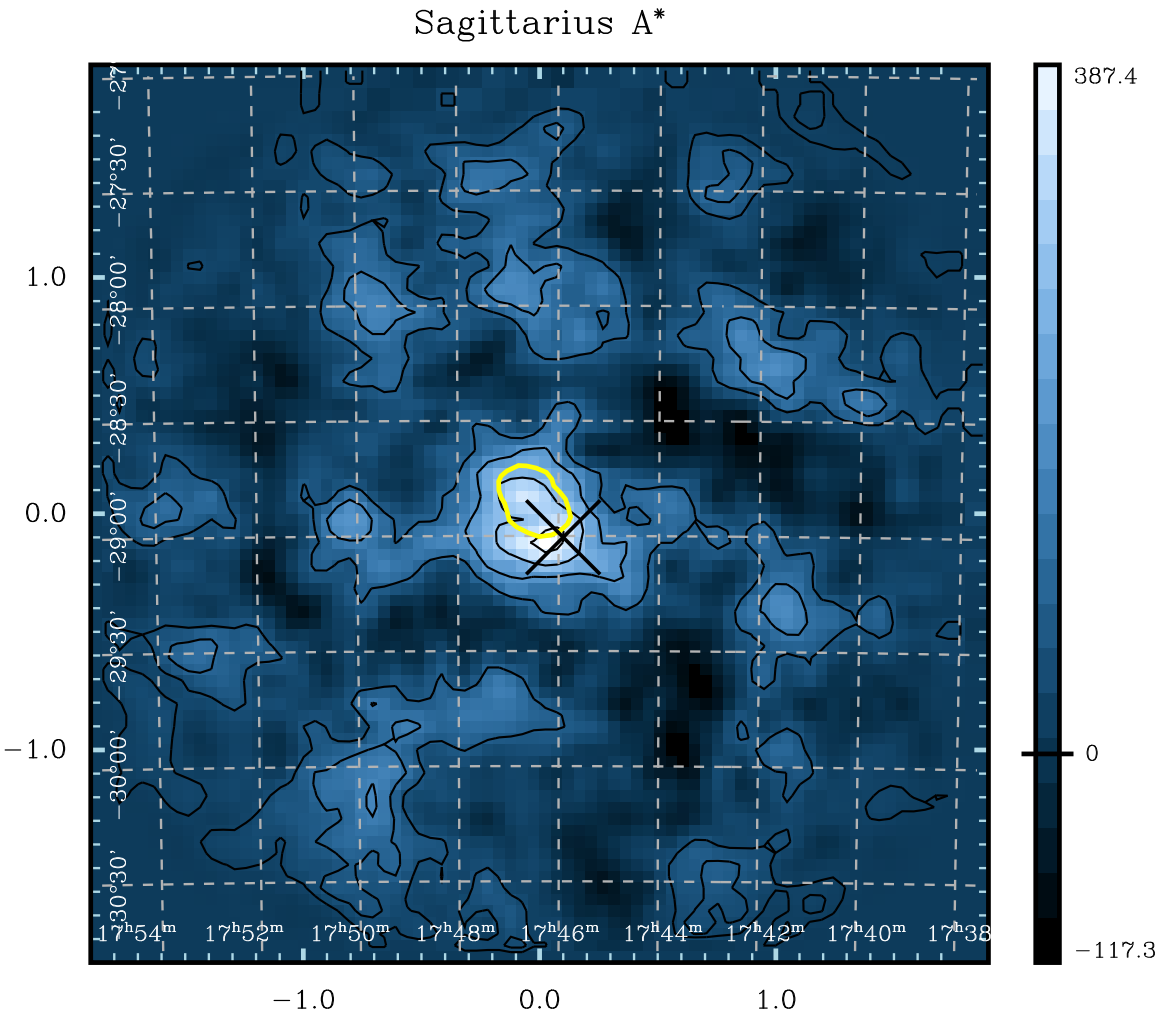

FIGURE 4.1: A gamma-ray image of the region around Sgr A*. The image is of excess counts with overlaid significance contours (1 standard deviation per contour). The axes are labeled in degrees from the assumed camera center. The true center position of the camera, which is not exactly at (0,0) due to flexing of the telescope at low elevation, is marked with a cross. The dashed lines are the RA and Dec contours at this position. Also shown (as a light contour) is the 99% confidence region for the EGRET observations (Hooper and Dingus, 2002).

standard deviation (σ) excess at the corrected center position.

After first running our full analysis on the Galactic Center data, we noticed that the final statistical significance varied each time the analysis was run anywhere from

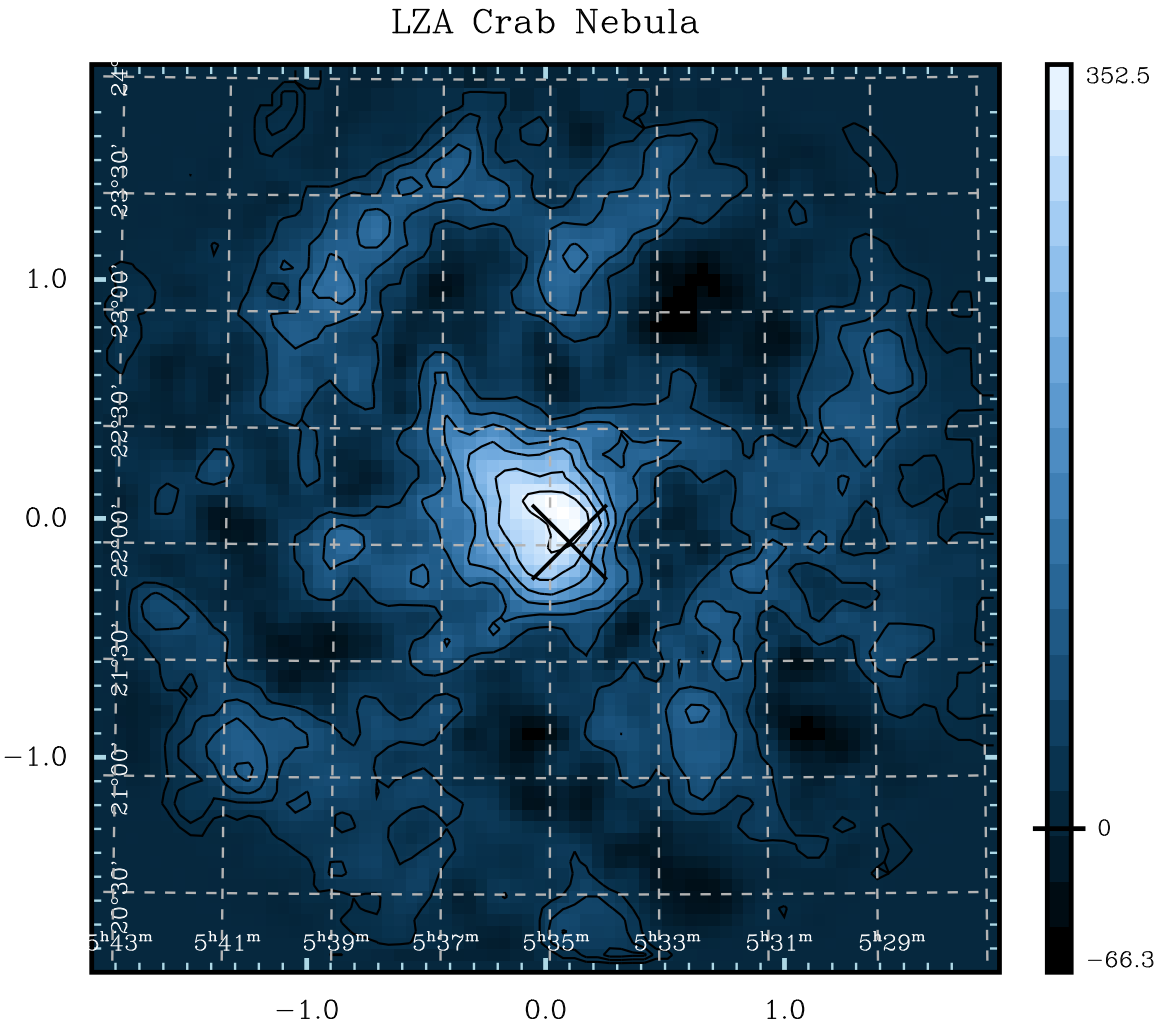

FIGURE 4.2: A gamma-ray image of the Crab Nebula taken at large zenith angle ($\approx 62°$) using the same analysis procedure used for the Galactic Center (Figure 4.1). The center position corrected for measured pointing offset is plotted in the image, though corrections to remove this offset have not been applied here.

3 to 5 σ. This variation turned out to be due to the Gaussian *padding* procedure described in Section 2.2.3. The point-of-origin in our two-dimensional analysis is sensitive to the the random noise injected into each event, and the number of events passing cuts also depends on the exact signal levels; both effects can indirectly lead to variations in the final significance when all events are accumulated into the two-dimensional image. In order to account for this in a conservative way, we devised a technique referred to as *hyper-padding* whereby we re-ran the analysis ten times and took the average significance, which though somewhat lower than the "best" result, is more conservative. We find the average significance at the corrected center position is (3.7 ± 0.13) σ, somewhat below the initial result. For reference, in Figure 4.2 we show the results of the same analysis procedure applied to 10 hours of observations of the Crab Nebula at a similar zenith angle range. Note that the significance of 7σ of the Crab detection at the offset position is substantially higher than the result of 3.8σ obtained applying the standard small zenith angle analysis procedure to these LZA data. Also, the similar angular extent in the LZA Crab and Sgr A* results indicates consistency with a point source within a 95% confidence region of radius ≈ 15 arcmin.

4.3 Gamma-ray Flux from the Galactic Center

To facilitate comparison with other detectors, the flux of gamma rays from the Galactic Center is calculated relative to the measured flux from the Crab Nebula. To define an absolute energy scale, the peak energy at which the flux is measured must

be calculated from simulations. To determine the peak energy of the detected flux from the Galactic Center, we use the canonical procedure of first assuming a spectral index close to that of the Crab Nebula, then calculating the peak energy for a Crab-like spectrum. First, we simulated gamma rays with a Crab Nebula spectrum (with integral spectral index $\gamma = 1.58$) (Mohanty et al., 1998) and a zenith angle of 61°, and analyzed the resulting data with a detector simulation and our analysis software. We determined the peak detected energy to be ≈ 2.8 TeV, with a 20% systematic error in this energy threshold. We then analyzed a set of contemporaneous LZA Crab Nebula data runs to find the Crab count rate and compared this to the corresponding rate for the Galactic Center. The integral flux for the Galactic Center, normalized to the Crab flux, is then:

$$F_{GC}(> 2.8\ \mathrm{TeV}) = N_{0,\mathrm{Crab}} \cdot (2.8\ \mathrm{TeV})^{-\gamma}/\gamma \cdot \frac{R_{\mathrm{GC}}}{R_{\mathrm{Crab}}} \tag{4.1}$$

Where $N_{0,\mathrm{Crab}}$ is the flux normalization factor for the Crab Nebula ($3.12{\times}10^{-7}\mathrm{m}^{-2}\mathrm{s}^{-1}$), γ is the integral Crab spectral index, and R_{GC} and R_{Crab} are the corresponding Galactic Center and Crab Nebula gamma-ray count rates. From the LZA Crab data, with corrections applied for a low-elevation pointing-offset, we find a gamma-ray rate of $R_{\mathrm{Crab}}(> 2.8\ \mathrm{TeV}) = 0.652 \pm 0.09$ photons min^{-1} and from the Galactic Center analyzed in a similar manner, we obtain an average rate of $R_{\mathrm{GC}}(> 2.8\ \mathrm{TeV}) = 0.141 \pm 0.05$ photons min^{-1}. Hence, the gamma-ray flux from the GC region above 2.8 TeV is $(5.3 \pm 1.9) \cdot 10^{-9}\,\mathrm{m}^{-2}\mathrm{s}^{-1}\mathrm{TeV}^{-1}$ or about 22% of the Crab Nebula (the flux

error includes the uncertainty in the Crab Nebula measurement).[1]

4.4 Galactic Center Spectrum

Data Set	N_0 ($m^{-2}s^{-1}TeV^{-1}$)	γ_0
SZA Crab	$(6.14^{+0.21}_{-0.48}) \cdot 10^{-7}$	$-2.57^{+0.07}_{-0.09}$
LZA Crab	$(3.30^{+0.40}_{-0.43}) \cdot 10^{-7}$	$-2.59^{+0.08}_{-0.09}$
Old SZA Crab	$(4.15^{+0.05}_{-0.50}) \cdot 10^{-7}$	$-2.25^{+0.06}_{-0.1}$
Galactic Center	$(3.87^{+1.61}_{-2.04}) \cdot 10^{-8}$	$-2.44^{+0.22}_{-0.48}$

TABLE 4.2: Spectral fit results for each data set.

Following the Forward-folding spectral reconstruction procedure outlined in Section 2.5, a spectrum was derived for the Galactic Center region. For comparison (and to verify the technique), we also derived spectra for the Crab Nebula at small zenith angle in the 1995/1996 season and large and small zenith angle during the 2000-2003 seasons. Figure 4.3 shows the resulting spectra, while the model fits and parameters are shown in Figure 4.4 and Table 4.2 respectively. Because the normalization factor

[1] It should be noted that the flux originally quoted in Kosack et al. (2004) was approximately 3 times larger than the flux shown here. This was due in part to an error in the pointing correction for the LZA Crab Nebula analysis and the inclusion of two poor-quality LZA Crab runs taken at overly-large zenith angles, which caused the Crab rate to appear lower than its true value—thus affecting the normalization factor for the Galactic Center. This error in the Crab rate was fixed less than two months after the publication came out, yielding this corrected result.

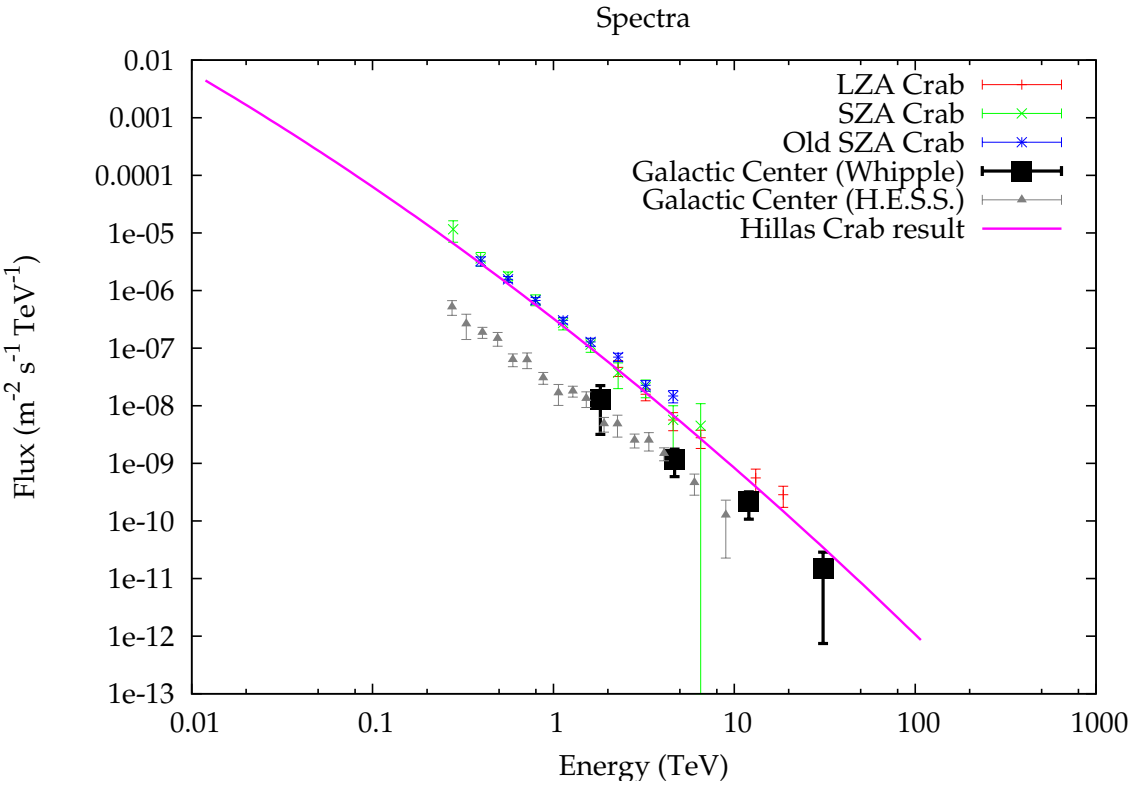

FIGURE 4.3: The results of the spectral analysis for the Galactic Center are shown as black boxes. Also plotted are the results of the same spectral analysis applied to various Crab Nebula data sets. The LZA Crab set is at the same elevation as the Galactic Center data, the SZA data was taken at small zenith angle, and the Old SZA set were taken at small zenith angle in the 1995-1996 season (representing an older version of the Whipple Camera). The solid line is a functional result for the Crab Nebula spectrum as measured by Hillas et al. (1998). Overlaid in triangles are the more recent spectral results from the H.E.S.S. array (Aharonian et al., 2004), which agree well with the Whipple spectra.

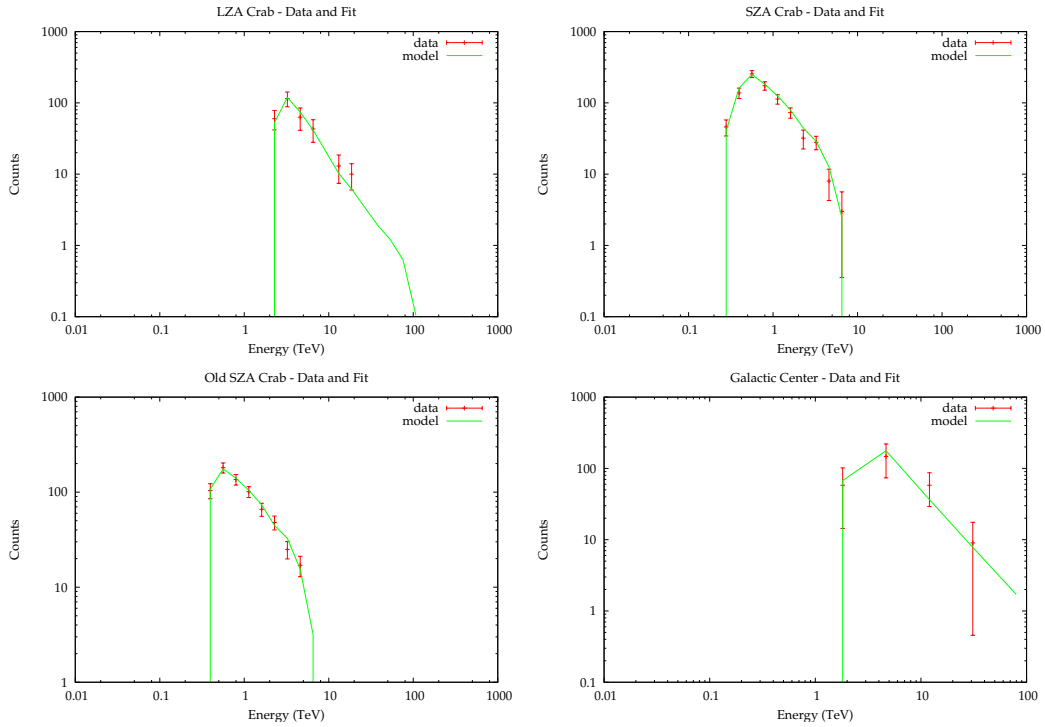

FIGURE 4.4: Forward-folded model fits for each dataset shown in Figure 4.3.

(N_0) gives the flux at 1 TeV and because the Galactic Center spectrum is flatter than that of the Crab, the normalization factor for the Galactic Center is only about 12% of the Crab, while the flux at the peak energy is 22% of the Crab at the same energy. Due to the low statistics of the Galactic Center observations, the spectrum can be thought of as an upper-limit only and not a definitive result. For further comparison, the results of a more-recent spectral analysis from the H.E.S.S. collaboration, are shown (Aharonian et al., 2004), which agree quite well with the Whipple result. The H.E.S.S. results, taken with a second-generation telescope in the Southern Hemisphere over the course of one year, contain more statistical significance due to the longer observation times and lower energy threshold for the Galactic Center available at that latitude.

4.5 Variability Analysis

The count rate from the Galactic Center observations is shown as a function of time in Figure 4.5. To determine the probability for steady emission, a χ^2 fit of a constant function ($f(t) = A$) was applied to this data and, for comparison, to a series of data taken of Markarian 421 (a TeV Blazar which is known to be highly variable) at a similar zenith angle range as the Galactic Center. The total significance of this Markarian 421 data sample was 2.3σ. The Galactic Center data yields a constant count rate of $6.12 \pm 1.59\ \gamma \cdot \mathrm{min}^{-1}$ with a reduced χ^2 of 1.13 (with 54 degrees of freedom), a remarkably good fit considering the changes in the Whipple instrument

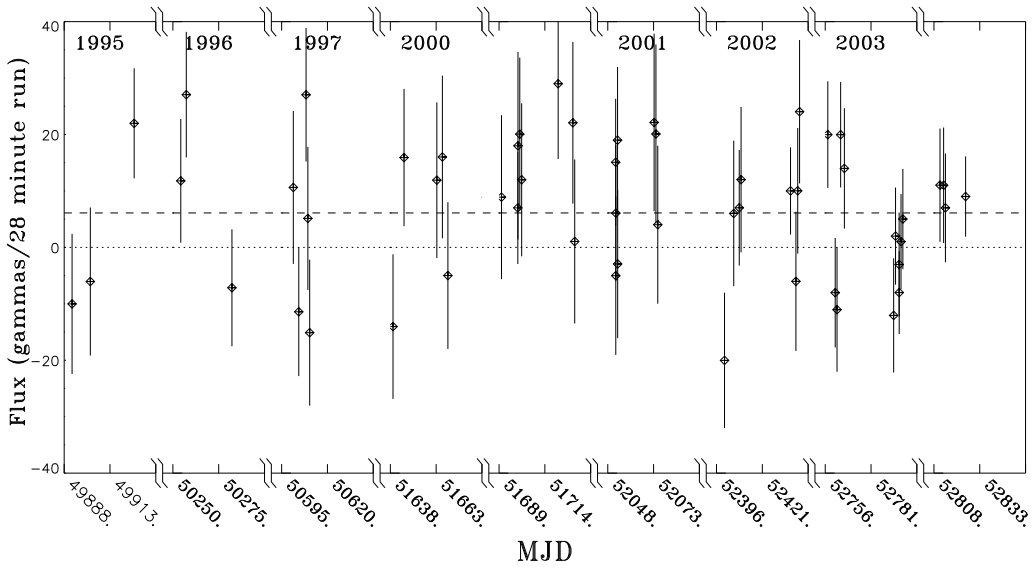

FIGURE 4.5: Gamma-ray count rate for the Galactic Center as a function of time. Each data point represents a single 28 minute observation. Time gaps in the data have been removed where indicated. The dashed line is a least squares fit of a constant function to the data.

over the observing period. There is a 25% chance of obtaining a χ^2 value this large or larger if there is no variability. The result for Mrk 421 yields a constant count rate of $6.86 \pm 6.13\ \gamma \cdot \mathrm{min}^{-1}$ with a reduced χ^2 of 3.03 (with 6 degrees of freedom). In this case, there is only a 1.2% chance of obtaining this χ^2 if there is no variability. Though this method is by no means statistically rigorous, it provides some indication that the VHE source at the Galactic Center is not dramatically time variable.

Chapter 5

Discussion

5.1 Comparison with other TeV Observations

5.1.1 CANGAROO Detection

The CANGAROO collaboration, which operates an ACT in Australia (CANGAROO-II), has also detected TeV emission from the Galactic center (simultaneously with the announcement of the Whipple results) (Tsuchiya et al., 2004). Since CANGAROO-II is located in the Southern-Hemisphere, it has the advantage of observing the Galactic Center for long periods of time at small zenith angles, requiring no special analysis modifications. Their data, taken in 2001 and 2002 with a total on-source observation time of 122 hours, show a point source at the Galactic Center with a soft $E^{-4.6\pm0.5}$ spectrum. Though there is some hint of a flare in 2001, no statistically significant variability was detected. The spectrum, which shows a steep cutoff and little emission above 1 TeV is, however, inconsistent with our results. The most likely explanation

is an error in the CANGAROO analysis, given the disagreement between other CANGAROO and HESS results.

5.1.2 HESS Detection

Several months after our results were made public, HESS, a second-generation Atmospheric Čerenkov Telescope array in Namibia, reported a 9.2σ excess in TeV emission from the direction of the Galactic Center (Aharonian et al., 2004). This detection was made with two telescopes in operation over two two-month periods in which they collected 4.7 and 11.8 hours of on-source data, respectively. In the first observation period, the telescopes were operated independently (and the data combined with off-line software), while in the latter, they operated as an array. The emission is consistent with a point-source located within one arcminute of Sgr A*, and has a power-law flux $F(E) = N_0 E^{-\alpha}$ with $\alpha = 2.12 \pm 0.09$ and $N_0 = (2.50 \pm 0.21) \times 10^{-8}\,\mathrm{m^{-2}\,s^{-1}\,TeV^{-1}}$ (see Figure 4.3). No evidence for variability is seen.

Like CANGAROO, HESS is a Southern-Hemisphere telescope and can see the Galactic Center at small zenith angles for a good portion of a year. Additionally, since HESS is an array-based telescope, each telescope sees the shower from a different viewpoint, allowing very accurate stereo-reconstruction of a shower. This has the advantage of providing drastically better background rejection.

Though the Whipple results presented in this paper are of lower statistical significance, the flux and spectrum from HESS agree well, giving credence to both results. While the HESS detection should be considered the definitive high-confidence con-

firmation of the Galactic Center source, the Whipple results provide one distinct advantage: observations that span a number of seasons, during which we see no evidence for long-term variability. In addition, the large effective area provided by LZA observations provide data at 3-10 TeV of comparable statistical significance to the high-energy HESS spectral points.

5.2 Present Understanding

Very little is known about the source of TeV emission in the Galactic Center. It is possible that three distinct, unidentified gamma-ray sources have been detected in this region: the Whipple/HESS source presented here, which is characterized by a hard spectrum with emission extending well above 3 TeV, the CANGAROO source, which has a soft spectrum and little emission at 3 TeV, and the EGRET GeV source, with a soft spectrum and apparent offset from Sgr A* (Buckley, 2005). Given the relatively low resolution of TeV observations, the emission from the Whipple/HESS source cannot be definitively associated with Sgr A*. However, the emission is unusually bright (with a flux of ~ 0.22Crab at approximately four times the distance to the Crab Nebula), making association with other nearby Galactic objects such as a supernova remnants, pulsars, or stellar mass black holes unlikely. If the emission is produced by the Sgr A East supernova remnant (Khokhlov and Melia, 1996), for example, the GeV flux detected by EGRET would be two orders of magnitude brighter than similar objects (Fatuzzo and Melia, 2003). TeV observations of other nearby galactic X-ray

sources have yielded only upper-limits or non-detections, furthering the possibility that the emission is from a more exotic source.

If the emission is from Sgr A*, and comes from the accretion disc of the supermassive black hole or from a hidden jet, the physical mechanisms for producing gamma-rays is still poorly understood. Though the Jet/ADAF model (see §1.2.1) can be adjusted to give good fits to the lower energy spectra, it does not predict the observed TeV flux or lack of variability. Proton synchrotron models can produce TeV emission, but only with very large magnetic fields ($\sim 10^6$ G), which are well above the accepted value (Aharonian and Neronov, 2005). Pion-decay models can also produce TeV gamma-rays, however the kinematics require a primary gamma-ray energy several times greater than the maximum observed energy, which would be $\gtrsim 30$ TeV given our results. The *black-hole plerion* model (discussed in §1.2.1) currently gives the most promising description, accounting for the lack of variability and for the numerous spectral components comprising the broad multi-wavelength emission.

The lack of TeV variability in light of significant X-ray, NIR, and radio flaring may be an indication that the TeV emission is being produced outside the accretion disc, and is thus less sensitive to changes in the accretion rate (as in the plerion model (Atoyan and Dermer, 2004)). Alternately, proton emission models may produce TeV emission from near the black hole with hour-scale variability, that by chance, have not yet been detected during current observations (Aharonian and Neronov, 2005).

If instead the observed emission is from WIMP dark matter annihilation (also expected to give rise to stead emission from a slightly extended source), then it presents

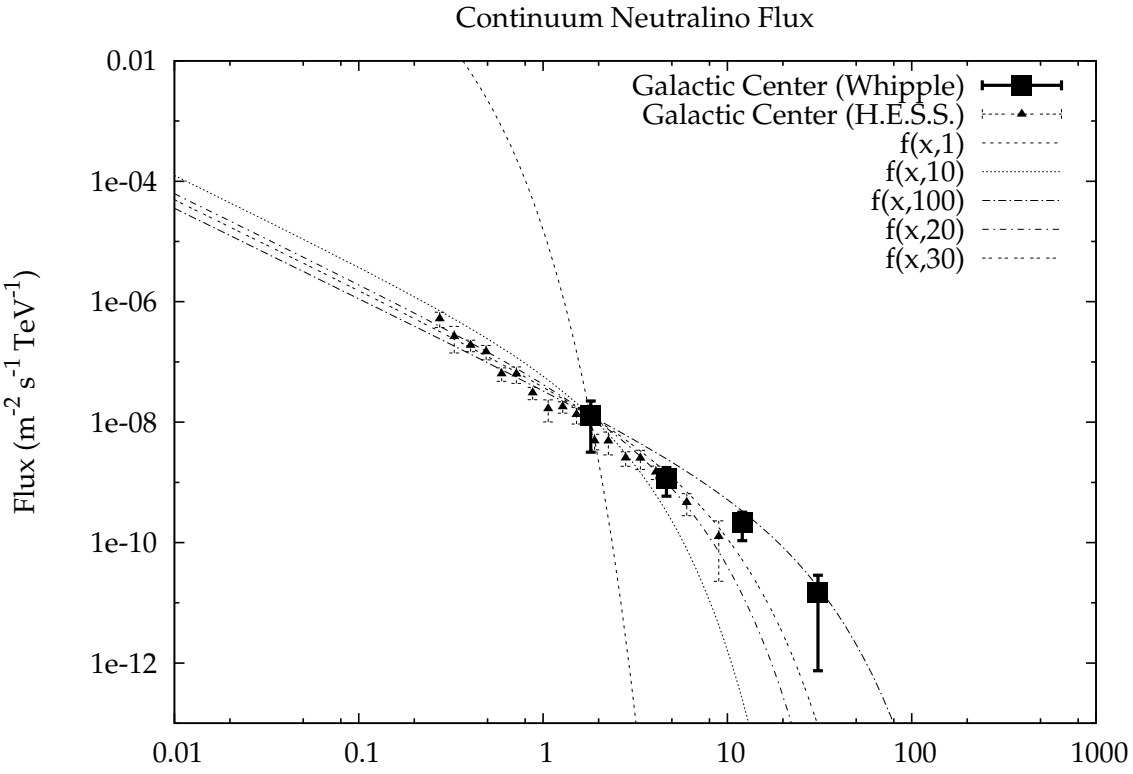

FIGURE 5.1: This plot shows the Whipple and HESS spectral results for the Galactic Center overlaid with a model for the continuum emission from neutralino annihilation (Bergström et al., 1998) for a 1 TeV,10 TeV,100 TeV,20 TeV, and 30 TeV neutralino. This would constrain the mass to be in the range 20 TeV $\lesssim m_\chi \lesssim$ 100 TeV.

some constraints on Neutralino models, and pushes the limits for an acceptable neutralino mass. Since the emission extends up to 10 TeV, the mass of the neutralino would have to be quite large. In Figure 5.1 I have overlaid our spectral results for the Galactic Center with a model of the expected continuum emission flux from neutralino annihilation, $f(E) = N_0(E/m_\chi)^{-1.5}e^{-7.8(E/m_\chi)}$ (Bergström et al., 1998), for several values of the neutralino mass m_χ. This model combined with our data predicts a mass between 20 TeV and 100 TeV. Horns (2004) argues that the HESS spectrum places a lower-limit of $m_\chi \geq 12\,\mathrm{TeV}$ at 90% confidence based on a fit to the theoretical π^0 spectrum. Though the theoretical maximum WIMP mass is as high as 340 TeV from unitarity considerations (Griest and Kamionkowski, 1990) , cosmological constraints can be placed which limit $m_\chi \leq 32$ TeV (Griest et al., 1990), and by some interpretations $\lesssim 600$ GeV (Ellis et al., 2003).

5.3 The Future

Now that the existence of a TeV gamma-ray source at the Galactic Center has been established, there are three primary open questions: How high in energy does the spectrum extend? Is there any evidence of variability? And, finally: Is Sgr A* the source of the emission? To answer these, further observations by next-generation gamma-ray telescopes such as HESS, VERITAS, and MAGIC, combined with GeV observations by the soon-to-be-launched GLAST satellite will be extremely important.

Understanding the extent of the spectrum will constrain astrophysical emission models, put further pressure on the viability of a dark-matter origin, and if spectral features are detected, possibly answer the dark matter question altogether. Though the spectrum measured by the HESS instrument is already quite detailed, large-zenith-angle observations of the source by Northern Hemisphere telescopes can provide higher-energy spectral measurements. The threshold energy of an ACT increases (by a factor of ~ 6) for LZA observations, but the effective area also increases (by a factor of ~ 4), so VERITAS, with a ~ 600 GeV LZA threshold will provide better sensitivity per unit observation time at the high-end of the spectrum (> 3 TeV) than HESS. The combination of small and large zenith-angle observations will give very detailed spectral information for the Galactic Center over a large dynamic range, allowing us to better understand what may be one of the hardest-spectrum and highest-energy gamma-ray sources yet observed.

To answer the variability question, long-term monitoring and higher-sensitivity observations will be required. The GLAST (*Gamma Ray Large Area Space Telescope*) satellite, scheduled to be launched in 2007, will have a wide field of view of $\gtrsim 2.5$ ster, allowing it to monitor the Galactic Center with excellent temporal coverage in an energy range of 20 MeV through 100 GeV. For TeV variability, we must rely on continuing pointed observations by ACTs, which have a much shorter duty cycle. However, given the number of next-generation ACTs in operation or under construction, coordinated campaigns with Southern Hemisphere ACTs (HESS, CANGAROO), combined with LZA observations by VERITAS and MAGIC should

give good temporal and spectral coverage. The Milagro water Čerenkov instrument at Los Alamos may also provide good long-term data, however it is currently not sensitive to resolve the Galactic Center. Coordinated multi-wavelength campaigns with X-ray telescopes will also be necessary to provide further insight into the TeV emission mechanism. Evidence for correlated X-ray/gamma-ray variability, for example, would rule-out plerionic emission and dark matter annihilation.

To determine the exact source of the TeV emission, higher-resolution observations will also be required. ACTs are currently the best instruments for high-resolution TeV astronomy, with angular resolutions on the order of 0.1° or lower. Space-based observatories have very large fields-of-view, but relatively low effective areas and poor angular resolution (due mostly to size restrictions).

Understanding the center of our own galaxy will provide much insight the physics of active galactic nuclei, black-holes, accretion mechanisms, and cosmology. Since the nature of the emission from the Galactic Center is still unknown, more detailed observations and theoretical interpretations of this fascinating region will likely continue into the foreseeable future.

Appendix A

Parameterization Formulae

A.1 Moments of the Light Distribution

$$
\begin{aligned}
S_{\mathrm{tot}} &\equiv SIZE = \sum_i S_i \\
\langle x \rangle &= \frac{1}{S_{\mathrm{tot}}} \sum_i S_i x_i \\
\langle y \rangle &= \frac{1}{S_{\mathrm{tot}}} \sum_i S_i y_i \\
\langle x^2 \rangle &= \frac{1}{S_{\mathrm{tot}}} \sum_i S_i x_i^2 \\
\langle y^2 \rangle &= \frac{1}{S_{\mathrm{tot}}} \sum_i S_i y_i^2 \\
\langle y^2 \rangle &= \frac{1}{S_{\mathrm{tot}}} \sum_i S_i y_i^2 \\
\langle xy \rangle &= \frac{1}{S_{\mathrm{tot}}} \sum_i S_i x_i y_i
\end{aligned}
\tag{A.1}
$$

The sums are made over pixels which pass the *cleaning* threshold only. These moments

are calculated about the origin of the camera. For an offset origin position (o_x, o_y), one can replace $x_i \rightarrow (x_i - o_x)$ and $y_i \rightarrow (y_i - o_y)$.

A.2 Useful Quantities

$$\begin{aligned} \sigma_x^2 &\equiv \left\langle x^2 \right\rangle - \langle x \rangle^2 \\ \sigma_y^2 &\equiv \left\langle y^2 \right\rangle - \langle y \rangle^2 \\ \sigma_{xy}^2 &\equiv \langle xy \rangle - \langle x \rangle \langle y \rangle \end{aligned} \tag{A.2}$$

$$\begin{aligned} d &\equiv \sigma_y^2 - \sigma_x^2 \\ z &\equiv \sqrt{d^2 + 4(\sigma_{xy}^2)^2} \end{aligned} \tag{A.3}$$

A.3 Geometric Parameters

$$\begin{aligned} LENGTH &= \sqrt{\left(\sigma_x^2 + \sigma_y^2 + z\right)/2} \\ WIDTH &= \sqrt{\left(\sigma_x^2 + \sigma_y^2 - z\right)/2} \\ DISTANCE &= \sqrt{\langle x \rangle^2 + \langle y \rangle^2} \\ MISS &= \left[(1 + d/z)\langle x \rangle^2 + (1 - d/z)\langle y \rangle^2\right]/2 \\ &\quad - 2\langle x \rangle \langle y \rangle \sigma_{xy}^2/z \\ ALPHA &= \arcsin\left(\frac{MISS}{DISTANCE}\right) \\ \psi &= \arctan\left(\frac{(d+z)\langle x \rangle + 2\sigma_{xy}^2 \langle x \rangle}{2\sigma_{xy}^2 \langle y \rangle - (d-z)\langle x \rangle}\right) \end{aligned} \tag{A.4}$$

A.3.1 Conversion from WIDTH and LENGTH to ZWIDTH and ZLENGTH

$$ZWIDTH(x,\vartheta) = \left\{ \left[(WIDTH^2 - \sigma^2_{\rm psf} + \sigma^2_{\rm pix})^{\frac{1}{2}} + B(x-C) + E(x-C)^2 + F(x-C)^3 \right]^2 \cdot \right. \\ \left. \cdot \mathcal{Z}(\cos\vartheta) + \sigma^2_{\rm psf} + \sigma^2_{\rm pix} \right\}^{\frac{1}{2}} \quad \text{(A.5)}$$

where, $x = \log SIZE$, and ϑ is the zenith angle and

$$\mathcal{Z}(\cos\vartheta, \cos\vartheta_{\rm fixed}) \equiv \frac{\cos^{\beta}(\vartheta_{\rm fixed})}{cos^{\gamma}(\vartheta_{\rm fixed})} \cdot cos^{\gamma}(\vartheta) \quad \text{(A.6)}$$

Parameter	ZWIDTH	ZLENGTH
A	0.003	0.003
B	0.047 ± 0.063	9.86 ± 2.08
C	9.8 ± 2.0	9.8 ± 2.0
D	0.18 ± 0.09	0.302 ± 0.001
E	0.015 ± 0.015	0.027 ± 0.001
F	0.0025 ± 0.0004	0.0037 ± 0.0002
β	1.5	1.2
γ	0.714 ± 0.02	0.949 ± 0.04

This is discussed in detail in §2.3.2.

A.4 2-D Parameters

The displacement (DISP) of the point or origin from the centroid $(\langle x \rangle, \langle y \rangle)$ is defined as:

$$DISP = \epsilon \left| 1 - \frac{WIDTH}{LENGTH} \right| \quad \text{(A.7)}$$

where ϵ, the *elongation factor*, is a constant (or function of other parameters) derived from simulations (see Section A.4).

Placing this displacement into the correct orientation, the two possible points of origin, **a** and **b** are:

$$\begin{aligned}
\mathbf{a} \equiv \begin{pmatrix} a_x \\ \\ a_y \end{pmatrix} &= \begin{pmatrix} \cos\psi & \sin\psi \\ \\ -\sin\psi & \cos\psi \end{pmatrix} \begin{pmatrix} DISP \\ \\ 0 \end{pmatrix} + \begin{pmatrix} \langle x \rangle \\ \\ \langle y \rangle \end{pmatrix} \\
\mathbf{b} \equiv \begin{pmatrix} b_x \\ \\ b_y \end{pmatrix} &= \begin{pmatrix} \cos\psi & \sin\psi \\ \\ -\sin\psi & \cos\psi \end{pmatrix} \begin{pmatrix} -DISP \\ \\ 0 \end{pmatrix} + \begin{pmatrix} \langle x \rangle \\ \\ \langle y \rangle \end{pmatrix}
\end{aligned} \tag{A.8}$$

In some cases, the correct point of origin can be chosen by looking at the shower *asymmetry* (or skewness) about the centroid. For this, all the moments must be re-calculated about the *centroid* position, not the origin of the camera, and we must define the 3rd order moments and variances:

$$\begin{aligned}
\left\langle x^3 \right\rangle &= \frac{1}{S_{\text{tot}}} \sum_i S_i x_i^3 \\
\left\langle y^3 \right\rangle &= \frac{1}{S_{\text{tot}}} \sum_i S_i y_i^3 \\
\left\langle x^2 y \right\rangle &= \frac{1}{S_{\text{tot}}} \sum_i S_i x_i^2 y_i \\
\left\langle x y^2 \right\rangle &= \frac{1}{S_{\text{tot}}} \sum_i S_i x_i y_i^2
\end{aligned} \tag{A.9}$$

$$
\begin{aligned}
v_{x^3} &= \left\langle x^3 \right\rangle - 3\left\langle x^2 \right\rangle \langle x \rangle + 2\langle x \rangle^3 \\
v_{y^3} &= \left\langle y^3 \right\rangle - 3\left\langle y^2 \right\rangle \langle y \rangle + 2\langle y \rangle^3 \\
v_{x^2y} &= \left\langle x^2 y \right\rangle - 2\langle xy \rangle \langle x \rangle + 2\langle x \rangle^2 \langle y \rangle - \left\langle x^2 \right\rangle \langle y \rangle \\
v_{xy^2} &= \left\langle xy^2 \right\rangle - 2\langle xy \rangle \langle y \rangle + 2\langle x \rangle \langle y \rangle^2 - \langle x \rangle \left\langle y^2 \right\rangle
\end{aligned}
\tag{A.10}
$$

Then, the asymmetry can be defined as:

$$
ASYM = v_{x^3}\cos^3\psi + 3v_{x^2y}\cos^2\psi\sin\psi + 3v_{xy^2}\cos\psi\sin^2\psi + v_{y^3}\sin^3\psi \tag{A.11}
$$

Appendix B

Gamma Ray Analysis Statistics

If N_{on} is the number of counts observed in an on-source observation, N_{off} is the number of counts observed off-source, and α is the ratio of integration times between on and off ($\alpha = t_{on}/t_{off}$), then the number of background photons is:

$$N_B = \alpha N_{off} \tag{B.1}$$

and the number of source photons (also called the gamma-ray *excess*) is,

$$N_S = N_{on} - N_B = N_{on} - \alpha N_{off} \tag{B.2}$$

Using Poisson statistics, the statistical *significance*, S, can be written in its simplest form as the ratio of signal counts above background to the standard deviation as:

$$S = \frac{N_S}{\hat{\sigma}(N_S)} = \frac{N_{on} - N_{off}}{\sqrt{\alpha(N_{on} + N_{off})}} \tag{B.3}$$

This form is derived and discussed in detail by Li and Ma (1983). A more accurate form of the significance, using a maximum-likelihood argument based on the null

hypothesis that all observed photons are due to background ($\langle N_s \rangle = 0$), is given by:

$$S = \sqrt{2} \left\{ N_{on} \ln \left[\frac{1+\alpha}{\alpha} \left(\frac{N_{on}}{N_{on}+N_{off}} \right) \right] + N_{off} \ln \left[(1+\alpha) \left(\frac{N_{off}}{N_{on}+N_{off}} \right) \right] \right\}^{1/2} \tag{B.4}$$

Formula B.4 was used for calculating the significance of results presented in this dissertation.

Appendix C

Detailed Galactic Center Results

TABLE C.1: All data runs taken of the Galactic Center region since 1995.

ON	OFF	N2	UT Date	Elevation (°)
gt002591	gt002590	gt002583	1995-06-24	28.98
gt002705	gt002704	gt002702	1995-07-04	28.57
gt002831	gt002830	gt002829	1995-07-28	29
gt005520	gt005519	gt005515	1996-06-20	29.19
gt005539	gt005538	gt005537	1996-06-23	28.54
gt005619	gt005618	gt005629	1996-07-18	29.22
gt008610	gt008609	gt008613	1997-06-02	27.16
gt008659	gt008658	gt008647	1997-06-05	28.75
gt008695	gt008694	gt008690	1997-06-09	28.7
gt008711	gt008710	gt008708	1997-06-11	29.21
gt014971	gt014970	gt014954	2000-04-05	27.59
gt015132	gt015131	gt015119	2000-04-29	27.25
gt015181	gt015180	gt015168	2000-05-02	28.63
gt015234	gt015233	gt015220	2000-05-05	29.13
gt015337	gt015336	gt015328	2000-05-26	27.79
gt015433	gt015432	gt015428	2000-06-04	22.18
gt015437	gt015436	gt015428	2000-06-04	29.2
gt015447	gt015446	gt015443	2000-06-05	28.13
gt015460	gt015459	gt015454	2000-06-06	29.16
gt015507	gt015506	gt015502	2000-06-26	28.6
gt015526	gt015525	gt015519	2000-07-04	28.9
gt015538	gt015537	gt015534	2000-07-05	28.32

Continued on next page...

Table C.1: (continued)

ON	OFF	N2	UT Date	Elevation (°)
gt017937	gt017936	gt017929	2001-05-23	25.97
gt017940	gt017939	gt017929	2001-05-23	29.17
gt017942	gt017941	gt017929	2001-05-23	26.98
gt017954	gt017953	gt017944	2001-05-24	28.66
gt017958	gt017957	gt017944	2001-05-24	28.11
gt018032	gt018031	gt018022	2001-06-13	28.29
gt018046	gt018045	gt018034	2001-06-14	28.72
gt018059	gt018058	gt018050	2001-06-15	28.89
gt022052	gt022051	gt022042	2002-05-06	27.69
gt022135	gt022134	gt022124	2002-05-11	29.18
gt022192	gt022191	gt022181	2002-05-14	28.48
gt022206	gt022205	gt022196	2002-05-15	29.05
gt022461	gt022460	gt022449	2002-06-11	23.83
gt022499	gt022498	gt022494	2002-06-14	28.15
gt022509	gt022508	gt022504	2002-06-15	28.62
gt022520	gt022519	gt022515	2002-06-16	28.48
gt024534	gt024533	gt024519	2003-04-28	28.29
gt024603	gt024602	gt024587	2003-05-02	29.01
gt024623	gt024622	gt024607	2003-05-03	28.65
gt024648	gt024647	gt024638	2003-05-05	29.11
gt024672	gt024671	gt024663	2003-05-07	28.24
gt024847	gt024846	gt024839	2003-06-03	29.09
gt024863	gt024862	gt024855	2003-06-04	27.97
gt024882	gt024881	gt024879	2003-06-06	29.21
gt024884	gt024883	gt024879	2003-06-06	27.34
gt024894	gt024893	gt024892	2003-06-07	28.16
gt024903	gt024902	gt024901	2003-06-08	27.29
gt024927	gt024926	gt024921	2003-06-21	29.17
gt024946	gt024945	gt024939	2003-06-23	29.2
gt024955	gt024954	gt024939	2003-06-24	28.8
gt025108	gt025107	gt025106	2003-07-05	27.88
gt027050	gt027049	gt027037	2004-05-12	28.11
gt027063	gt027062	gt027051	2004-05-13	28.48
gt027077	gt027076	gt027065	2004-05-14	26.73
gt027109	gt027108	gt027099	2004-05-16	24.75
gt027129	gt027128	gt027118	2004-05-17	28.02
gt027146	gt027145	gt027135	2004-05-18	26.25
gt027166	gt027165	gt027154	2004-05-19	28.68

Continued on next page...

TABLE C.1: (continued)

ON	OFF	N2	UT Date	Elevation (°)
gt027256	gt027255	gt027249	2004-06-08	26.76
gt027266	gt027265	gt027257	2004-06-09	28.16
gt027335	gt027334	gt027329	2004-06-15	27.51
gt027367	gt027366	gt027361	2004-06-17	27.93
gt027382	gt027381	gt027376	2004-06-18	28.02
gt027398	gt027397	gt027392	2004-06-19	28.36
gt027412	gt027411	gt027407	2004-06-20	28.58
gt027425	gt027424	gt027422	2004-06-22	29.11

TABLE C.2: Events Passing Cuts for each run. The number of events remaining after each set of cuts is shown. The "trigger" cuts are MAX1,MAX2 and SIZE, the "shape" cuts are LENGTH,WIDTH,MISS,and DISTANCE, and the "orientation" cut is the ALPHA cut (which was not applied in the Galactic Center 2D analysis, but is shown here for completeness). The last column (off-alpha) is the number of counts passing the Trigger and Shape cuts which have an ALPHA value in the range $20° - 65°$ and is a measure of the number of background gamma-ray events.

Run ID	**Total**	**Trigger**	**Shape**	**Orientation**	**off-alpha**
gt002591	13243	6040	614	96	310
gt002590	13901	6270	663	101	327
gt002705	14581	6498	741	120	346
gt002704	15193	6660	744	130	355
gt002831	9049	3867	466	75	257
gt002830	9375	3942	420	51	204
gt005520	11815	4950	522	87	263
gt005519	12073	5044	536	89	262
gt005539	14905	6374	630	107	311
gt005538	14785	6323	575	73	306
gt005619	14056	6004	540	80	266
gt005618	14425	6003	498	72	248
gt008610	12492	7935	710	116	331
gt008609	12745	7956	697	113	339
gt008659	11745	7193	554	92	274
gt008658	11761	7002	633	98	324
gt008695	12385	7825	714	122	352
gt008694	12649	8059	651	103	336
gt008703	13489	8558	779	119	386

Continued on next page...

TABLE C.2: (continued)

Run ID	Total	Trigger	Shape	Orientation	off-alpha
gt008702	14120	8905	794	141	399
gt008711	13105	8247	838	144	387
gt008710	13225	8097	787	129	395
gt014971	16875	4595	781	138	396
gt014970	18504	4566	757	129	375
gt015047	14030	3590	714	119	337
gt015046	13355	3629	816	109	391
gt015132	18829	5154	859	140	457
gt015131	18875	5136	820	144	407
gt015181	18475	5568	1188	162	623
gt015180	18064	5529	1199	168	625
gt015234	16810	4265	984	160	472
gt015233	16903	4182	911	132	446
gt015337	16830	4663	944	179	478
gt015336	17138	4730	894	141	481
gt015433	12777	3295	392	62	209
gt015432	13015	3334	403	71	186
gt015437	18858	5545	1364	218	661
gt015436	18801	5667	1378	212	655
gt015447	15508	4702	971	164	519
gt015446	15450	4475	877	127	453
gt015460	15517	4158	930	140	462
gt015459	15367	4090	894	156	411
gt015507	16538	4210	858	142	434
gt015506	15987	3877	787	134	368
gt015526	18317	5491	1213	192	598
gt015525	18551	5661	1168	194	568
gt015538	18040	5266	1104	178	560
gt015537	17930	5254	1033	169	498
gt017937	25105	4493	603	101	306
gt017936	24846	4377	557	94	288
gt017940	27904	5404	999	148	500
gt017939	28361	5499	1034	167	539
gt017942	25120	4675	630	127	321
gt017941	25228	4743	641	121	326
gt017954	27433	5369	954	153	474
gt017953	26676	5240	935	136	477
gt017958	26747	5135	860	141	421
gt017957	26312	5115	852	126	441

Continued on next page...

TABLE C.2: (continued)

Run ID	Total	Trigger	Shape	Orientation	off-alpha
gt018032	31098	5915	1307	223	663
gt018031	31707	6062	1285	224	671
gt018046	34128	5451	1290	239	636
gt018045	37352	5641	1337	218	683
gt018059	25269	4985	975	157	488
gt018058	25967	5163	1007	147	499
gt022052	20627	4134	722	122	379
gt022051	25468	4339	798	134	422
gt022135	20730	5038	956	146	462
gt022134	22100	4949	928	136	452
gt022192	16478	3769	558	95	265
gt022191	14462	3550	551	94	281
gt022206	18806	4644	814	155	395
gt022205	21126	4851	895	131	442
gt022461	10579	2730	282	55	138
gt022460	10893	2775	278	67	122
gt022499	11853	3344	569	94	284
gt022498	12039	3457	655	94	352
gt022509	13133	3525	689	99	332
gt022508	13300	3505	654	109	328
gt022520	15050	4224	951	146	507
gt022519	15848	4191	848	130	454
gt024534	14680	3179	381	82	173
gt024533	13544	3035	382	60	193
gt024603	14887	3384	527	69	270
gt024602	14505	3572	560	93	270
gt024623	14442	3457	589	100	288
gt024622	15789	3543	556	95	283
gt024648	16309	3779	563	91	279
gt024647	15498	3729	319	62	155
gt024672	13661	3545	558	101	287
gt024671	13846	3474	520	69	257
gt024847	15491	2853	473	76	244
gt024846	10850	2550	417	57	206
gt024863	10550	2297	323	59	156
gt024862	10748	2259	301	50	155
gt024882	15120	3132	440	58	228
gt024881	11895	3123	431	62	205
gt024884	10297	2530	261	47	145

Continued on next page...

TABLE C.2: (continued)

Run ID	**Total**	**Trigger**	**Shape**	**Orientation**	**off-alpha**
gt024883	10442	2591	267	41	149
gt024894	10914	2829	339	60	172
gt024893	9754	2585	323	53	161
gt024903	10600	2625	351	67	178
gt024902	10311	2432	292	54	158
gt024927	13684	3303	505	84	248
gt024926	14853	3266	516	74	267
gt024946	11173	3379	476	82	241
gt024945	11046	3385	454	85	230
gt024955	11581	3511	478	83	237
gt024954	11762	3497	470	63	240
gt025108	6123	1664	256	40	125
gt025107	6110	1627	217	31	111

1-D Analysis by run.

TABLE C.3: Statistics for each run pair in the Galactic Center dataset

ON	OFF	Excess	Significance
gt002591	gt002590	-5.02	-0.35
gt002705	gt002704	-10.08	-0.63
gt002831	gt002830	23.97	2.14
gt005520	gt005519	-2.34	-0.17
gt005539	gt005538	34.08	2.55
gt005619	gt005618	7.808	0.63
gt008610	gt008609	2.503	0.16
gt008659	gt008658	-6.57	-0.47
gt008695	gt008694	19.07	1.27
gt008703	gt008702	-21.76	-1.35
gt008711	gt008710	14.84	0.89
gt014971	gt014970	8.94	0.54
gt015047	gt015046	9.86	0.65
gt015132	gt015131	-4.14	-0.24
gt015181	gt015180	-5.97	-0.32
gt015234	gt015233	28.01	1.64
gt015337	gt015336	37.86	2.11

continued on next page...

Table C.3: (continued)

ON	OFF	Excess	Significance
gt015433	gt015432	-8.99	-0.78
gt015437	gt015436	6.00	0.28
gt015447	gt015446	37.11	2.17
gt015460	gt015459	-16.04	-0.93
gt015507	gt015506	7.99	0.48
gt015526	gt015525	-1.83	-0.09
gt015538	gt015537	9.07	0.48
gt017937	gt017936	7.13	0.51
gt017940	gt017939	-19.03	-1.07
gt017942	gt017941	6.12	0.38
gt017954	gt017953	16.99	0.99
gt017958	gt017957	15.09	0.92
gt018032	gt018031	-0.73	-0.03
gt018046	gt018045	21.18	0.99
gt018059	gt018058	10.03	0.57
gt022052	gt022051	-12.04	-0.75
gt022135	gt022134	10.02	0.59
gt022192	gt022191	1.02	0.07
gt022206	gt022205	24.01	1.42
gt022461	gt022460	-11.98	-1.08
gt022499	gt022498	-0.02	-0.00
gt022509	gt022508	-9.94	-0.68
gt022520	gt022519	16.08	0.96
gt024534	gt024533	21.97	1.84
gt024603	gt024602	-24.04	-1.88
gt024623	gt024622	4.94	0.35
gt024648	gt024647	28.94	2.34
gt024672	gt024671	31.99	2.46
gt024847	gt024846	13.24	1.09
gt024863	gt024862	9.00	0.86
gt024882	gt024881	-4.05	-0.37
gt024884	gt024883	5.98	0.63
gt024894	gt024893	7.02	0.66
gt024903	gt024902	13.03	1.18
gt024927	gt024926	10.05	0.79
gt024946	gt024945	-3.00	-0.23
gt024955	gt024954	20.00	1.65
gt025108	gt025107	9.01	1.07

Appendix D

Code for Various Algorithms

The following are pieces of source-code from the `WUparam` analysis package developed for analyzing the data presented in this thesis.

D.1 Sky Brightness Map

Do a pointing check using the pedestal variances. Generates a 2-D grid that matches the grid used by the Cutter for the 2-D significance/excess plots which contains the sky brightness at each point in RA/DEC space. Also generates a 2-D "tubeoffness" map of PMT's that were turned off due to extrememe pedestal variances.

onpeds on-source Pedestal array

offpeds off-source Pedestal array

grid 2D array of doubles where the brightnesses should be stored.

header the RawHeaderRecord for the run (specifying RA and DEC)

avg_gpstime the average gps time of the run.

```
void
Parameterizer::
mapSkyBrightness( const string &id, const vector<Pedestal> &onpeds,
                  const vector<Pedestal> &offpeds, const Array_t &gain,
                  const RawHeaderRecord &header, double avg_gpstime,
```

```
                bool derotation) {

const double DEGPERPIX=0.1; // degrees per pixel (assuming square pixels)
const double SIGR2 = 0.02;  // something like the RMS^2 of the PSF

Image2D brightmap(39,39);
Image2D tubeoffmap(39,39);

Array_t xcoord, ycoord;
Array_t pedvardiff;
Coord_t coord;
int i,j,k;
double sky_brightness, tubeoffness;
double r2, gauss_weight;
int nxbins = brightmap.getXDim();
int nybins = brightmap.getYDim();

// calculate the correct derotation angle (theta)

updateAngles( avg_gpstime, header );

// precalculate the pedestal variance difference (yes, variances
// not dispersions)

pedvardiff.resize(onpeds.size());
for (i=0; i<onpeds.size(); i++) {

    if ( (onpeds[i].type == Pedestal::TUBEOFF ||
          offpeds[i].type == Pedestal::TUBEOFF)
         ||
         (onpeds[i].type == Pedestal::STAR &&
          offpeds[i].type == Pedestal::STAR)) {

        pedvardiff[i] = 0;

    }
    else {
        pedvardiff[i] = pow(onpeds[i].dispersion,2)
            - pow(offpeds[i].dispersion,2);
    }

}

// Get the camera coordinates and derotate them into tangential coords!

xcoord.resize(_cam->xCoords().size());
ycoord.resize(_cam->yCoords().size());
xcoord = _cam->xCoords();
ycoord = _cam->yCoords();

if (derotation == true) {
    for (i=0; i<(int)xcoord.size(); i++) {
        coord.x = xcoord[i];
        coord.y = ycoord[i];
        derotatePoint( _theta, coord );
        xcoord[i] = coord.x;
        ycoord[i] = coord.y;
    }
}

// Set up the coordinate grid:

brightmap.setCoordinateBox( -nxbins*DEGPERPIX/2.0,-nybins*DEGPERPIX/2.0,
                            nxbins*DEGPERPIX/2.0,nybins*DEGPERPIX/2.0);
tubeoffmap.setCoordinateBox( -nxbins*DEGPERPIX/2.0,-nybins*DEGPERPIX/2.0,
                             nxbins*DEGPERPIX/2.0,nybins*DEGPERPIX/2.0);

// Accumulate the sky brightness and tubeoffness:

for (i=0; i<nxbins; i++) {
    for (j=0; j<nybins; j++) {

        sky_brightness = 0;
        tubeoffness = 0;

        for (k=0; k<(int)xcoord.size(); k++) {

            // tube is ON or contains a star in the ON
            // run, or just good in the OFF, so update sky
            // brightness map

            r2 = (pow(xcoord[k] - brightmap.getXCoord(i),2) +
                  pow(ycoord[k] - brightmap.getYCoord(j),2));
            gauss_weight = exp(-r2/SIGR2);
            sky_brightness += pedvardiff[k]*gauss_weight
                *pow(gain[k],2); // flat field


            if ((onpeds[k].type == Pedestal::TUBEOFF) ||
```

```
                    (offpeds[k].type == Pedestal::TUBEOFF) ||
                    (onpeds[k].type == Pedestal::STAR) ||
                    (offpeds[k].type == Pedestal::STAR)) {

                    // tube is OFF, so update tubeoffness map
                    r2 = (pow(xcoord[k] - tubeoffmap.getXCoord(i),2) +
                          pow(ycoord[k] - tubeoffmap.getYCoord(j),2));
                    gauss_weight = exp(-r2/SIGR2);
                    tubeoffness  += 1.0*gauss_weight;

                }

            }


            brightmap.addToPixel(i,j, sky_brightness);
            tubeoffmap.addToPixel( i,j, tubeoffness );

        }
    }

    // save the maps...

    brightmap.save( id+"/"+id+"-sky_brightness" );
    tubeoffmap.save( id+"/"+id+"-tubeoffness" );

}
```

D.2 Image Parameterization

This function parameterizes an image and calculate the 2D points of origin for gamma-ray showers. The Hillas parameter calculations made here are fairly standard, and should be essentially identical in all Whipple analysis software.

image array of pmt values for the image you want to parameterize

param cleanpixels is a list of the indices of the picture/boundary tubes which pass the cleaning process

The arrays `_x, _y` are precalculated arrays of coordinates of the pixel positions in the camera.

```
void
HillasImageAnalyzer::
parameterize(const Array_t &image, vector<int> &cleanpixels){

    register int i;
    vector<int>::iterator iter;
    double totalsignal=0;
    double momx=0,momy=0, momx2=0, momy2=0, momxy=0, momx3=0, momy3=0;
    double momx2y=0, momxy2=0;
    double vx2, vy2, vxy, vx3, vy3, vx2y, vxy2;
    double d,z, tanpsi_numerator, tanpsi_denominator, sinalpha, azwidth2,z2;
    double cospsi, sinpsi;
    double disp;
    Coordinate_t pa,pb,tempcoord;
    double tmp;
    double u,v;
    double apsi;
    Array_t qx, qy;

    _param.invalid = 0;

    //=========================================================================
    // Get total signal (sum over picture and boundary)

    _param.pixels_in_picture = 0;

    for (iter=cleanpixels.begin(); iter != cleanpixels.end(); iter++) {
        totalsignal += image[*iter];
        _param.pixels_in_picture++;
    }

    _param.size = totalsignal;
```

```
if (totalsignal < EPSILON) {
    clearParam(_param);
    _param.invalid=1;
    return;
}

//=====================================================================
// Calculate moments <x>,<y>,<x^2>,<y^2>,<xy> and use values
// precalculated in the constructor to minimize multiplies.  Third
// order moments are calculated later, when the the asymmetry
// calculation is done (since they myst be centered on the point
// of origin, not the camera origin)

for (iter=cleanpixels.begin(); iter != cleanpixels.end(); iter++) {
    momx    += image[*iter] * _x[*iter]  ;
    momy    += image[*iter] * _y[*iter];
    momx2   += image[*iter] * _x2[*iter];
    momy2   += image[*iter] * _y2[*iter];
    momxy   += image[*iter] * _xy[*iter];
}

momx   /= totalsignal;
momy   /= totalsignal;
momx2  /= totalsignal;
momy2  /= totalsignal;
momxy  /= totalsignal;

//=====================================================================
// Calculate variances (sigma = sqrt(variance))

vx2  = (momx2 - momx*momx);       // <x^2> - <x>^2
vy2  = (momy2 - momy*momy);       // <y^2> - <y>^2
vxy  = (momxy - momx*momy);       // <xy> - <x><y>

//=====================================================================
// Calculate some common factors...

d = vy2 - vx2;

z2 = d*d + 4.0*vxy*vxy;
if (z2>0)
    z = sqrt(z2) ;
else {
    z = 0.0;
    _param.invalid++;
}

//=====================================================================
// Calculate Centroid

_param.centroid.x = momx;
_param.centroid.y = momy;

//=====================================================================
// Calculate width and length

tmp  = (vx2 + vy2 - z )/2.0;
if (tmp>0) _param.width = sqrt(tmp);
else {_param.width = 0.0; _param.invalid++;}

tmp = ( vx2 + vy2 + z )/2.0;
if (tmp>0) _param.length = sqrt(tmp);
else {_param.length=0.0; _param.invalid++;}

//=====================================================================
// Calculate length over size

_param.length_over_size = _param.length / _param.size;

//=====================================================================
// Calculate distance

_param.distance = gsl_hypot(momx, momy);

//=====================================================================
// Calculate miss

if (z > 0.0) {

    u = 1.0+d/z;
    v = 2.0-u;

    tmp = (u*momx*momx + v*momy*momy)/2.0 - momx*momy*2.0*vxy/z;
    if(tmp>0.0) _param.miss = sqrt(tmp);
    else { _param.miss=0; } // don't want small miss to be invalid here
}
else {
    _param.miss = _param.distance;
```

```
}

//=============================================================================
// Calculate azwidth

azwidth2 = (momx2 + momy2 - z);
if (azwidth2>0.0) _param.azwidth = sqrt(azwidth2);
else {_param.azwidth=0.0; _param.invalid++;}

//=============================================================================
// Calculate psi angle

tanpsi_numerator = (d+z)*momy + 2.0*vxy*momx;
tanpsi_denominator = (2*vxy*momy) - (d-z)*momx;

if (tanpsi_numerator > 1.0)
    tanpsi_numerator = 1.0;
else if (tanpsi_numerator<-1.0)
    tanpsi_numerator = -1.0;
if (tanpsi_denominator > 1.0)
    tanpsi_denominator = 1.0;
else if (tanpsi_denominator<-1.0)
    tanpsi_denominator = -1.0;

if (fabs(tanpsi_denominator) > EPSILON )
    _param.psi = atan2( tanpsi_numerator, tanpsi_denominator );
else {
    _param.psi = M_PI_2;
    _param.invalid++;
}

//    _param.psi = gsl_sf_angle_restrict_pos(_param.psi);

//=============================================================================
// Calculate alpha angle

sinalpha = _param.miss/_param.distance;
if (-1.0 <= sinalpha && sinalpha <= 1.0)
    _param.alpha = asin( sinalpha );
else {
    _param.alpha = (sinalpha >=1)? LARGE : -LARGE;
    _param.invalid++;
}

//=============================================================================
// Calculate phi angle (centroid polar angle)

_param.phi = atan2( _param.centroid.y, _param.centroid.x );
_param.phi = gsl_sf_angle_restrict_pos( _param.phi );

//=============================================================================
// Obtain the max adc values...

for (i=0; i<3; i++) {
    _param.max[i] = 0.0;
    _param.index_of_max[i] = 0;
}

for (iter=cleanpixels.begin(); iter != cleanpixels.end(); iter++) {

    if ( image[*iter] > _param.max[2] ){
        if ( image[*iter] > _param.max[1] ){
            if ( image[*iter] > _param.max[0] ){
                _param.max[2] = _param.max[1];
                _param.max[1] = _param.max[0];
                _param.max[0] = image[*iter];
                _param.index_of_max[2] = _param.index_of_max[1];
                _param.index_of_max[1] = _param.index_of_max[0];
                _param.index_of_max[0] = *iter;
            }
            else {
                _param.max[2] = _param.max[1];
                _param.max[1] = image[*iter];
                _param.index_of_max[2] = _param.index_of_max[1];
                _param.index_of_max[1] = *iter;
            }
        }
        else {
                _param.max[2] = image[*iter];
                _param.index_of_max[2] = *iter;
        }
    }
}

//=============================================================================
// Obtain frac[3] values

_param.frac[0] = _param.max[0]/totalsignal;
_param.frac[1] = _param.frac[0] + _param.max[1]/totalsignal;
```

```
_param.frac[2] = _param.frac[1] + _param.max[2]/totalsignal;

//=========================================================================
// 2-D analysis

_param.asymmetry = 0;

if ( _2d_is_enabled ) {

    // ---------------------------------------------------------
    // Calculate 2 possible Points of Origin

    cospsi = cos( -_param.psi );
    sinpsi = sin( -_param.psi );

    // First calculate the displacement along the major-axis of the
    // point of origin (don't know whether it is plus or minus)


    if (_param.length > EPSILON) {
        disp = fabs( _elongation - _elongation *
                    _param.width/_param.length );
    }
    else {
        disp = -LARGE;
    }

    // the points of origin in this frame are given by
    // x' = x +/= disp, y' = y

    pa.x = -disp;
    pb.x = disp;
    pa.y = 0.0;
    pb.y = 0.0;

    // now put into correct orientation by rotating by psi
    // and then translating to the centroid

    if (fabs(_param.psi) > EPSILON ) {
        _param.point_of_origin_a.x = pa.x * cospsi + pa.y*sinpsi;
        _param.point_of_origin_a.y = -pa.x * sinpsi + pa.y*cospsi;
        _param.point_of_origin_b.x = pb.x * cospsi + pb.y*sinpsi;
        _param.point_of_origin_b.y = -pb.x * sinpsi + pb.y*cospsi;
    }
    else {
        _param.point_of_origin_a.x = pa.x;
        _param.point_of_origin_a.y = pa.y;
        _param.point_of_origin_b.x = pb.x;
        _param.point_of_origin_b.y = pb.y;
    }

    _param.point_of_origin_a.x += _param.centroid.x;
    _param.point_of_origin_a.y += _param.centroid.y;
    _param.point_of_origin_b.x += _param.centroid.x;
    _param.point_of_origin_b.y += _param.centroid.y;

    // ---------------------------------------------------------
    // Now, we need to know which of the two points is the correct
    // one, so calculate the Asymmetry about one of the points.
    // Put the favored point in "a" and the reject in "b"

    // For the asymmetry calculation, we need to calculate vx3,
    // vx2y, vxy2, vy3 centered around one of the possible points
    // of origin (not about the camera center). That means
    // recalculating all the moments about the new origin.  I
    // don't use the precalculated arrays (_x, _y, etc.) since
    // it's pointless to recalculate ALL the pixels, just the ones
    // in the image. The precalculated arrays are still useful for
    // the next event, so they shouldn't be modified.

    double x,y;
    int sign;
    momx=0; momy=0; momx2=0; momy2=0; momxy=0;
    momx3=0; momy3=0; momx2y=0; momxy2=0;

    for (iter=cleanpixels.begin(); iter != cleanpixels.end(); iter++) {
        x = _x[*iter]-_param.point_of_origin_a.x;
        y = _y[*iter]-_param.point_of_origin_a.y;
        momx    += image[*iter] * x;
        momy    += image[*iter] * y;
        momx2   += image[*iter] * x*x;
        momy2   += image[*iter] * y*y;
        momxy   += image[*iter] * x*y;
        momx3   += image[*iter] * x*x*x;
        momy3   += image[*iter] * y*y*y;
        momx2y  += image[*iter] * x*x*y;
        momxy2  += image[*iter] * x*y*y;
    }
```

```
        momx   /= totalsignal;
        momy   /= totalsignal;
        momx2  /= totalsignal;
        momy2  /= totalsignal;
        momxy  /= totalsignal;
        momx3  /= totalsignal;
        momy3  /= totalsignal;
        momx2y /= totalsignal;
        momxy2 /= totalsignal;

        vx3  = (momx3  - 3*momx2*momx + 2*momx*momx*momx);
        vy3  = (momy3  - 3*momy2*momy + 2*momy*momy*momy);
        vx2y = (momx2y - 2*momxy*momx + 2*momx*momx*momy - momx2*momy);
        vxy2 = (momxy2 - 2*momxy*momy + 2*momx*momy*momy - momx*momy2);

        // Recalculate psi angle from the new point:
        // Really, the angle should be the same as for the origin, but
        // the sign may be incorrect (since the quandrants are different)

        tanpsi_numerator = (d+z)*momy + 2.0*vxy*momx;
        tanpsi_denominator = (2*vxy*momy) - (d-z)*momx;
        apsi = atan2( tanpsi_numerator, tanpsi_denominator );
        cospsi = cos(apsi);
        sinpsi = sin(apsi);

        // Now calculate the asymmetry

        tmp = ( vx3*pow(cospsi,3) + 3*vx2y*cospsi*cospsi*sinpsi
                + 3*vxy2*cospsi*sinpsi*sinpsi + vy3*pow(sinpsi,3) );

        // NOTE: unlike quicklook, assymmetry is an absolute value for
        // the correct point of origin (which is always "a")
        // A negative sign just means a swap occured

        tmp = tmp/pow(_param.length,3);
        sign = GSL_SIGN(tmp);
        _param.asymmetry = sign*pow(fabs(tmp), 0.3333333);

        // Swap points of origin if asymmetry is negative, so "a"
        // always contains the correct point of origin

        if (sign == -1 ) {
            tempcoord = _param.point_of_origin_a;
            _param.point_of_origin_a = _param.point_of_origin_b;
            _param.point_of_origin_b = tempcoord;
        }

    }

}
```

D.3 EZCut Parameter Corrections

Convert a set of standard Hillas parameters into EZCuts "Z" parameters, which are corrected for zenith angle and camera gain factor.

```
void
EZCutter::
applyCorrections(HillasParameterization &param) {

    double dx,dy, cfact;

    // constants from fits to simulated data. The functional form for
    // width and length is as follows:
    //
    // f(f',x) = [( sqrt(f'^2-A^2) + B(x-C) + E(x-C)^2 + F(x-C)^3)^2 *
    // (cos(60)^COSPOW)/(cos(60)^\gamma) * cos(zenith)^\gamma +
    // A]^(1/2) where x is the log(size) and f' is the zwidth or
    // zlength value.  The function has to be inverted to convert from
    // width -> zwidth.  D is the fitted mean f' value from simulations.

    const double WA = 0.003;
    const double WB = 0.04679;
    const double WC = 9.866;
    const double WD = 0.1832;
    const double WE = 0.01534;
    const double WF = 0.00248;
    const double WGAMMA = 0.949;
    const double WCOSPOW = 1.5;

    const double LA = 0.003;
    const double LB = 0.0792;
```

```
const double LC = 9.867;
const double LD = 0.3023;
const double LE = 0.02700;
const double LF = 0.00374;
const double LGAMMA = 0.714;
const double LCOSPOW = 1.2;

double zen;

HillasParameterization oldparam = param; //for debugging
zen = param.zenith;

//=============================================================
// First, apply camera gain correction (PE/DC)
//=============================================================

// l/s must be corrected after PE to DC correction, but before
// zenith angle

param.max[0] *= _cam->getPEToDC();
param.max[1] *= _cam->getPEToDC();
param.max[2] *= _cam->getPEToDC();
param.size   *= _cam->getPEToDC();
param.length_over_size = (param.length/(double)(param.size));

//=============================================================
// Calculate ezwidth , ezlength
//=============================================================

const double cos60 = cos(60.0*M_PI/180.0);
double ezwidth2, ezlength2;
double ezwidth, ezlength, wzenithfactor,lzenithfactor;
double x,wshift2,lshift2,lterm1,wterm1;

wzenithfactor = ( (pow(cos60, WGAMMA)/pow(cos60,WCOSPOW))
                        /pow( cos(zen), WGAMMA ));

lzenithfactor = ( (pow(cos60, LGAMMA)/pow(cos60,LCOSPOW))
                         /pow( cos(zen), LGAMMA ));
x=log(param.size/0.4489); // need to divide out .4489 since fit
                          // values assume 490 camera with no
                          // corrections


wshift2 = param.width*param.width - WA;
wterm1 = (wshift2*wzenithfactor>1e-20)?
    sqrt(wshift2*wzenithfactor): 1e-20;

ezwidth2 = WA + pow( wterm1 - WB*(x-WC) - WE*pow(x-WC,2)
                        - WF*pow(x-WC,3) ,2 );
ezwidth = (ezwidth2>0.0)? sqrt(ezwidth2) : 0.0;

// ---- zlength

lshift2 = param.length*param.length - LA;
lterm1 = (lshift2*lzenithfactor>1e-20)?
    sqrt(lshift2*lzenithfactor) :1e-20;

ezlength2 = LA + pow( lterm1 - LB*(x-LC) - LE*pow(x-LC,2)
                          - LF*pow(x-LC,3) ,2 );

ezlength = (ezlength2>0.0)? sqrt(ezlength2) : 0.0;

//=============================================================
// Correct the 2D points
//=============================================================

double newelongation;

// First calculate the distance between the point of origin and
// centroid

dx = param.point_of_origin_a.x - param.centroid.x;
dy = param.point_of_origin_a.y - param.centroid.y;

// Now calculate the correction factor including two terms: the
// first ratio corrects the elongation factor, the second replaces
// the width/length (elongation) dependence with the intrinsic
// elongation given by zwidth/zlength

// KPK: the elongation factor is now a function of x=ln(size), fit
// from simulations.  e(x) = 1.0894 + 0.092611*x.  Here x
// shouldn't be divided by 0.4489 because the correction factor
// was already applied in the simulations!

x = log(param.size);
newelongation = 1.0894 + 0.092611*x;

// correct the old point of origin based on the new elongation factor:
```

```
    // the Parameterizer always assumes a elongation factor of 1.68.

    cfact = (newelongation / 1.68) *  // TODO: 1.68 shouldn't be hardcoded!
        ((1.0-ezwidth/ezlength)/(1.0-param.width/param.length));

    // Modified by JB 030201 should just add the rescaled distance
    // from centroid to point of origin to the orignal centroid
    // position for point a, subtract fo point b

    param.point_of_origin_a.x = param.centroid.x + cfact*dx;
    param.point_of_origin_a.y = param.centroid.y + cfact*dy;

    param.point_of_origin_b.x = param.centroid.x - cfact*dx;
    param.point_of_origin_b.y = param.centroid.y - cfact*dy;

    //=============================================================
    // set all the values
    //=============================================================

    // note miss is also scaled by cos(theta) in case somebody wants
    // to re-calculate alpha from miss and distance later.

    param.width = ezwidth;
    param.length = ezlength;
    // param.distance /= cos(zen); // from now on, don't correct distance
                                  //  (it's not needed)
    param.miss /= cos(zen);


}
```

Bibliography

F. Aharonian and A. Neronov. High-Energy Gamma Rays from the Massive Black Hole in the Galactic Center. *ApJ*, 619:306–313, January 2005.

F. Aharonian, A. G. Akhperjanian, K.-M. Aye, A. R. Bazer-Bachi, M. Beilicke, W. Benbow, D. Berge, P. Berghaus, K. Bernlöhr, O. Bolz, C. Boisson, C. Borgmeier, F. Breitling, A. M. Brown, J. Bussons Gordo, P. M. Chadwick, V. R. Chitnis, L.-M. Chounet, R. Cornils, L. Costamante, B. Degrange, A. Djannati-Ataï, L. O'C. Drury, T. Ergin, P. Espigat, F. Feinstein, P. Fleury, G. Fontaine, S. Funk, Y. Gallant, B. Giebels, S. Gillessen, P. Goret, J. Guy, C. Hadjichristidis, M. Hauser, G. Heinzelmann, G. Henri, G. Hermann, J. A. Hinton, W. Hofmann, M. Holleran, D. Horns, O. C. de Jager, I. Jung, B. Khélifi, N. Komin, A. Konopelko, I. J. Latham, R. Le Gallou, M. Lemoine, A. Lemière, N. Leroy, T. Lohse, A. Marcowith, C. Masterson, T. J. L. McComb, M. de Naurois, S. J. Nolan, A. Noutsos, K. J. Orford, J. L. Osborne, M. Ouchrif, M. Panter, G. Pelletier, S. Pita, M. Pohl, G. Pühlhofer, M. Punch, B. C. Raubenheimer, M. Raue, J. Raux, S. M. Rayner, I. Redondo, A. Reimer, O. Reimer, J. Ripken, M. Rivoal, L. Rob, L. Rolland, G. Rowell, V. Sahakian, L. Saugé, S. Schlenker, R. Schlickeiser, C. Schuster, U. Schwanke, M. Siewert, H. Sol, R. Steenkamp, C. Stegmann, J.-P. Tavernet, C. G. Théoret, M. Tluczykont, D. J. van der Walt, G. Vasileiadis, P. Vincent, B. Visser, H. J. Völk, and S. J. Wagner. Very high energy gamma rays from the direction of Sagittarius A*. *Astronomy and Astrophysics*, 425:L13–L17, October 2004.

A. Atoyan and C. D. Dermer. TeV Emission from the Galactic Center Black Hole Plerion. *ApJL*, 617:L123–L126, December 2004.

F. K. Baganoff, Y. Maeda, M. Morris, M. W. Bautz, W. N. Brandt, W. Cui, J. P. Doty, E. D. Feigelson, G. P. Garmire, S. H. Pravdo, G. R. Ricker, and L. K. Townsley. Chandra X-Ray Spectroscopic Imaging of Sagittarius A* and the Central Parsec of the Galaxy. *ApJ*, 591:891–915, July 2003.

B. Balick and R. L. Brown. Intense sub-arcsecond structure in the galactic center. *ApJ*, 194:265–270, December 1974.

L. Bergström, P. Ullio, and J. H. Buckley. Observability of gamma rays from dark matter neutralino annihilations in the Milky Way halo. *Astroparticle Physics*, 9: 137–162, August 1998.

J. Buckley. Very-High-Energy Gamma-Ray Emission from the Galactic Center. *Galactic Center Newsletter*, 20:6–12, May 2005.

J. H. Buckley, C. W. Akerlof, D. A. Carter-Lewis, M. Catanese, M. F. Cawley, V. Connaughton, D. J. Fegan, J. P. Finley, J. A. Gaidos, A. M. Hillas, F. Krennrich, R. C. Lamb, R. W. Lessard, J. E. McEnery, G. Mohanty, J. Quinn, A. J. Rodgers, H. J. Rose, A. C. Rovero, M. S. Schubnell, G. Sembroski, R. Srinivasan, T. C. Weekes, and J. Zweerink. Constraints on cosmic-ray origin from TeV gamma-ray observations of supernova remnants. *Astronomy and Astrophysics*, 329:639–658, January 1998.

J.M. Davies and E.S. Cotton. *Solar Energy Sci. and Eng*, 1:16, 1957.

A. Eckart, F. K. Baganoff, M. Morris, M. W. Bautz, W. N. Brandt, G. P. Garmire, R. Genzel, T. Ott, G. R. Ricker, C. Straubmeier, T. Viehmann, R. Schödel, G. C. Bower, and J. E. Goldston. First simultaneous NIR/X-ray detection of a flare from Sgr A*. *Astronomy and Astrophysics*, 427:1–11, November 2004.

S. Eidelman, K.G. Hayes, K.A. Olive, M. Aguilar-Benitez, C. Amsler, D. Asner, K.S. Babu, R.M. Barnett, J. Beringer, P.R. Burchat, C.D. Carone, C. Caso, G. Conforto, O. Dahl, G. D'Ambrosio, M. Doser, J.L. Feng, T. Gherghetta, L. Gibbons, M. Goodman, C. Grab, D.E. Groom, A. Gurtu, K. Hagiwara, J.J. Hernández-Rey, K. Hikasa, K. Honscheid, H. Jawahery, C. Kolda, Kwon Y., M.L. Mangano, A.V. Manohar, J. March-Russell, A. Masoni, R. Miquel, K. Mönig, H. Murayama, K. Nakamura, S. Navas, L. Pape, C. Patrignani, A. Piepke, G. Raffelt, M. Roos, M. Tanabashi, J. Terning, N.A. Törnqvist, T.G. Trippe, P. Vogel, C.G. Wohl, R.L. Workman, W.-M. Yao, P.A. Zyla, B. Armstrong, P.S. Gee, G. Harper, K.S. Lugovsky, S.B. Lugovsky, V.S. Lugovsky, A. Rom, M. Artuso, E. Barberio, M. Battaglia, H. Bichsel, O. Biebel, P. Bloch, R.N. Cahn, D. Casper, A. Cattai, R.S. Chivukula, G. Cowan, T. Damour, K. Desler, M.A. Dobbs, M. Drees, A. Edwards, D.A. Edwards, V.D. Elvira, J. Erler, V.V. Ezhela, W. Fetscher, B.D. Fields, B. Foster, D. Froidevaux, M. Fukugita, T.K. Gaisser, L. Garren, H.-J. Gerber, G. Gerbier, F.J. Gilman, H.E. Haber, C. Hagmann, J. Hewett, I. Hinchliffe, C.J. Hogan, G. Höhler, P. Igo-Kemenes, J.D. Jackson, K.F. Johnson, D. Karlen, B. Kayser, D. Kirkby, S.R. Klein, K. Kleinknecht, I.G. Knowles, P. Kreitz, Yu.V. Kuyanov, O. Lahav, P. Langacker, A. Liddle, L. Littenberg, D.M. Manley, A.D. Martin, M. Narain, P. Nason, Y. Nir, J.A. Peacock, H.R. Quinn, S. Raby, B.N. Ratcliff, E.A. Razuvaev, B. Renk, G. Rolandi, M.T. Ronan, L.J. Rosenberg, C.T. Sachrajda, Y. Sakai, A.I. Sanda, S. Sarkar, M. Schmitt, O. Schneider, D. Scott, W.G. Seligman, M.H. Shaevitz, T. Sjöstrand, G.F. Smoot, S. Spanier, H. Spieler, N.J.C. Spooner, M. Srednicki, A. Stahl, T. Stanev, M. Suzuki, N.P. Tkachenko, G.H. Trilling, G. Valencia, K. van Bibber, M.G. Vincter, D. Ward, B.R. Webber, M. Whalley, L. Wolfenstein, J. Womersley, C.L. Woody, O.V. Zenin, and R.-Y. Zhu. Review of Particle Physics. *Physics Letters B*, 592:1+, 2004. URL http://pdg.lbl.gov.

R. D. Ekers, W. M. Goss, U. J. Schwarz, D. Downes, and D. H. Rogstad. A full synthesis map of SGR A at 5GHz. *Astronomy and Astrophysics*, 43:159–166, October 1975.

R. D. Ekers, J. H. van Gorkom, U. J. Schwarz, and W. M. Goss. The radio structure of SGR A. *Astronomy and Astrophysics*, 122:143–150, June 1983.

J. Ellis, K. A. Olive, Y. Santoso, and V. C. Spanos. *Phys. Lett. B*, 565:176, 2003.

A. A. Esin, J. E. McClintock, and R. Narayan. Advection-dominated Accretion and the Spectral States of Black Hole X-Ray Binaries: Application to Nova MUSCAE 1991. *ApJ*, 489:865–+, November 1997.

H. Falcke. *Radio and X-ray emission from the Galactic black hole*, pages 310–342. The Galactic Black Hole, 2003.

M. Fatuzzo and F. Melia. A Kinship Between the EGRET Supernova Remnants and Sagittarius A East. *ApJ*, 596:1035–1043, October 2003.

I. Frank and I. Tamm. Cerenkov radiation. *C.R. Acc. Sci. U.S.S.R.*, 14:109, 1937.

Juhan Frank, Andrew King, and Derek Raine. *Accretion Power in Astrophysics*. Cambridge University Press, 1992.

R. Genzel, R. Schödel, T. Ott, A. Eckart, T. Alexander, F. Lacombe, D. Rouan, and B. Aschenbach. Near-infrared flares from accreting gas around the supermassive black hole at the Galactic Centre. *Nature*, 425:934–937, October 2003.

A. M. Ghez, S. Salim, S. D. Hornstein, A. Tanner, J. R. Lu, M. Morris, E. E. Becklin, and G. Duchêne. Stellar Orbits around the Galactic Center Black Hole. *ApJ*, 620: 744–757, February 2005.

K. Griest and M. Kamionkowski. Unitarity limits on the mass and radius of dark-matter particles. *Physical Review Letters*, 64:615–618, February 1990.

K. Griest, M. Kamionkowski, and M. S. Turner. Supersymmetric dark matter above the W mass. *Phys. Rev. D*, 41:3565–3582, June 1990.

A. M. Hillas, C. W. Akerlof, S. D. Biller, J. H. Buckley, D. A. Carter-Lewis, M. Catanese, M. F. Cawley, D. J. Fegan, J. P. Finley, J. A. Gaidos, F. Krennrich, R. C. Lamb, M. J. Lang, G. Mohanty, M. Punch, P. T. Reynolds, A. J. Rodgers, H. J. Rose, A. C. Rovero, M. S. Schubnell, G. H. Sembroski, G. Vacanti, T. C. Weekes, M. West, and J. Zweerink. The Spectrum of TeV Gamma Rays from the Crab Nebula. *ApJ*, 503:744–+, August 1998.

D. Hooper and B. Dingus. Improving the angular resolution of egret and new limits on supersymmetric dark matter near the galactic center. *astro-ph*, 0212509, 2002.

D. Horns. TeV γ-radiation from Dark Matter annihilation in the Galactic center. *ArXiv Astrophysics e-prints*, August 2004.

S. Ichimaru. Bimodal behavior of accretion disks - Theory and application to Cygnus X-1 transitions. *ApJ*, 214:840–855, June 1977.

J.V. Jelley. *Čerenkov Radiation and its Applications*, chapter 9. Pergamon Press, Inc, 1958.

G. Jungman and M. Kamionkowski. γ rays from neutralino annihilation. *Phys. Rev. D*, 51:3121–3124, March 1995.

G. Jungman, M. Kamionkowski, and K. Griest. Supersymmetric dark matter. *Physics Reports*, 1995.

A. Khokhlov and F. Melia. Powerful Ejection of Matter from Tidally Disrupted Stars near Massive Black Holes and a Possible Application to Sagittarius A East. *ApJL*, 457:L61+, February 1996.

J. Kildea. Act source skymap. private communication, 2005.

K. Kosack, H. M. Badran, I. H. Bond, P. J. Boyle, S. M. Bradbury, J. H. Buckley, D. A. Carter-Lewis, O. Celik, V. Connaughton, W. Cui, M. Daniel, M. D'Vali, I. de la Calle Perez, C. Duke, A. Falcone, D. J. Fegan, S. J. Fegan, J. P. Finley, L. F. Fortson, J. A. Gaidos, S. Gammell, K. Gibbs, G. H. Gillanders, J. Grube, K. Gutierrez, J. Hall, T. A. Hall, D. Hanna, A. M. Hillas, J. Holder, D. Horan, A. Jarvis, M. Jordan, G. E. Kenny, M. Kertzman, D. Kieda, J. Kildea, J. Knapp, H. Krawczynski, F. Krennrich, M. J. Lang, S. Le Bohec, E. Linton, J. Lloyd-Evans, A. Milovanovic, J. McEnery, P. Moriarty, D. Muller, T. Nagai, S. Nolan, R. A. Ong, R. Pallassini, D. Petry, B. Power-Mooney, J. Quinn, M. Quinn, K. Ragan, P. Rebillot, P. T. Reynolds, H. J. Rose, M. Schroedter, G. H. Sembroski, S. P. Swordy, A. Syson, V. V. Vassiliev, S. P. Wakely, G. Walker, T. C. Weekes, and J. Zweerink. TeV Gamma-Ray Observations of the Galactic Center. *ApJL*, 608: L97–L100, June 2004.

T. P. Krichbaum, D. A. Graham, A. Witzel, A. Greve, J. E. Wink, M. Grewing, F. Colomer, P. de Vicente, J. Gomez-Gonzalez, A. Baudry, and J. A. Zensus. VLBI observations of the galactic center source SGR A* at 86 GHz and 215 GHz. *Astronomy and Astrophysics*, 335:L106–L110, July 1998.

T.-P. Li and Y.-Q. Ma. Analysis methods for results in gamma-ray astronomy. *ApJ*, 272:317–324, September 1983.

S. Liu and F. Melia. An Accretion-induced X-Ray Flare in Sagittarius A*. *ApJL*, 566:L77–L80, February 2002.

K. Y. Lo, Z. Shen, J. Zhao, and P. T. P. Ho. Intrinsic Size of Sagittarius A*: 72 Schwarzschild Radii. *ApJL*, 508:L61–L64, November 1998.

Malcolm S. Longair. *High Energy Astrophysics*, volume 1. Cambridge University Press, New York, 2nd edition, 1992.

D. Lynden-Bell and M. J. Rees. On quasars, dust and the galactic centre. *MNRAS*, 152:461–+, 1971.

Y. Maeda, F. K. Baganoff, E. D. Feigelson, M. Morris, M. W. Bautz, W. N. Brandt, D. N. Burrows, J. P. Doty, G. P. Garmire, S. H. Pravdo, G. R. Ricker, and L. K. Townsley. A Chandra Study of Sagittarius A East: A Supernova Remnant Regulating the Activity of Our Galactic Center? *ApJ*, 570:671–687, May 2002.

T. Manmoto, S. Mineshige, and M. Kusunose. Spectrum of Optically Thin Advection-dominated Accretion Flow around a Black Hole: Application to Sagittarius A *. *ApJ*, 489:791–+, November 1997.

S. Markoff, H. Falcke, F. Yuan, and P. L. Biermann. The Nature of the 10 kilosecond X-ray flare in Sgr A*. *Astronomy and Astrophysics*, 379:L13–L16, November 2001.

H. A. Mayer-Hasselwander, D. L. Bertsch, B. L. Dingus, A. Eckart, J. A. Esposito, R. Genzel, R. C. Hartman, S. D. Hunter, G. Kanbach, D. A. Kniffen, Y. C. Lin, P. F. Michelson, A. Muecke, C. von Montigny, R. Mukherjee, P. L. Nolan, M. Pohl, O. Reimer, E. J. Schneid, P. Sreekumar, and D. J. Thompson. High-energy gamma-ray emission from the Galactic Center. *Astronomy and Astrophysics*, 335:161–172, July 1998.

Fulvio Melia and Heino Falcke. The supermassive black hole at the galactic center. *astro-ph*, 0106162, 2001.

P. G. Mezger, W. J. Duschl, and R. Zylka. The Galactic Center: a laboratory for AGN? *The Astronomy and Astrophysics Review*, 7:289–388, 1996.

G. Mohanty, S. Biller, D. A. Carter-Lewis, D. J. Fegan, A. M. Hillas, R. C. Lamb, T. C. Weekes, M. West, and J. Zweerink. Measurement of TeV gamma-ray spectra with the Cherenkov imaging technique. *Astroparticle Physics*, 9:15–43, June 1998.

B. Moore, F. Governato, T. Quinn, J. Stadel, and G. Lake. Resolving the Structure of Cold Dark Matter Halos. *ApJL*, 499:L5+, May 1998.

R. Narayan, I. Yi, and R. Mahadevan. Explaining the Spectrum of SAGITTARIUS-A* with a Model of an Accreting Black-Hole. *Nature*, 374:623–+, April 1995.

R. Narayan, R. Mahadevan, J. E. Grindlay, R. G. Popham, and C. Gammie. Advection-dominated accretion model of Sagittarius A*: evidence for a black hole at the Galactic center. *ApJ*, 492:554–568, January 1998.

J. F. Navarro, C. S. Frenk, and S. D. M. White. The Structure of Cold Dark Matter Halos. *ApJ*, 462:563–+, May 1996.

Raymond Plante, K. Y. Lo, and Richard M. Crutcher. Image from http://archive.ncsa.uiuc.edu/Cyberia/Bima/GalCntr.html. University of Illinois at Urbana-Champaign, Astronomy Department.

M. Pohl. A variability and localization study of 3EG J1746-2851. *ArXiv Astrophysics e-prints*, December 2004.

D. Porquet, P. Predehl, B. Aschenbach, N. Grosso, A. Goldwurm, P. Goldoni, R. S. Warwick, and A. Decourchelle. XMM-Newton observation of the brightest X-ray flare detected so far from Sgr A*. *Astronomy and Astrophysics*, 407:L17–L20, August 2003.

M. Punch, C. W. Akerlof, M. F. Cawley, M. Chantell, D. J. Fegan, S. Fennell, J. A. Gaidos, J. Hagan, A. M. Hillas, Y. Jiang, A. D. Kerrick, R. C. Lamb, M. A. Lawrence, D. A. Lewis, D. I. Meyer, G. Mohanty, K. S. O'Flaherty, P. T. Reynolds, A. C. Rovero, M. S. Schubnell, G. Sembroski, T. C. Weekes, and C. Wilson. Detection of TeV photons from the active galaxy Markarian 421. *Nature*, 358:477–+, August 1992.

P.F.R. Rebillot. Pmt q.e. measurements. private communication, 2003.

M. J. Reid and A. Brunthaler. The Proper Motion of Sagittarius A*. II. The Mass of Sagittarius A*. *ApJ*, 616:872–884, December 2004.

P. T. Reynolds, C. W. Akerlof, M. F. Cawley, M. Chantell, D. J. Fegan, A. M. Hillas, R. C. Lamb, M. J. Lang, M. A. Lawrence, D. A. Lewis, D. Macomb, D. I. Meyer, G. Mohanty, K. S. O'Flaherty, M. Punch, M. S. Schubnell, G. Vacanti, T. C. Weekes, and T. Whitaker. Survey of candidate gamma-ray sources at TeV energies using a high-resolution Cerenkov imaging system - 1988-1991. *ApJ*, 404:206–218, February 1993.

S. Roy and A. Pramesh Rao. Sgr A* at low radio frequencies: Giant Metrewave Radio Telescope observations. *MNRAS*, 349:L25–L29, April 2004.

K. Tsuchiya, R. Enomoto, L. T. Ksenofontov, M. Mori, T. Naito, A. Asahara, G. V. Bicknell, R. W. Clay, Y. Doi, P. G. Edwards, S. Gunji, S. Hara, T. Hara, T. Hattori, S. Hayashi, C. Itoh, S. Kabuki, F. Kajino, H. Katagiri, A. Kawachi, T. Kifune, H. Kubo, T. Kurihara, R. Kurosaka, J. Kushida, Y. Matsubara, Y. Miyashita, Y. Mizumoto, H. Moro, H. Muraishi, Y. Muraki, T. Nakase, D. Nishida, K. Nishijima, M. Ohishi, K. Okumura, J. R. Patterson, R. J. Protheroe, N. Sakamoto, K. Sakurazawa, D. L. Swaby, T. Tanimori, H. Tanimura, G. Thornton, F. Tokanai, T. Uchida, S. Watanabe, T. Yamaoka, S. Yanagita, T. Yoshida, and T. Yoshikoshi. Detection of Sub-TeV Gamma Rays from the Galactic Center Direction by CANGAROO-II. *ApJL*, 606:L115–L118, May 2004.

P. Ullio and L. Bergström. Neutralino annihilation into a photon and a Z boson. *Phys. Rev. D*, 57:1962–1971, February 1998.

T. C. Weekes, M. F. Cawley, D. J. Fegan, K. G. Gibbs, A. M. Hillas, P. W. Kowk, R. C. Lamb, D. A. Lewis, D. Macomb, N. A. Porter, P. T. Reynolds, and G. Vacanti. Observation of TeV gamma rays from the Crab nebula using the atmospheric Cerenkov imaging technique. *ApJ*, 342:379–395, July 1989.

T.C. Weekes. *Very High Energy Gamma-Ray Astronomy*. Institute of Physics Publishing, 2003.

F. Yuan, S. Markoff, and H. Falcke. A Jet-ADAF model for Sgr A*. *Astronomy and Astrophysics*, 383:854–863, March 2002.

J. Zhao, G. C. Bower, and W. M. Goss. Radio Variability of Sagittarius A*-a 106 Day Cycle. *ApJL*, 547:L29–L32, January 2001.

R. Zylka, P. G. Mezger, and H. Lesch. Anatomy of the Sagittarius A complex. II - 1300 micron and 870 micron continuum observations of SGR A* and its submm/IR spectrum. *Astronomy and Astrophysics*, 261:119–129, July 1992.